STUDY OF SECONDARY NEUTRONS FROM UNIFORM SCANNING PROTON BEAMS BY MEANS OF EXPERIMENT AND SIMULATION

By

MOHAMMAD RAFIQUL ISLAM

Master of Science
Oklahoma State University
Stillwater, Oklahoma
May, 2013

Submitted to the Faculty of the
Graduate College of the
Oklahoma State University
in partial fulfillment of
the requirement for
the Degree of
DOCTOR OF PHILOSOPHY
July, 2013

STUDY OF SECONDARY NEUTRONS FROM UNIFORM SCANNING PROTON BEAMS BY MEANS OF EXPERIMENT AND SIMULATION

Dissertation Approved:

Eric Benton

_____

Dissertation Adviser

Eduardo G Yukihara

_____

Committee Member

Jerimy C Polf

_____

Committee Member

Carl D Latino

_____

Committee Member

Dedicated to my Father

Mohammad Nurul Alam Akand

ACKNOWLEDGEMENT

There are lots of individuals whom I would like to thank for their help and support for the successfully completion of this work. First of all, I would like to thank my advisor, Dr. Eric Benton, for his guidance, encouragement, and incessant support throughput this project. A time to time discussion with him on this project made me confident, focused and more motivated. I am inspired by his pleasant personality and capable leadership.

Sincere thanks to Dr. Art Lucas, Dr. Joel Dewitt, Dr. Carl Johnson, Dr. Tyler Collums, Jonathon Monson, Aaron Ruse, Nathan Lindy, and Robert Honeyman for their support and assistance.

Heartfelt thanks to my wife, Maliha Rahman and my son Nameer, for their love, support, and presence during the challenging period of this project.

My sincere thanks to my parents for their support for my whole life and without them I could never come this far. My parents always had confidence in me that I can

Acknowledgements reflect the views of the author and are not endorsed by committee members or Oklahoma State University.

do better and that inspiration helped and encouraged me in successfully completing this work.

I would also like to thank Dr. Yuanshui Zheng for his generous support, especially for the beam time and the information related to beam delivery system used at ProCure Proton Therapy Center, Oklahoma City, OK. I would also like to thank my Committee members, Dr. Eduardo Yukihara, Dr. Jerimy Polf, and Dr. Carl Latino for their time and support in this project.

Sincere thanks to all the staff of the physics department, especially, Susan Cantrell, Warren Grider, and Melissa Edwards, for their help and support. Special thanks to FLUKA authors and the FLUKA discussion forum for their help, especially Vasilis Vlachoudis for his help to successfully simulate the experiments.

Acknowledgements reflect the views of the author and are not endorsed by committee members or Oklahoma State University.

Name: MOHAMMAD RAFIQUL ISLAM

Date of Degree: July, 2013

Title of Study: STUDY OF SECONDARY NEUTRONS FROM UNIFORM SCANNING PROTON BEAMS BY MEANS OF EXPERIMENT AND SIMULATION

Major Field: Physics

ABSTRACT:

Proton radiotherapy is becoming popular as an effective modality to treat cancer. However the advantages of the proton radiotherapy could be offset due to the effect of secondary neutrons. Secondary neutrons are an undesired byproduct in proton radiotherapy. It is important to quantify the dose equivalent due to secondary neutrons since they could lead to secondary cancer later in the patient's life. In this study, our aim was to investigate the off-axis dose equivalent due to secondary neutrons from a uniform scanning proton radiotherapy system at the ProCure Proton Therapy Center, Oklahoma City, OK. Both experiments and simulations were carried out for the purpose of this study. CR-39 plastic nuclear track detectors were used to measure dose equivalent inside a phantom and in air at various depths and angles with respect to the primary beam axis for four different experimental configurations. Three different proton beam energies, 78 MeV, 162 MeV and 226 MeV, all using a 4 cm modulation width, a 5 cm diameter brass aperture, and a small snout located 38 cm from isocenter were used for the experiments. The Monte Carlo radiation transport code FLUKA was used to simulate the experiments for a simplified snout configuration. The measured ratio of secondary neutron dose equivalent to therapeutic primary proton dose (H_n/D_p) ranged from 0.3 mSv/Gy to 50 mSv/Gy. Both experiment and simulation showed a similar decreasing trend in dose equivalent with distance from beam isocenter and the magnitude varied by a factor of about 4 in most of the locations. An overall higher H_n/D_p in air than inside the phantom was observed and this suggests that the production of secondary neutrons in the beam delivery device is significantly higher than inside the body. Comparison of H_n/D_p with other studies suggests that the neutron exposure to patients from uniform scanning systems is similar to that of passive scattering systems.

TABLE OF CONTENTS

LIST OF TABLES

Table Page

LIST OF FIGURES

Figure Page

CHAPTER 1

INTRODUCTION

In radiation therapy, the purpose is to deliver a greater dose of ionizing radiation to the cancerous tumor, sufficient to kill the tumor, while delivering a minimal dose to the surrounding healthy tissue. Protons have been used in radiation therapy for several decades and are continually gaining in popularity. This is primarily because energetic protons have finite range and deposit most of their energy near the end of their range, known as Bragg peak. In 1945, Robert Wilson first suggested that the property of Bragg peak of energetic protons might be useful in medical use. This is because, by modulating the energy (range) of the beam, the Bragg peak can be made to coincide with the location of the tumor in the patient body. This will allow protons to deposit most of their energy to the tumor and a minimum energy to the healthy tissues surrounding the tumor.

Proton radiotherapy has nearly about 50 years of history. But it has been very slow of becoming a routine modality mostly due to the expense of an accelerator to achieve protons of energy from 50 MeV to 250 MeV required for the treatment.

However, in the last ten years, there has been a rapid growth of proton treatment facilities around the world due to the precise dose delivery that a proton beam can offer. Currently, there are 38 proton facilities operating around the world and 34 more is under consideration (PTCOG, 2013). This growing number suggests that proton radiotherapy is becoming increasingly important as an effective form of radiotherapy in the years to come.

The primary proton beam, used in proton radiotherapy, is generally too narrow to cover a tumor of practical size. For this reason, the beam needs to spread over the treatment volume. The spreading of a beam is done in beam delivery device either by inserting scattering material along the beam path commonly known as passive scattering system, or by using sweeping magnets to scan the beam onto the tumor known as active scanning system. When the beam is shaped, primary protons will undergo nuclear interactions with different beam shaping components in the beam delivery device, resulting the production of secondary neutrons, known as external neutrons (Perez-Andujar et al., 2009, Polf et al., 2005, Polf and Newhauser, 2005, Hecksel et al., 2010, Jiang et al., 2005, Zheng et al., 2007b, Zheng et al., 2008, Zheng et al., 2007a, Moyers et al., 2008, Binns and Hough, 1997). Neutrons can also be created inside the body due to the nuclear interaction of proton with tissue mass, commonly known as internal neutrons.

Neutrons have long been known to capable of doing greater biological damage than similar dose of x-rays, electrons or protons. Partly, this is due to the fact that

neutrons do not interact through Coulomb barrier; instead, the interaction occurs through nuclear interaction processes. As a result, energy tends to be transferred through light nuclei due to elastic and inelastic nuclear interaction, causing greater damages to the cell. This makes neutrons more biologically damaging, i.e. higher relative biological effectiveness (RBE) compared to other forms of radiation such as x-rays, and protons. Because of the higher RBE, neutrons may lead a secondary cancer later in the patient's lifetime. Due to the risk of secondary cancer, the secondary neutrons produced in proton treatment facility should be assessed, monitored, and minimized as much as possible.

The measurement of dose and dose equivalent due to neutrons is not straightforward. This is because the interaction probability (cross section) of neutrons with detecting material (e.g. gas) used in common radiation detector (e.g. ionization chamber) is negligible. In addition, the signal due to neutrons is swamped by the primary radiation in such detectors. Due to this, special methods are needed to employ for the detection of neutrons of variable energies. Common types of neutron detectors used in neutron dosimetry include, REM meter, Bonner sphere, bubble detector, etc., where a fluence to dose equivalent conversion coefficients is used to measure the neutron dose equivalent. The conversion coefficients used in these detectors are, in general, determined based on the Monte Carlo method, allowing a greater uncertainty in the measured result.

An alternative detector in neutron dosimetry is CR-39 plastic nuclear track detector (PNTD). CR-39 PNTD is a thin plastic polymer and the advantages of CR-39 PNTD include: a) CR-39 PNTD is insensitive to primary protons but has tissue like sensitivity to the neutrons, b) dose and dose equivalent can be measured directly from the LET information of the incident particles, and c) unlike other detectors it is thin and can be placed anywhere inside the phantom to measure organ equivalent dose. For all these reasons, this study uses CR-39 PNTD for the measurement of dose equivalent from secondary neutrons.

In this work, our aim is to study the off-axis secondary neutrons created from a uniform scanning proton beam used at ProCure Proton Therapy Center, OK. The uniform scanning beam delivery system is a very recent development and not many treatment centers have this mode of beam delivery system available. Also, the literature available for the secondary neutrons due to uniform scanning is scarce. In addition, no treatment planning technique in proton radiotherapy to date accounts the possible neutron exposure. The objective of this work is to quantify the dose equivalent due to secondary neutrons produced in a uniform scanning system inside the phantom and in air at different angles and locations relative to isocenter of the beam for different proton energies with a typical treatment set up. The study was carried out by means of experiment and simulation using a simplified version of uniform scanning systems (See Section 2.6.2.2) currently in use at ProCure Proton Therapy Center, Oklahoma City, OK. The focus of this study is to help with the followings:

a) quantitative study of dose equivalent due to secondary neutrons for a common proton radiotherapy treatment facility using uniform scanning beam delivery system
b) if uniform scanning beam delivery system serves better over passive scattering system in neutron production
c) if there is a need to improving beam shaping components for better shielding of neutrons used in uniform scanning system

1.1 *Organization of this work*

This work presents general radiation therapy, the rationale for proton radiotherapy, underlying principle of proton radiotherapy, and the current status of proton radiotherapy in Chapter Two. Different types of beam shaping devices including active scanning and passive scattering devices are also discussed here. The neutrons environment at a common proton radiotherapy treatment facility and the basic mechanism responsible for the production of secondary neutrons is presented in Chapter Three. Chapter Four discusses on the fundamental dosimetric quantities required for the calculation of absorbed dose and dose equivalent. The method of fluence to dose equivalent conversion in FLUKA is also discussed in Chapter Four. The detail about CR-39 plastic nuclear track detector, experimental design and simulation approach is presented in Chapter Five. Chapter Five also discusses on the design of experiment and numerical configurations that has been employed in this study and the importance of such approaches in determining neutrons dose

equivalent in proton radiotherapy. Detector read-out process and the method used to analyze the experimental and simulated data are presented in Chapter Six. Results from both experiment and simulation from this study is presented in Chapter Seven. Finally, Chapter Eight compares results from this study with published data for similar passive scattering and uniform scanning beam delivery systems. A summary of this study and related future work is also mentioned in Chapter Eight.

CHAPTER 2

RADIOTHERAPY

This chapter describes radiation therapy and compares different modes of radiotherapy. The history of proton radiotherapy, current status, and underlying principle of proton radiotherapy are presented. The beam delivery system in proton radiotherapy plays an important role in shaping the beam to the contours of the tumor. The design of the beam delivery system also plays a major role in the number of secondary neutrons produced by the proton radiotherapy beam. A number of different types of beam delivery system have been developed for use in proton radiotherapy and three major types will be described in detail, especially with regard to the production of secondary neutrons.

2.1 *General Radiotherapy*

Radiation therapy (or radiotherapy) refers the use of ionizing radiation to treat cancer by killing the malignant cells that make up the tumor. The objective of radiotherapy is to deliver a high dose of ionizing radiation to the tumor volume while at the same time minimizing the dose of ionizing radiation delivered to the healthy tissue surrounding the tumor.

Table 2.1: The rate of Radiotherapy used by cancer patients according to cancer type (Joiner and Kogel, 2009).

Tumor type	Proportion of all Cancers (%)	Proportion of patients receiving radiotherapy (%)	Patients receiving radiotherapy (% of all cancers)
Breast	13	83	10.8
Lung	10	76	7.6
Melanoma	11	23	2.5
Prostate	12	60	7.2
Gynecological	5	35	1.8
Colon	9	14	1.3
Rectum	5	61	3.1
Head and Neck	4	78	3.1
Gall Bladder	1	13	0.1
Liver	1	0	0.0
Esophageal	1	80	0.8
Stomach	2	68	1.4
Pancreas	2	57	1.1
Lymphoma	4	65	2.6
Leukemia	3	4	0.1
Myeloma	1	38	0.4
Cancer nervous system	2	92	1.8
Renal	3	27	0.8
Bladder	3	58	1.7
Testis	1	49	0.5
Thyroid	1	10	0.1
Unknown primary	4	61	2.4
Other	2	50	1.0
Total	100		52.3

Today, radiotherapy is one of the most effective treatments for cancer. In a study summarized in Table 2.1, Tobias and Delaney et. al. (Tobias, 1996, Delaney et al., 2005), showed that more than half of all cancer patients (52.3%) receive radiotherapy at some point in their treatment. This table shows the percent of patients receiving radiotherapy as a principal form of treatment as well as the percent of patients of all types of cancers receives radiotherapy at some stage of treatment.

In the early stage of cancer, especially when the cancer is confined to a single tumor and has not metastasized (spread to the other organs), surgery is the preferred treatment. Radiotherapy is an alternative to surgery and an effective form of treatment for long term control of tumors in the lung, cervix, bladder, prostate, head and neck, skin, and other organs. Chemotherapy (where strong chemical agents are used to control the malignant cancerous cells) is the third most important form of cancer treatment, is also popular (Joiner and Kogel, 2009). However, the success rate for treating cancers using chemotherapy alone is low. For local treatment of most types of tumors, a combination of radiotherapy and surgery have a success rate of about 40% (Souhami and Tobias, 1986, DeVita et al., 1979). Radiotherapy as the principal form of treatment has a success rate of about 15% for all types of cancers, whereas the success rate due to chemotherapy alone is about 2% (Joiner and Kogel, 2009). That study estimated that the patient cure rate was around seven times higher in radiotherapy compared to chemotherapy. However, it is important to note that depending on the stage of the cancer, radiotherapy is sometimes

combined with chemotherapy or surgery for treating cancer patients. Based on patient's age, tumor location, stage of the tumor development, and the general health of the patient, the final choice of the treatment modality is made.

In radiation therapy, the tumor is given a prescribed amount dose using ionizing radiation. Exposure of biological cells to ionizing radiation can lead to damage to the cell's DNA. In general, the more frequently a cell undergoes mitosis (reproduction) the more sensitive it is to radiation damage, i.e. the less likely the cell can correctly repair damage due to radiation exposure. Consequently, cancer cells less likely to repair the damage caused by radiation compared to healthy cells.

Damage to DNA by ionizing radiation can take one of the two forms: direct damage and indirect damage. An illustration of direct or indirect interaction is shown in Figure 2.1. Direct damage occurs when the energetic charged particle or photon interacts directly with one or more electrons belonging to the DNA, causing a break in the DNA strand. Indirect reaction, on the other hand, damages cells via free radical. A free radical is highly reactive molecule, atom or ion that has an unpaired orbital electron in the outer shell and is formed when ionizing radiation interacts with small molecules such as water molecules. Such an interaction can be expressed as:

$$radiation + H_2O \rightarrow H_2O^+ + e^-.$$

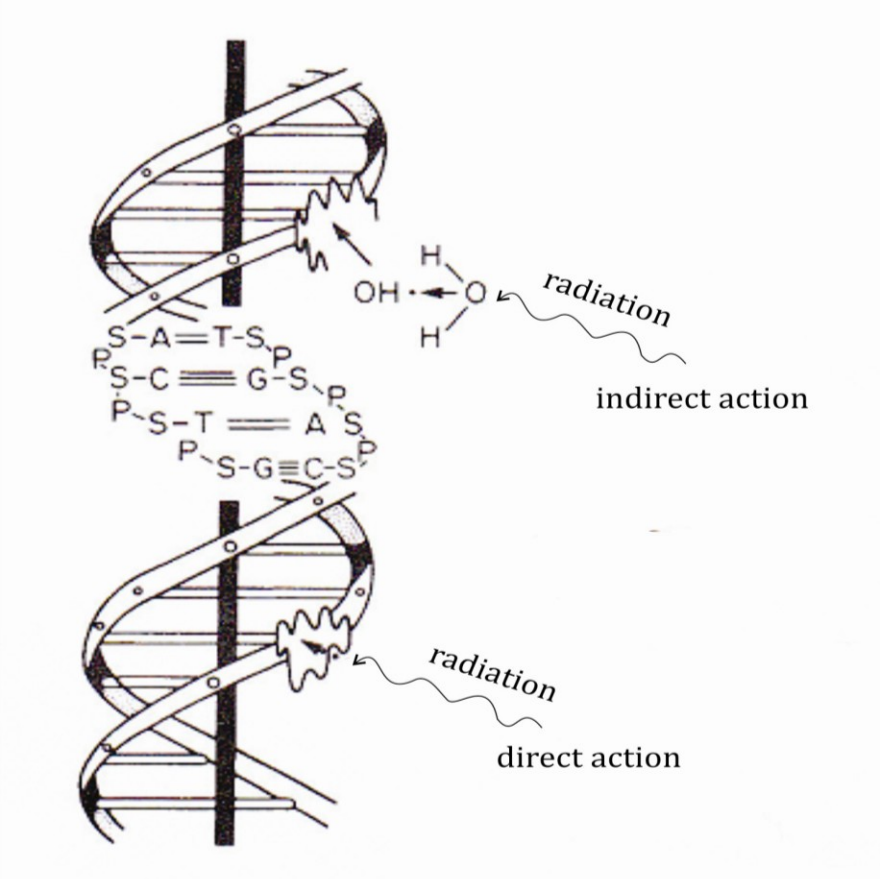

Figure 2.1: A schematic representation of direct and indirect action. Picture was adapted from (Hall and Giaccia, 2006).

The free ion radical (H_2O^+) interact again with another water molecule and produce an hydroxyl radicals (OH^-):

$$H_2O^+ + H_2O \rightarrow H_3O^+ + OH^-.$$

Hydroxyl free radicals (OH^-) are extremely reactive and cause harmful chemical reactions within the cell including reacting with a DNA molecule leading to a strand break. It has been estimated that about two thirds of all damage done to cells by exposure to x-rays can be attributed due to hydroxyl free radicals in indirect interactions (Saha, 2006). Energetic protons and heavy ions mostly damage the cell

via direct reaction, whereas photons and x-rays primarily damage the cell via indirect interactions.

2.1.1 Different forms of Radiotherapy

Depending on the source of radiation, radiation therapy can take two forms: a) external beam radiation therapy (EBRT or XBRT), and b) internal radiotherapy. In external beam radiation therapy, an external source of radiation is placed outside the body to treat cancerous tumors. X-rays and electrons are the most widely used form of radiation in external beam radiation therapy. Superficial tumors such as those on or near the skin are often treated using electrons or low energy (kilo-voltage) x-rays, whereas, megavoltage x-rays are used for deep seated tumors such as tumors in the prostate, lungs, etc. The use of energetic protons and heavy ions also fall in the category of external beam radiotherapy. External beam radiation therapy is further classified as conventional and unconventional radiotherapy. Conventional radiotherapy includes x-ray and electron beam radiotherapy, while unconventional radiotherapy includes proton and heavy ion beam radiotherapy.

Internal radiation therapy, on the other hand, uses radioisotope as radiation source and dose is delivered by placing the source inside or on the treatment volume (Patel and Arthur, 2006). This form of treatment uses both sealed and unsealed radioactive source (NCI, 2013). The use of sealed radioactive sources in and around the tumor is generally known as Brachytherapy. In this method, the placement of

the sources could be either, inside a cavity (intracavity), inside a tumor (interstitialy) or attached to the surface (Khan, 2003). The most common types of radioactive sources used in brachytherapy are ^{98}Au, ^{125}I, ^{192}Ir, and ^{113}Pd. By placing radioisotopes sources or seeds within and in close proximity to the tumor volume, a greater dose can be delivered locally to the tumor while the dose falls off rapidly with distance from the source in the adjacent healthy tissues. Because of this rapid dose fall off, brachytherapy is popular in the treatment of prostate, cervical, breast, and skin cancers. In addition, brachytherapy is sometimes used in conjunction with external radiation therapy to boost the dose directly deliver to the tumor.

Radiotherapy with unsealed sources sometimes also referred as brachytherapy uses soluble forms of radioactive sources such as ^{131}I. This isotope is administered either via injection or ingestion. The use of unsealed sources in radiation therapy is effective only for some types of thyroid cancer, since thyroid cells naturally absorb both radioactive and stable iodine (NCI, 2013). However, depending on the tumor stage, a combination of external and internal beam therapy is commonly prescribed in treatment for thyroid cancer.

2.2 *Basics of Proton Therapy*

In proton radiotherapy, the energetic protons interact with matter through three different processes (Goitein, 2008): a) coulomb interactions with atomic electrons,

b) coulomb interactions with atomic nuclei, and c) nuclear interactions with atomic nuclei. Coulomb interactions with atomic electrons occur when high energy positively charged protons interact with the negatively charged orbital electrons. This process transfers enough kinetic energy to the electrons to cause excitation and ionization of the atoms. The ionization process takes place when the interacting protons transfer sufficient energy and knock out one or more electrons from the target atom. Most of the ejected electrons in ionization process contain small amounts of energy and are stopped in the immediate vicinity of the trajectory of the primary proton. Some of these ejected electrons may receive sufficient energy to travel macroscopic distances inside the matter. These high energy electrons are commonly referred as δ-rays and they can cause further excitation and ionization in the region surrounding the initial interaction. The deflection of primary protons in this process is negligible since protons are much heavier than electrons.

Protons also interact with the coulomb fields of atomic nuclei as they penetrate through matter. Since both protons and nuclei are positively charged, repulsion takes place between incoming protons and atomic nuclei. This causes the protons to scatter since nuclei are of equal or greater mass than the incident protons. However, the net statistical deflection is typically very small after many of such scattering events (Goitein, 2008).

Nuclear interactions with atomic nuclei are another process which occurs via the strong nuclear force. There are two types of nuclear collision: a) elastic collisions,

and b) non-elastic collisions. In elastic collisions, the incident proton transfers a significant fraction of its kinetic energy to the target nucleus, while the nucleus remains intact and the incident proton is deflected by several degrees. An example of an elastic collision of proton with an oxygen nucleus can be written as:

$$p + {}^{16}O \rightarrow p + {}^{16}O.$$

In a non-elastic collision, the interaction of an incident proton with a target nucleus may cause the nucleus to break apart and as a result, fragments of the target nucleus may emerge considerable kinetic energy. In this process, incident protons lose a significant kinetic energy and can be deflected by several degrees. An example of a non-elastic collision of proton with an oxygen atom can be written as:

$$p + {}^{16}O \rightarrow p + {}^{15}O + n.$$

Table 2.2 shows the results due to non-elastic collisions of 150 MeV protons on ^{16}O nuclei (Seltzer, 1993).

Table 2.2: Energy taken up by various particles as a result of 150 MeV protons incident on ^{16}O nucleus (Seltzer, 1993).

Particle	Fraction of energy (%)
Protons	57
Neutrons	20
Alpha particles	2.9
Deuterons	1.6
Tritium	0.2
Helium-3	0.2
Recoil fragments	1.6

Among different processes, the primary mechanism for energy loss by protons as they pass through the matter is the Coulomb interaction with the atomic electrons of the stopping medium. Incident protons in this process experience a gradual loss of energy as they penetrate through matter. The loss of energy of primary protons is not same at all depths in the medium. The loss of energy due to Coulomb interactions can be calculated using the Bethe-Bloch formula (Bethe, 1930):

$$-\frac{dT}{dx} = \frac{n_e e^4}{4\pi\varepsilon_0^2 m v^2} L, \qquad 2.1$$

where $-\frac{dT}{dx}$ is the energy lost by the incident charged particle proton per unit path length, n_e represents the electron density of the target, e represents electron charge, ε_0 represents the permittivity of free space, m is the rest mass of the electron, L represents a collection of logarithmic factors and correction factors. Bethe-Bloch formula assumes that the target electrons are free. This assumption is valid because the binding energy of electrons is much lower than the energy of the incident charged particles. The correction factor L is given by:

$$L = \ln\left(\frac{2mv^2}{I}\right) - \ln\left(1 - \frac{v^2}{c^2}\right) - \frac{v^2}{c^2} - \frac{\delta}{2}. \qquad 2.2$$

The standard relativistic corrections, $-\ln(1 - v^2/c^2) - v^2/c^2$, are important if the projectile in the interaction is moving at a significant fraction of the speed of light. If the velocity of the projectile is small compared to the speed of light, Equation (2.2) simplifies to $L \cong \ln(2mv^2/I)$, where v is the velocity of the incident charged particle

and I is the mean ionization potential. The term, $\delta/2$, in Equation (2.2) represents the density effect correction (Sternheimer and Peierls, 1971).

From Equation 2.1, the energy loss of an incident proton is roughly proportional to the inverse square of its velocity. For this reason, when the velocity of a proton decreases, the energy lost to the stopping medium increases. At the end of the proton range, when the velocity reaches a minimum, the energy loss reaches a maximum causing a peak at the end of its range. This is known as the Bragg peak and this energy loss profile of charged particle in the stopping medium is known as Bragg curve. An example of a Bragg curve for a 200 MeV proton in water is shown in Figure 2.2 (Jones and Schreuder, 2001).

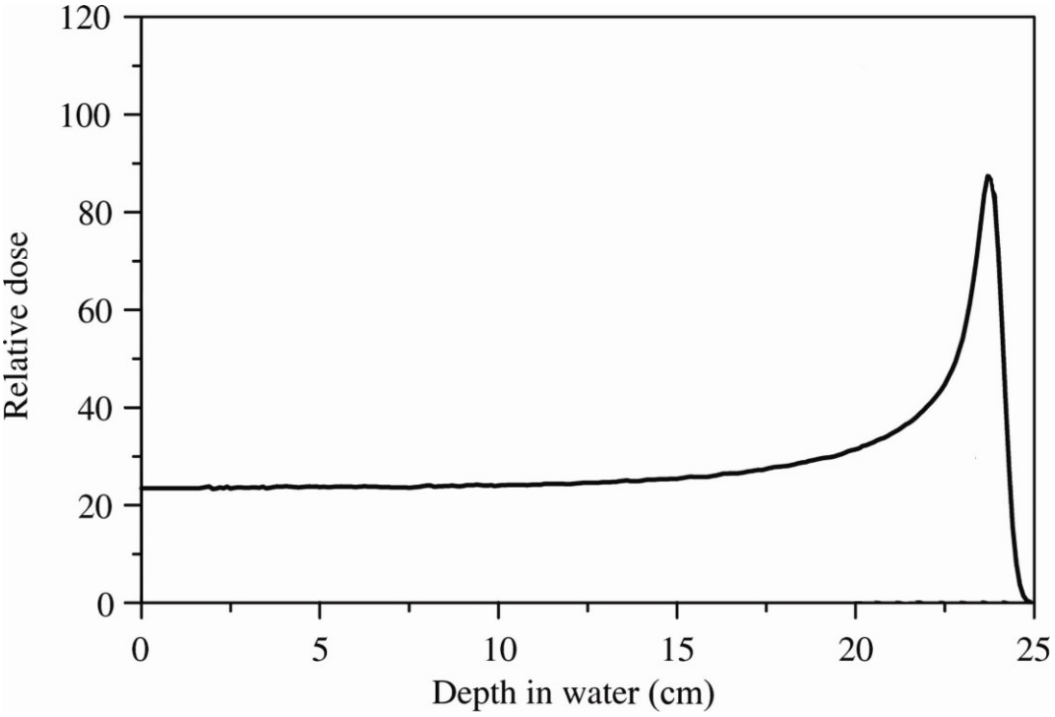

Figure 2.2: A Bragg curve for 200 MeV proton beam in water (Jones and Schreuder, 2001). The Bragg peak is seen at a depth of about 23 cm.

The width of the Bragg peak is caused by the statistical variations in the ionization processes known as range straggling. Range straggling refers to the fact that not all the protons have the same range as there are statistical differences in the ionization processes, causing the end point of the protons to spread out. In addition, the energy of the incident proton beam is never completely monoenergetic and this also contributes in spreading out Bragg peak.

2.3 *Benefits of proton radiotherapy*

In conventional external beam radiotherapy, dose delivered to the patients falls-off exponentially with depth in the patient's body. This leads to the healthy tissue adjacent to the tumor volume receiving significant dose. This problem of minimizing dose to healthy tissue is better handled using proton beams. Protons are relatively heavier and have finite range in matter. The relatively heavy mass allows protons to scatter less as it travel through the matter and the finite range stops the beam at a certain depth inside the tissue. This combination allows the proton beam to deliver maximum energy at the end of its range (i.e. at Bragg peak) and keep focused as it propagates through matter.

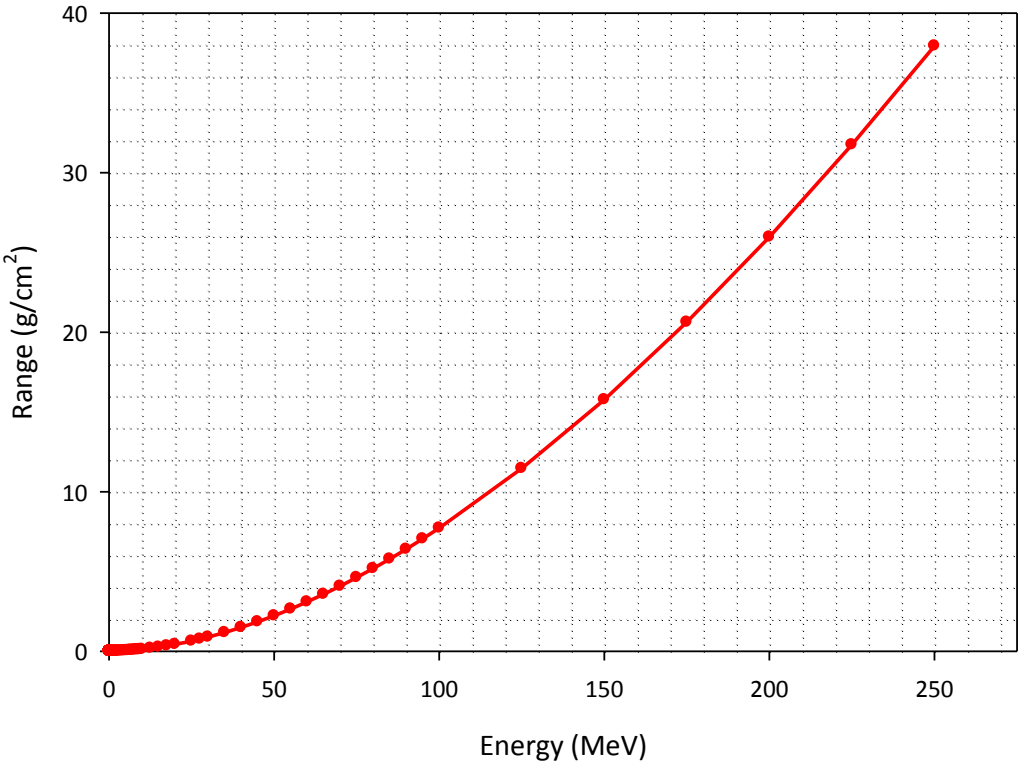

Figure 2.3: Range of proton beam in water. Data taken from NIST website (NIST, 2012).

An example of the range of proton beam for therapeutic energy (up to 300 MeV) in water is shown in Figure 2.3 (NIST). As shown in the figure, a given kinetic energy of a proton corresponds to finite range in water or tissue. This provides a distinct clinical advantage. On the other hand, x-rays do not stop after a finite range but attenuate exponentially with depth in tissue. Because of their inherent properties, x-rays deliver maximum dose near the entrance and a considerably higher dose to the healthy tissue near the treatment volume. Protons, unlike x-rays, deliver a higher dose to the tumor using the Bragg peak property and minimum dose to the adjacent healthy tissue.

Figure 2.4 shows an example of dose deposition in tissue as a function of depth for three different modes of treatment: x-rays (20MV), electrons (4MeV), and protons (150 MeV). As can be seen from this figure, protons deliver most of their dose at the end of their range while x-rays start with a dose build up and then falls off exponentially. Electron beams, on the other hand, show a greater dose fall off but this clinical advantage is limited to lower energy only. As the energy of the electron beam increase, the beam becomes contaminated with x-rays and also electron scatters to a great extent as they travel through the tissue. Clinically, this restricts the use of electron beams to treatment of shallow tumors.

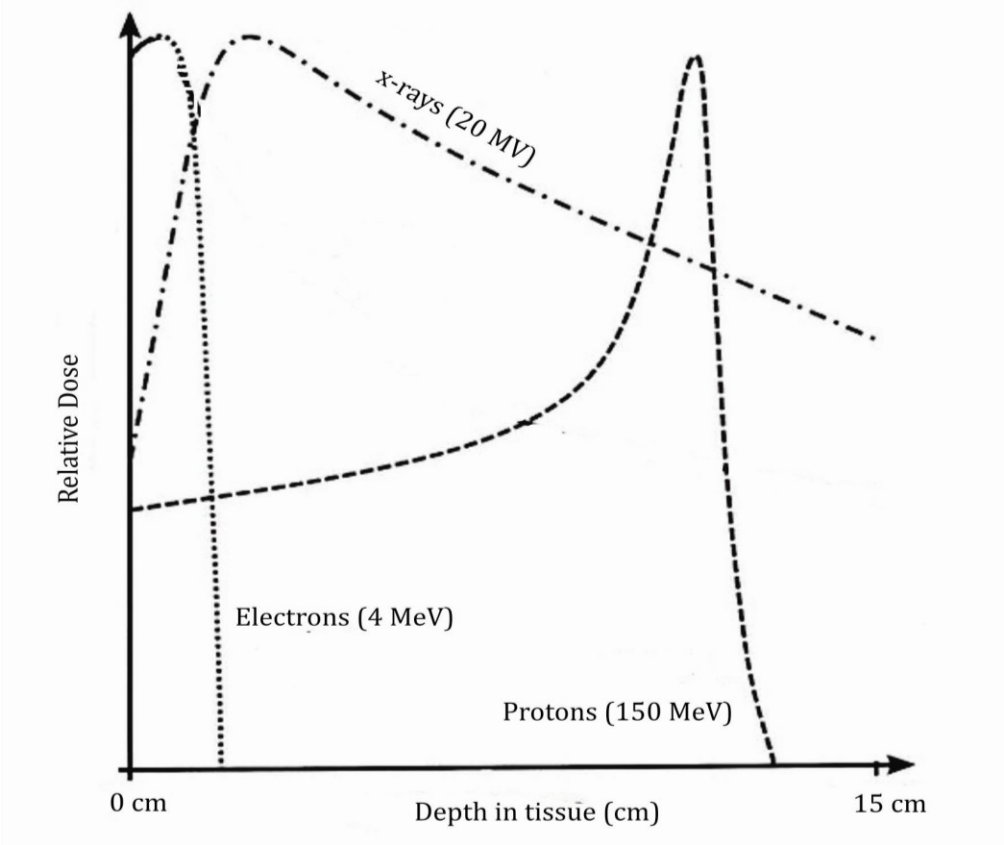

Figure 2.4: Comparison of depth dose curve for x-rays (20MV), electrons (4MeV), and protons (150 MeV) beams. Picture taken from (Wikimedia, 2013).

Dose distributions from x-rays and protons in a patient with medulloblastoma are shown in the Figure 2.5 (Terezakis et al., 2011). In this study, the dose distribution due to x-rays and proton is shown for craniospinal irradiation, i.e. spinal column is irradiated to prevent the spread of malignant cells via the spinal fluids. In the image, different colors represent dose distribution with red corresponding to the highest dose and blue corresponding to the lowest dose. The top figure (A) shows the dose distribution due to an x-ray beam and the bottom figure (B) shows the dose due to proton beam. As can be seen from this figure, for x-rays, healthy tissue beyond the spinal column receive significant dose, whereas, proton beam deposits negligible dose beyond the spinal column. Clinically, the advantage of precise deposition of dose has placed proton radiotherapy as a superior modality compared to x-rays and electron radiotherapy (Dowdell, 2011). For this reason, proton radiotherapy has been proving effective in critical cases such as tumors in pediatric patients (Dowdell), tumors in head and neck (Steneker et al., 2006, Dowdell, 2011), and ocular tumors (Dendale et al., 2006).

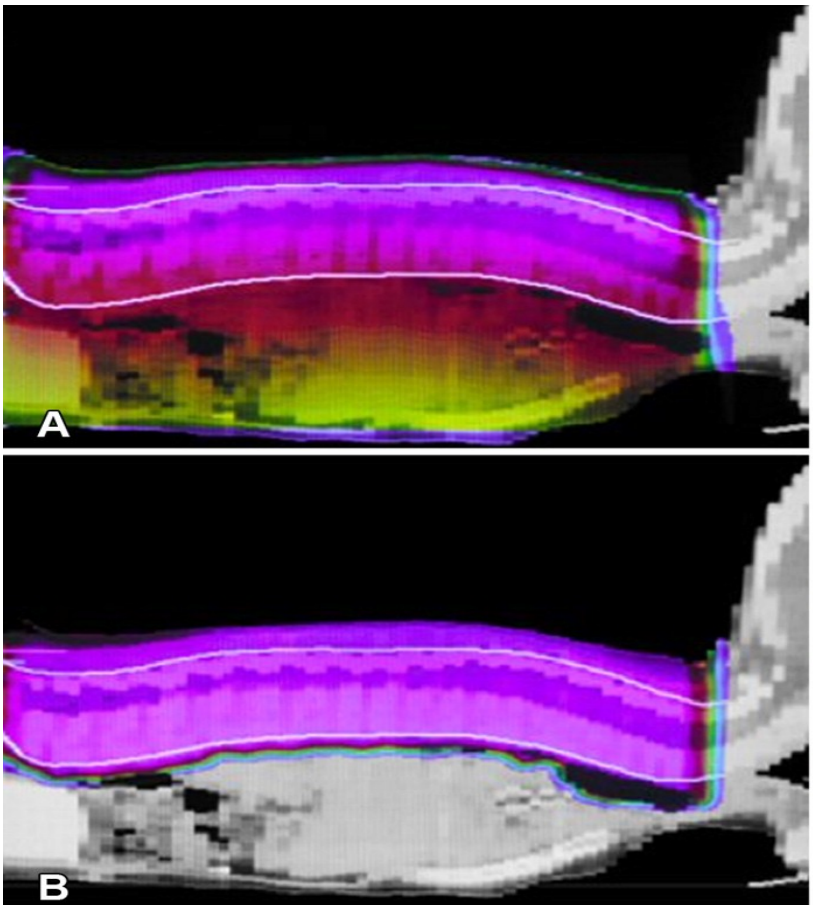

Figure 2.5: A comparison of dose distribution in a patient due to photon and proton beam for medulloblastoma (Terezakis et al., 2011).

2.4 *History of proton radiotherapy and present status*

Among different modes of radiation therapy, the use of proton beam has recently started gaining in popularity. In 1946, Robert Wilson first suggested that the beams of energetic protons can be employed in the treatment of cancer (Wilson, 1946). The key points that he made at that time were: a) the relatively larger mass of

proton compared to x-rays and electrons would cause less scattering, better confining the radiation to the tumor volume, and b) the greater energy deposition of protons at the end of their range would allow highly localized irradiation that would spare nearby healthy tissues. Following Robert Wilson's suggestion, different groups started to investigate the biological effects of energetic charged particles. The first studies were conducted by Tobias et. al. (ICRU, 2007) in 1952 at the University of California Berkley. This group reported the effect of high whole body doses that would kill fifty percent of tested cell population in the laboratory mice. During that time, few other groups were involved in the investigation in finding the biological effects on experimental animals from exposure to energy protons.

The first use of proton beams on a human patient was also conducted at the University of California, Berkley. This work was designed to suppress the hormone production by the pituitary gland to control breast cancers. Since a high proportion of breast cancers are hormone dependent. For this purpose, pituitary glands of different experimental animals were irradiated with energetic protons. Following irradiation, a substantial reduction in the pituitary gland was observed. With this discovery, the Berkley group decided to conduct a phase-I clinical trial on human patients with breast carcinoma (ICRU, 2007).

In 1954, eight years after Robert Wilson's original suggestion, first patient was treated using protons at the University of California, Berkley (Tobias et al., 1958), Around 26 patients were treated in that study and several patients experienced

great clinical response. In 1957, the Berkley group expanded the study to investigate the clinical response of tumors with other heavy ion beams including helium, carbon and neon. During this period treatment was limited to only a few types of tumor. In addition, the treatment of deep seated tumors was not possible as the accelerator had not been designed for medical use and the energy of the beam was not high enough to penetrate to the greater depths within the patient's body.

In 1961, proton therapy began on a regular basis in USA using the 160 MeV synchrocyclotron at the Harvard University cyclotron laboratory. Patients with pituitary adenomas, intracranial tumors, and arteriovenous malformations (AVM) were treated using multiple narrow beams (ICRU, 2007). Following the irradiation, significant clinical responses were observed for the patients with pituitary adenomas and AVMs. Treatment with energetic protons of different sites of the body soon followed. At the same time, researchers started to consider the efficacy of a fractionated dose instead of one large dose. In 1973, Suit et. al. (ICRU, 2007) conducted such an study to investigate the efficacy of fractionated doses to malignant tumors. The favorable outcomes of their study soon led to treatment by the team and subsequently applied fractionated dose to several other types of tumors.

Outside of USA, in 1957 University of Uppsala, Sweden started treating patient using a 185 MeV proton beam and fractionated doses. Significant positive results were seen in patients with tumors of the uterus, cervix, nasopharynx, and head and neck.

Proton therapy started in Japan in1979, in Russia in 1967, in South Africa in 1993 (ICRU, 2007). During the period from 1950 to 1970, cancer treatment using proton beam was mostly carried out using accelerators built for physics research and this limited the treatment to only clinical cases. In the late 1970s, the availability of computers and advanced imaging technique made proton therapy more viable. The first purpose built accelerator for proton radiotherapy was installed in 1990 at Loma Linda University Medical Center in California (Slater, 1991).

Currently (up to March, 2013), there are 38 proton facilities operating around the world and 34 more are under consideration (PTCOG, 2013). Table 2.3 provides a full list of proton therapy currently in operation including the year of first treatment and total number of patient treated through March 2013. As of March 2013, more than 78,000 patients have been treated using proton radiotherapy. Also, the number of proton therapy facilities that have opened in the recent years clearly shows that proton therapy is rapidly gaining popularity.

Table 2.3: List of proton treatment centers currently in operation. Maximum proton energy, the year of first treatment, and total number of patient treated in each facility up to March 2013 is listed (PTCOG, 2013).

Institute	Location	Max energy	First	Patient
ITEP, Moscow	Russia	250	1969	4246
St. Petersburg	Russia	1000	1975	1386
PSI, Villigen	Switzerland	250	1996	1409
Dubna	Russia	200	1999	922
Uppsala	Sweden	200	1989	1267
Clatterbridge	England	62	1989	2297
Loma Linda	CA, USA	250	1990	16884
Nice	France	65	1991	4692
Osray	France	230	1991	5949
NRF ithemba Lab	South Africa	200	1993	521
IU Health PTC, Bloomington	IN, USA	200	2004	1688
UCSF/UC Davis	CA, USA	60	1994	1515
TRIUMF, Vancouver	Canada	72	1995	170
HMI, Berlin	Germany	72	1998	2084
NCC, Kashiwa	Japan	235	1998	1226
HIBMC, Hyogo	Japan	230	2001	3198
PMRC(2), Tsukuba	Japan	250	2001	2516
NPTC, MGH Boston	MA,USA	235	2001	6550
INFN-LNS, Catania	Italy	60	2002	293
SCC, Shizuoka Cancer center	Japan	235	2003	1365
STPTC, Koriyama-City	Japan	235	2008	1812
WPTC, Zibo	China	230	2004	1078
MD Anderson Cancer Center	TX, USA	250	2006	3909
UFPTI, Jacksonville	FL, USA	230	2006	4272
NCC, IIsan	South Korea	230	2007	1041
RPTC, Munich	Germany	250	2009	1377
ProCure PTC, Oklahoma city	OK, USA	230	2009	1045
HIT, Heidelberg	Germany	250	2009	252
UPenn, Philadelphia	PA, USA	230	2010	1100
CDH PC, Warrenvile	IL, USA	230	2010	840
HUPTI, Hampton	VA, USA	230	2010	489
IFJPAN, Krakow	Poland	60	2011	15
Mediopolis MRI, Ibusuki	Japan	250	2011	490
CNAO, Pavia	Italy	250	2011	58
ProCure PTC, Somerset	NJ, USA	230	2012	137
PTC Czech rso Prague	Czech Republic	230	2012	1
SCCA, ProCure PTC, Seatle	WA, USA	230	2013	1

2.5 *Spread out Bragg peak (SOBP)*

In proton radiotherapy, the tumor volume is placed inside the Bragg peak region to assure maximum dose deposition. But, usually the width of the Bragg-peak of a proton beam is not wide enough to completely cover a tumor volume. The enlargement of Bragg peak is therefore required to cover a practical size of a tumor. The uniform enlargement of the Bragg peak region is called the spread out Bragg peak (SOBP). In practice, several Bragg peaks are combined together to achieve a desired SOBP for the uniform dose delivery at the treatment site. During treatment, this is usually done by running the proton beam either through an appropriate range modulator or ridge filter (Chu et al., 1993).

Figure 2.6: A common range modulator wheel used in proton radiotherapy. Picture taken from (Schlegel et al., 2006).

A range modulator consists of an absorber of variable thickness on a circular rotating disk as shown in Figure 2.6. The modulator wheel usually rotates about 10 Hz where the combination of discrete absorber thicknesses produces a temporal variation in beam energy (Koehler et al., 1977). The absorber is made of a combination of low-Z (Lexan or polycarbonate) and high-Z (lead) material (Schlegel et al., 2006). The low-Z material slows down the beam with little scattering while the high-Z material adjusts the scattering at each depth. Each absorber thickness corresponds to an individual Bragg peak and each Bragg peak is assigned with an individual weighting factor. A weighted sum to the series of individual Bragg peaks is done to produce the desired SOBP (Schlegel et al., 2006).

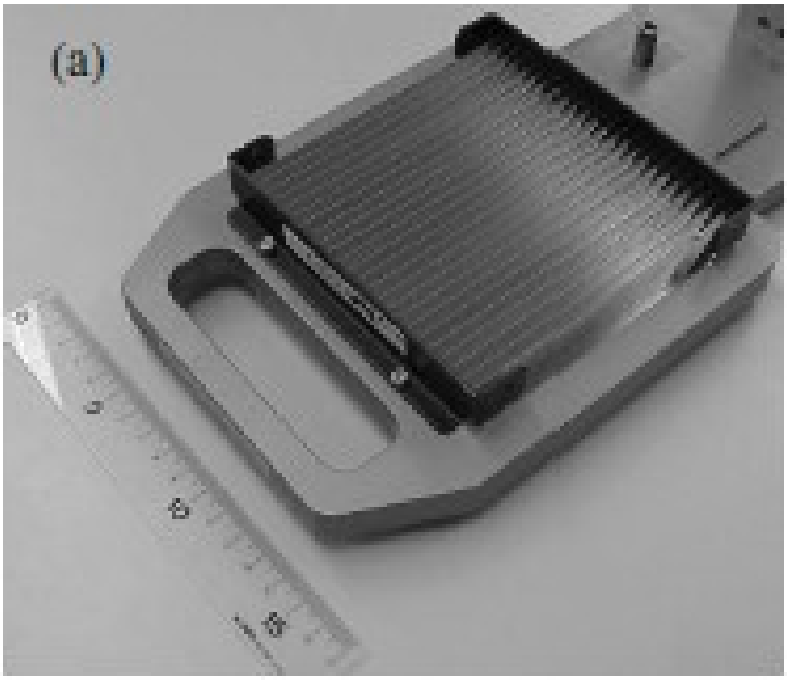

Figure 2.7: An example of basic ridge filter (Akagi et al., 2003).

A ridge filter is a typically stationary device. An example of typical ridge filter is the bar ridge filter shown in

Figure 2.7. A bar ridge filter uses about 30-50 bars where aluminum is used as the bar material because aluminum reduces scattering compare to other metals. The working principle of ridge filter is similar to the range modulator wheel except that it is stationary and it usually does not use any high Z material. In a ridge filter, the use of low Z metal allows a reduction in scattering that eventually helps to reduce the modulator effects in the final dose distribution in the patient. However, depending on the beam delivery technique, both range modulator and ridge filter have their place in the treatment.

Multiple absorbers in the range modulator or various bars in the ridge filter forms the required SOBP. An example of an SOBP for 200 MeV (maximum energy) proton beam using a range modulator is shown in Figure 2.8. As can be seen from the figure, each absorber thickness corresponds to a particular depth and the increasing depth of the absorber leads to a decreasing depth of the Bragg peak. Since each individual Bragg peak is assigned with a particular weight, the desired SOBP is produced by performing a weighted average of all the Bragg peaks.

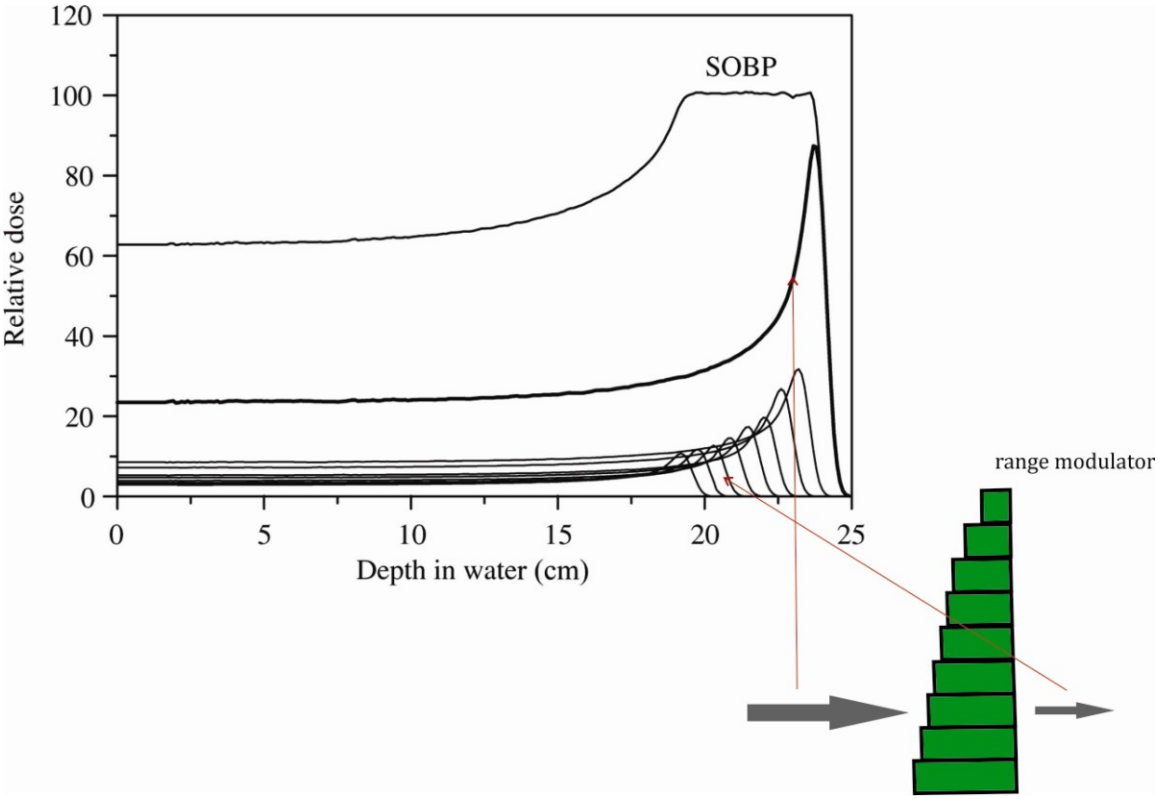

Figure 2.8: Illustration of the SOBP production using a range modulator for the maximum 200 MeV proton energy (ICRU, 2007).

2.6 *Beam delivery techniques*

Primary proton beams that are extracted from an accelerator are nearly monoenergetic and possess small lateral dimensions. For the practical use, the beam must to conform to the dimensions of the tumor, i.e. the beam must be modified both laterally and longitudinally. The modification of the beam is done by a beam delivery system in a treatment facility. Currently, there are two types of beam delivery systems available: passive scattering and active scanning. In general, passive scattering employs scattering material in the beam path for scattering, while active scanning employs dynamic scanning approach to irradiate the tumor volume.

Although passive scattering system is more common than active scanning system, active scanning is considered to have the following advantages over passive scattering system (Albertini, 2011): a) may not require any beam shaping components like range modulator, patient specific aperture, range compensator, etc. to achieve dose conformity, thereby reducing secondary radiation exposure, b) greater efficiency, i.e. the number of protons required to achieve a total dose in a given volume is much less in active scanning than passive scattering, so healthy tissue receives less dose, and c) inherently flexible in clinical use.

2.6.1 Passive scattering technique

Most of the treatment facilities currently in operation use the passive scattering method (Zheng et al., 2007a). This method may use a single scattering material or double scattering materials to scatter the beam. In the single scattering approach, a single piece of high-Z material (e.g. lead) is used for the lateral spreading of the beam and in double scattering technique, a second scatterer is placed further downstream to spread the central part of the beam as shown in Figure 2.9. The second scatterer typically uses a combination of low and high-Z materials. Because of the scattering process, the single scattering method can keep only 10% of the beam within the central uniform region. This makes the single scattering method efficient only for small treatment sites. The double scattering method, on the other hand, is efficient for larger treatment fields, where up to 45% of the beam remains

within the central region (Gottschalk, 2004). Depending on the required treatment field, both single and double scattering methods are currently in use.

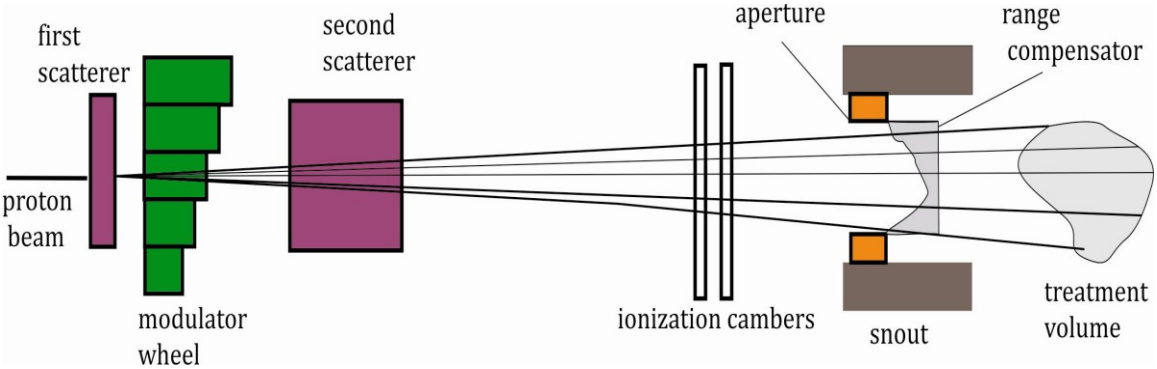

Figure 2.9: Schematic diagram of passive scattering system for proton radiotherapy.

As shown in Figure 2.9, when the beam enters the beam delivery system, it passes through a series of beam shaping components. The beam starts trough a first scatterer, then continues through the range modulator wheel, a second scatterer, ionization chambers and finally passes through a snout that contains a patient aperture and a range compensator. The first and second scatterers spread the beam laterally, while the range modulator spreads the beam longitudinally. The combination of range modulator and scatterers spread the beam both laterally and longitudinally. The ionization chambers closer to the snout monitor the beam flatness and symmetry, as well as the amount of delivered dose. The beam is finally shaped at the snout by the aperture and the range compensator.

A snout (Figure 2.9) is a removable component that contains the patient aperture and range compensator. The snout is attached at the end of a fixed beam delivery

system. The size of the snout varies depending on the treatment field size. The aperture is a patient specific custom milled collimator (Figure 2.10) that shapes the treatment field to a specific target profile. Usually, apertures are made out of brass because brass provides the best value in terms of price, weight, and production of secondary radiation. The patient specific range compensator is another custom made piece (Figure 2.10) which is used to shape the distal part of the dose distribution. Plastic material is commonly used for range compensator. The combination of patient aperture and range compensator conform the dose distribution to the contours of the treatment volume.

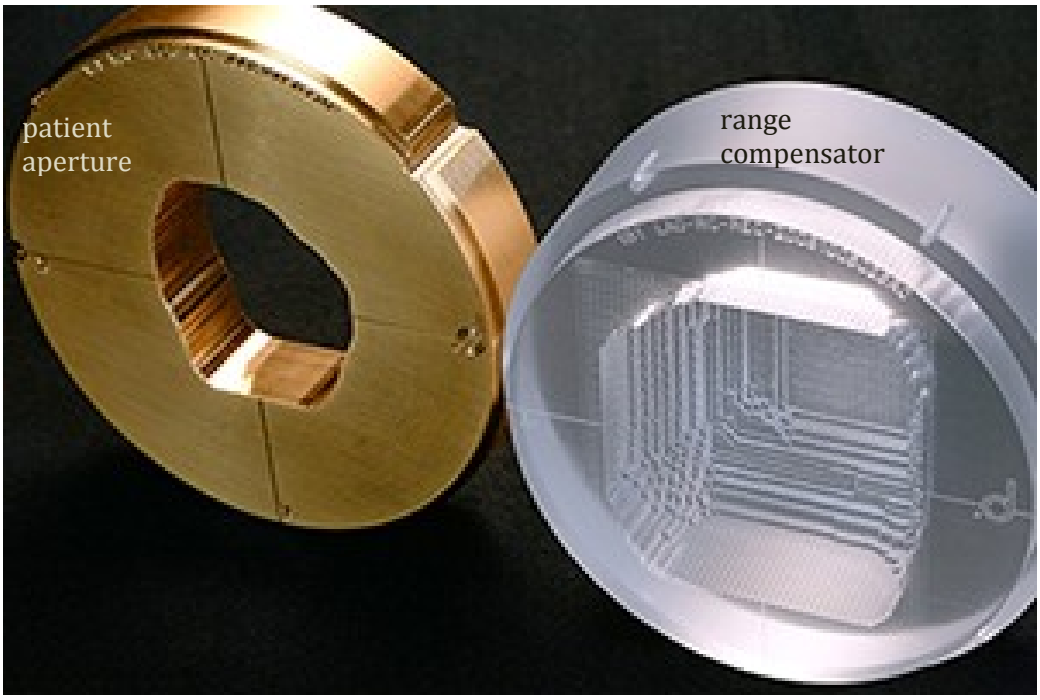

Figure 2.10: A custom patient aperture (left), and a custom made range compensator (right). Picture taken from (Decimal, 2013).

2.6.2 Active Scanning Technique

The active scanning method is an alternative to the passive scattering method. In 1980, Kanai et al. (Kanai et al., 1980) first suggested this alternative approach and later this technique was implemented at different facilities around the world (Albertini, 2011). The principle behind the active scanning system is essentially simple, i.e., protons are charged particles and can be deflected by magnetic fields. Using this approach, the narrow pencil beam is no longer required to be broadened by scattering method; instead it can be scanned over the treatment volume using appropriately varying magnetic fields. For this purpose, scanning magnets are used to generate the required magnetic fields so that the beam can be scanned onto the target. The scanning along the x-y plane of the treatment volume can be done using a particular magnetic field while scanning in depth is achieved by means of energy variation (Farr et al., 2008). The combination of the scanning ability and the energy variation allows this technique to place each individual Bragg peak anywhere inside the tumor volume.

Active scanning systems are classified into two categories (Zheng et al., 2012): a) pencil beam scanning, and b) uniform scanning. The basic differences between pencil beam scanning and uniform scanning are: a) pencil beam scanning may not require any beam shaping components while uniform scanning system requires beam shaping components (Goitein, 2008), b) pencil beam scanning is capable of delivering a beam of variable intensity during scanning, while uniform scanning employs a beam of uniform intensity.

2.6.2.1 Pencil beam scanning

Pencil beam scanning system uses scanning magnets to scan a narrow pencil beam (few mm) of variable intensity onto different planes (layers) of the treatment volume. The scanning along the depth is done by means of energy variation. A schematic diagram of a pencil beam scanning system is shown in Figure 2.11. In this method, scanning starts with the deepest layer of the target and covers a predetermined set of spots on that layer. The energy is then reduced and moves to a relatively shallower layer and covers all the predetermined spots on that layer again. This process continues until all the spots on the treatment volume have been covered.

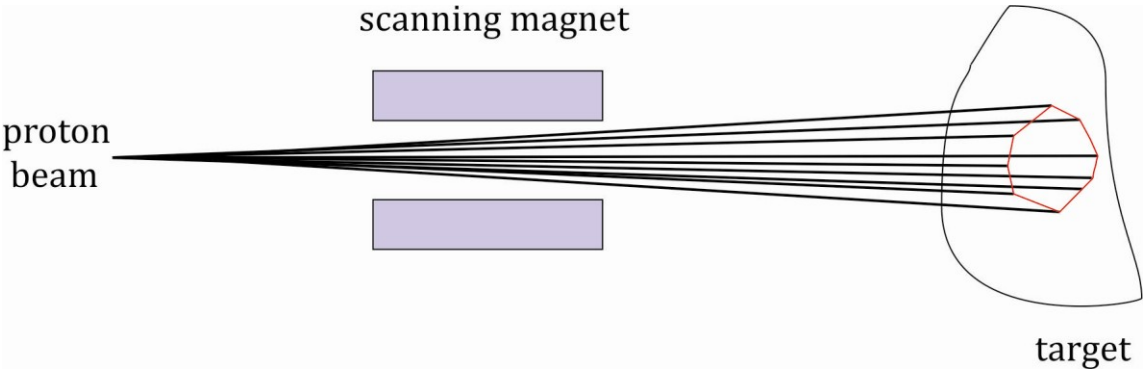

Figure 2.11: Schematic diagram of spot scanning delivery system in proton radiotherapy.

Pencil beam scanning can be done primarily in two different ways: spot scanning and raster or continuous beam scanning (Schlegel et al., 2006). In spot scanning, a constant magnet setting is used to deliver the dose to a given spot on a particular layer of the target (Kanai et al., 1980). After that spot is covered, the beam is then

turned off and magnet settings are changed to new values to irradiate the next spot. This process employs different magnet settings for different spots until all the predetermined spots on the tumor have been covered. Raster or continuous beam scanning is very similar to the spot scanning method except that the beam is not turned off while it moves from one spot to the next. The beam remains on during the entire scanning process.

2.6.2.2 Uniform scanning

Uniform scanning system is recently developed beam delivery system. In general, a uniform scanning system is a hybrid of active scanning and passive scattering. This process uses sweeping magnets as like in active scanning to steer the beam and also beam shaping components (snout) as in passive scattering to conform the beam to the target. In this method, a beam of uniform intensity is used to scan different layers of the treatment volume. A schematic diagram of a uniform scanning system (IBA Louvian-la-neuve, Belgium) is shown in Figure 2.12.

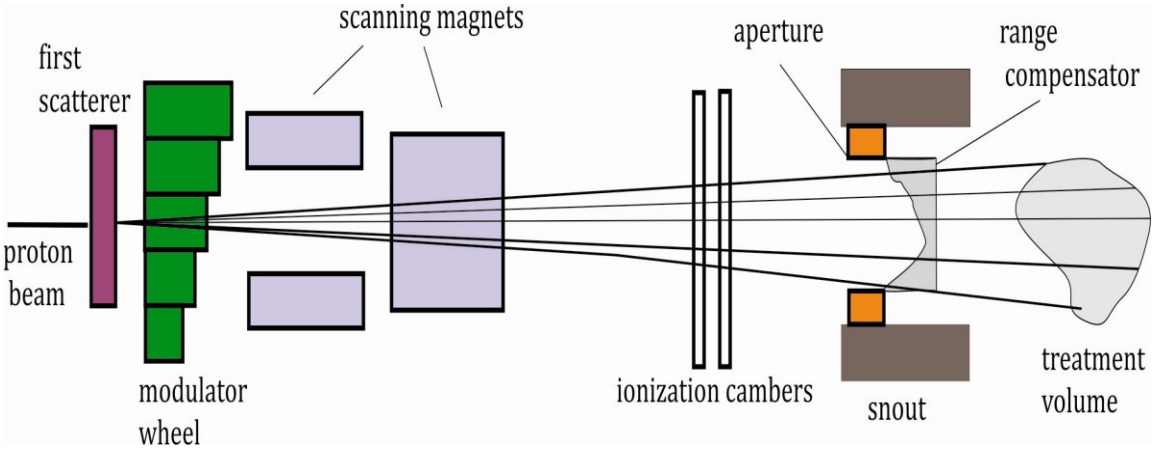

Figure 2.12: Schematic diagram of IBA uniform scanning nozzle. The components in the nozzle is not in scale.

As shown in the figure, the proton beam passes through different beam shaping components, similar to the passive scattering system, except that instead of a second scatterer this method uses scanning magnet to cover lateral width of the treatment volume. The beam starts with the first scatterer, and then continues through the range modulator, scanning magnets, ionization chambers and finally the snout. The initial enlargement of the beam is done by the first scatterer. The combination of modulator wheel and the first scatterer lowers the beam energy to the required treatment depth. As the wheel rotates, the different thicknesses of absorber material adjust the beam to different depths of the treatment volume. As the beam passes through the modulator, the sweeping magnets deflect the beam by sweeping back and forth with a particular frequency. This creates a beam of uniform intensity commonly known as an uncollimated beam (Zheng et al., 2012). As the uncollimated beam continues, the ionization chambers monitor the beam symmetry, uniformity,

and the amount of delivered dose. Finally, the beam is shaped according to the tumor using the patient aperture and range compensator contained in the snout.

The working mechanism of uniform scanning system is similar to pencil beam scanning. During scanning, the beam starts with the distal layer of the target and irradiates that layer. The beam then moves to a relatively shallower layer and irradiates that layer and the process continues until the proximal edge of the treatment volume is covered.

This study investigates the dose equivalent due to secondary neutrons created by the uniform scanning system as described above. This uniform scanning system is currently in operation at the Procure Proton Therapy Center in Oklahoma City, OK. Both experiment and simulation work was carried out for this study. For the simulation, a simplified version of the uniform scanning system was used. See Sections 5.2 and 5.3 for details about the experimental and simulation set ups.

CHAPTER 3

SECONDARY NEUTRONS

This chapter describes the nuclear processes responsible for secondary neutron production in proton radiotherapy. Dominant nuclear interactions for the production of secondary neutrons in therapeutic proton energies (50 to 250 MeV) are described. The level of neutron production largely depends on the design of the beam delivery device and on the primary proton energy. Neutron interactions with tissue and the reasons behind using water as alternative to tissue are also discussed.

3.1 *Secondary neutrons in proton radiotherapy*

In proton radiotherapy, different beam shaping components including the scatterer, range modulator, patient collimator and range compensator are used to conform the beam to the target. The interaction of energetic protons with these devices creates secondary particles through non-elastic nuclear interactions. The type and energy of the secondary particles produced in the interaction depend on the incident proton energy and the composition, density, and geometry of the interacting medium. These secondaries consist of different types of particles including neutrons, protons, electrons, alpha particles, and heavier fragments. Among them, the exposure from

neutrons could be potentially damaging as neutrons have higher relative biological effectiveness (RBE).

The level of secondary neutron production strongly depends on the type of beam delivery system because each beam delivery system uses different beam shaping components. Of the various beam shaping components, the patient specific aperture can be a major source of secondary neutrons (Jiang et al 2005, Mesoloras et al 2006, Zheng et al 2007, Zacharatou Jarlskog et al 2008, Perez-Andujar et al 2009). In addition, because the patient specific aperture is placed close to the patient, neutrons produced in this component can contribute significantly to the total patient dose outside the treatment volume compared to the neutrons contribution from other components. It is important to note that during treatment, the field size is always chosen to be larger than the patient specific aperture. This is because the treatment facility is limited by the number of field sizes that an accelerator can produce. Due to this limitation, a significant portion of the beam is stopped by the aperture during treatment. This leads to higher rates of proton induced nuclear interactions and thus to increased production of secondary neutrons.

Two nuclear processes, intranuclear cascade and nuclear evaporation are responsible for the production of secondary neutrons in the energy range of 50 to 250 MeV primary protons (ICRU, 1978). Figure 3.1 shows a graphical representation of intranuclear cascade and evaporation process. For proton energies greater than 50 MeV, the intranuclear cascade process is particularly

important (Benton, 2004). In this process, protons, neutrons, alpha particles and occasionally heavier nuclei are produced as a result of nuclear interactions between incident particles and the target nucleus. The emitted particles in intranuclear cascade possess energy lower than the incident particles (Figure 3.1) and move in the forward direction, i.e. in the direction of the primary beam. These particles can undergo further nuclear interactions, known as an extra nuclear cascade. However, the probability to initiate an extra nuclear event in proton radiotherapy is small because the energy required for such events is greater than a few hundred MeV. The energy of the secondary neutrons due to intranuclear cascades start around ~10 MeV and can be as high as the incident proton energy (Zheng et al., 2007a).

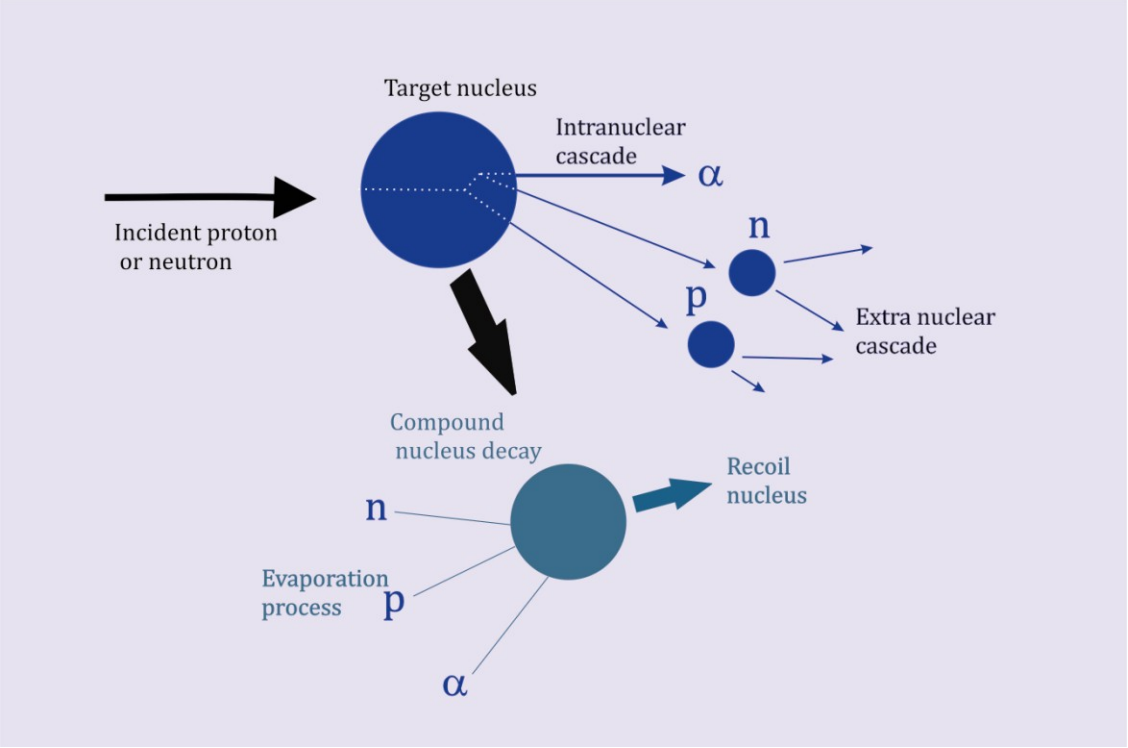

Figure 3.1: Illustration of intranuclear cascade and evaporation process (ICRU, 1978).

The evaporation process, on the other hand, occurs in multiple steps processes following an intranuclear cascade. Alternatively, a target nucleus can absorb an incident proton or neutron and then undergo an evaporation interaction. After the release of the particles due to intranuclear cascade or the absorption of a proton or neutron, the target nucleus is often left in an excited and unstable state (Figure 3.1) and is referred as a compound nucleus (ICRU, 1978). The compound nucleus achieves stability by evaporating neutrons, protons, and alpha particles. The particles due to evaporation are emitted isotropically. The energy of the secondary neutrons due to evaporation process range from 0 to 10 MeV (Zheng et al., 2007a). The energy of the secondary neutrons created in proton radiotherapy primarily contains two peaks: a) peak due to evaporation neutrons (<10 MeV), and b) peak due to intranuclear cascade neutrons (>10 MeV).

3.2 *Neutron interactions with matter*

A neutron can interact with a target nucleus in a different number of ways, where the interaction probability depends on the energy of the incident neutron and the type of target nucleus. Various types of interactions can take place and the probability of any of such interaction is known as the cross section, having dimensions of area, i.e. cm^2. An example of different types possible nuclear interactions is shown in Figure 3.2.

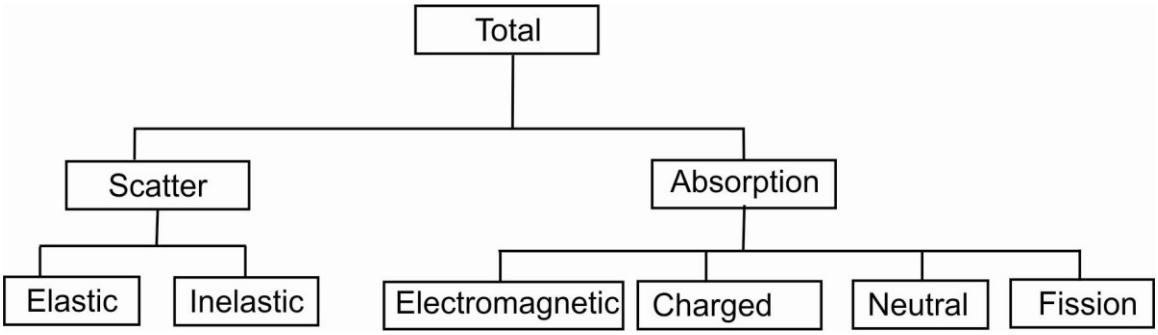

Figure 3.2: Different types of neutron interaction (Rinard, 1991).

As shown in Figure 3.2, two major types of interactions are possible: a) scattering, and b) absorption. Scattering events are further divided into elastic and inelastic interactions, whereas absorption events are categorized into electromagnetic, charged, neutral, and fission interactions. In scattering interactions, the incident neutron is scattered by a target nucleus and as a result of this interaction, the direction and speed of the incident neutron changes. In this process, the target nucleus remains intact, the total kinetic energy of the event is conserved and the internal states of the target nucleus and neutron remain unchanged. If the total kinetic energy in scattering is not conserved, the scattering is known as inelastic scattering. A fraction of energy in inelastic scattering is spent on the internal rearrangement of nucleons inside the nucleus (Rinard, 1991).

In the absorption process, a neutron is absorbed by a target nucleus. Following absorption of a neutron by a target nucleus, the kinetic energy carried by the neutron will excite the nucleus to one of its higher energy states and the de-excitation of the nucleus may lead to one of several outcomes: a) the emission of

electromagnetic radiation i.e. gamma rays, b) charged particles such as protons, deuterons, and alpha particles may emit, c) the emission of neutrons, and d) a fission event can take place, i.e. the nucleus can split into two or more fragments including neutrons (Rinard, 1991).

The total cross section for neutron/target interactions is energy dependent. Depending on energy, neutrons are classified as: a) fast neutrons (> 500 keV), b) intermediate neutrons (10 keV-500 keV), c) epithermal neutrons (0.5 eV-10 keV), and d) thermal or slow neutrons (< 0.5 eV). Fast and intermediate neutrons, in general, undergo scattering interactions while thermal or epithermal neutrons undergo absorption interactions.

3.2.1 Neutron's interaction with tissue and the rationale for using water as tissue replacement

The interaction of neutrons on tissue depends on the interaction process of neutrons with each tissue component. The most common elements in human body are hydrogen, carbon, and oxygen and the total interactions depend on the individual interaction with each of these elements. Neutrons with energy greater than 1 MeV (fast neutrons) interact with carbon and oxygen nuclei in tissue through inelastic processes and can release alpha particles. These alpha particles deposit their energy to the tissue mass. Neutrons with energy 10 keV up to 1 MeV (intermediate energy neutrons) interacts elastically with the nuclei of hydrogen

atoms (protons). In this process, the energy transfer causes the creation of recoil protons while the incident neutron elastically scatters off a hydrogen nucleus. Thermal neutrons (< 0.5 eV), on the other hand, often transfer energy through the absorption process.

The leading mechanism of energy transfer by neutrons to tissue is elastic scattering, where neutrons scatter of the hydrogen nuclei of water (Howell, 2010). This is because: a) the similar mass of hydrogen and neutron causes neutron to transfer maximum energy via elastic scattering, b) hydrogen has large neutron scattering cross section, and c) hydrogen is the most abundant element in tissue.

An example of total cross sections for incident neutrons up to 20 MeV on hydrogen, carbon, and oxygen as a function of energy are shown in Figure 3.3 (NNDC, 2013). As can be seen from the figure, the total cross section of neutrons on carbon, hydrogen and oxygen either follows a decreasing trend with energy or stay constant with increasing neutron energy. The decreasing trend of total cross section is due to elastic interactions, while the constant trend is due to inelastic interactions. The peaks at around 0.1 to 10 MeV for carbon and oxygen nuclei are called resonance peaks. Resonance peaks occur when an incident neutron excites the target nucleus to one of its excited nuclear states. For the hydrogen nucleus (protons), resonance peaks are not visible because protons do not possess any excited nuclear states at these energies.

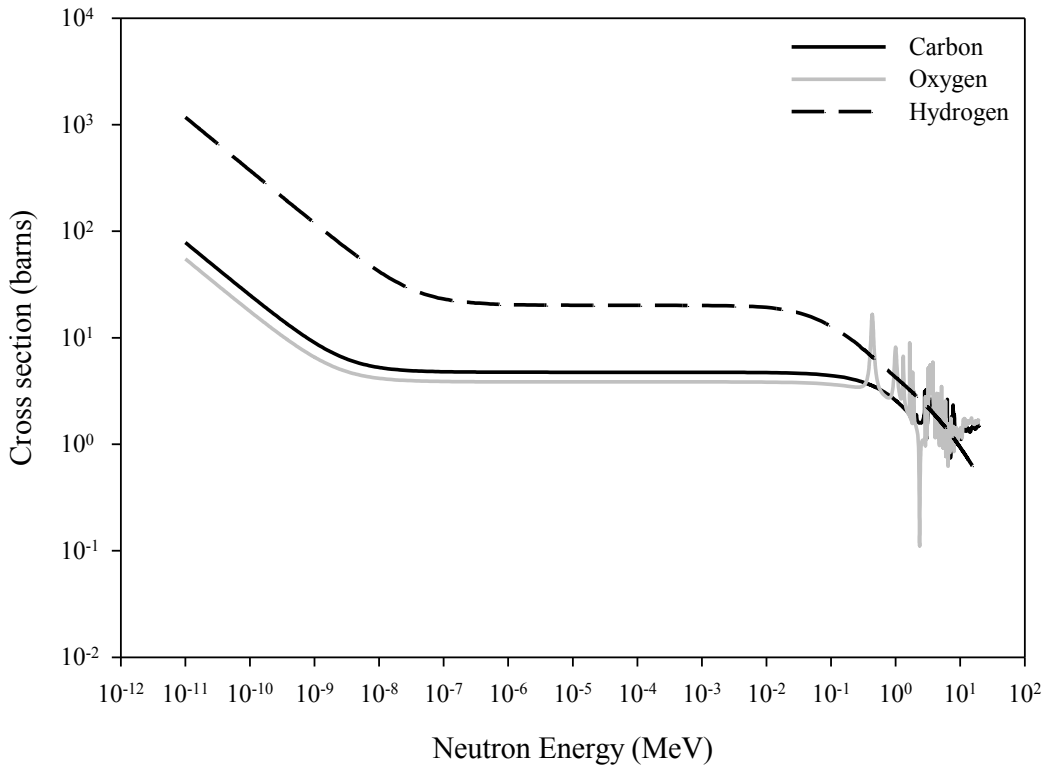

Figure 3.3: The average total cross section of neutron for carbon, oxygen and hydrogen as a function of incident neutron energy (NNDC, 2013).

Figure 3.3 shows that hydrogen has about an order of magnitude greater total cross section than do carbon and oxygen for the same neutron energy. This means that hydrogen content in tissue dominates the neutron response. For this reason and also due to the similarity in the atomic mass percentages (Table 3.1) of hydrogen in water and in tissue (ICRU muscle), the difference in total cross section between water and ICRU muscle are negligible. This is shown in Figure 3.4, where the solid line represents the neutron cross section for neutrons on water and dotted line represents neutron cross section on ICRU muscle (for clarity, the total cross section on water is multiplied by a factor of 10). Because of the similarity in total cross sections of neutron on water and ICRU muscle and since CR-39 plastic nuclear track

detector possesses a tissue like sensitivity to neutrons, this study uses water as tissue replacement in the FLUKA simulations.

Table 3.1: Atomic percentages for ICRU muscle and water (ICRU, 1983).

Content	Atomic percentages (%)	
	ICRU muscle	water
H	63.3	66.67
C	6.4	
O	28.5	33.33
Other	1.8	

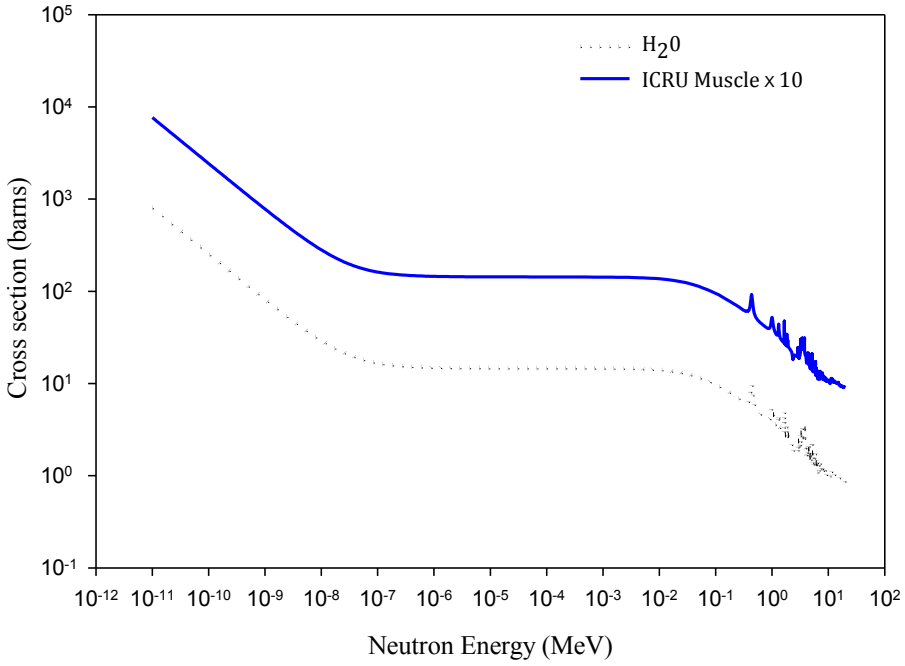

Figure 3.4: The average total cross section of neutron for ICRU muscle and water as a function of incident neutron energy(NNDC, 2013). ICRU muscle cross section is multiplied by 10 in the graph to distinguish it from the cross section for neutrons on water .

CHAPTER 4

DOSIMETRIC QUANTITIES AND RADIATION LEAKAGE

Dosimetric quantities are essential to quantify a given radiation environment. For example, the energy of the incident radiation per unit mass or absorbed dose is crucial in understanding the radiation exposure. But, absorbed dose alone cannot explain the radiation sensitivity of human tissue and that is why dose equivalent is measured. Dose equivalent is based on absorbed dose, but includes effectiveness in producing damage. This chapter describes the dosimetric quantities including particle fluence, LET (linear energy transfer), absorbed dose and dose equivalent. Dose equivalent using CR-39 plastic nuclear track detector is determined based on particle LET. In FLUKA simulations, fluence to dose conversion coefficients are used to determine dose equivalent. Standard guidelines for radiation leakage in radiation therapy are also described in this chapter.

4.1 *Particle Fluence*

Particle fluence is important for the quantification of radiation exposure in radiation therapy. According to the International Commission on Radiation Units and

Measurements (ICRU), particle fluence, Φ, is defined as the number of particles, dN, that cross a unit area, dA (ICRU, 1998a):

$$\Phi = \frac{dN}{dA}. \tag{4.1}$$

The SI unit of particle fluence is particles/m^2. For isotropic or nearly isotropic situations, fluence is corrected for solid angle, Ω:

$$\Phi = \frac{dN}{dAd\Omega}, \tag{4.2}$$

where the unit is cm^{-2}sr^{-1}.

4.2 *Linear Energy Transfer (LET)*

Linear energy transfer (LET) refers to the energy deposition per unit path length by the charged particles as they travel through a medium. The term LET represents the local energy deposition in a medium and depends on the radiation type and the target material. LET is determined by the rate of energy loss in the medium as:

$$LET = \frac{dE}{dl} \tag{4.3}$$

where dE denotes the energy loss in the length, dl, of the stopping medium. The SI unit for LET is Joules/meter, but is more commonly expressed in keV/μm.

LET is related to mass stopping power and linear stopping power. The term mass stopping power (for a material of density of ρ) for charged particles is represented as (ICRU, 1998b):

$$\frac{S}{\rho} = \frac{1}{\rho}\frac{dE}{dl}, \tag{4.4}$$

The term S is the linear stopping power. Mass stopping power and linear stopping power are similar except that mass stopping power is independent of density of the material. The SI unit of mass stopping power is J.m^2/kg but in practice usual has units of MeV·cm^2/g. Mass stopping power includes the contributions from electronic, radiative, and nuclear stopping power and can be expressed as:

$$\frac{S}{\rho} = \frac{1}{\rho}\left(\frac{dE}{dl}\right)_{el} + \frac{1}{\rho}\left(\frac{dE}{dl}\right)_{rad} + \frac{1}{\rho}\left(\frac{dE}{dl}\right)_{nuc}. \tag{4.5}$$

The term $\left(\frac{dE}{dl}\right)_{el}$ represents electronic stopping power due to collision with electrons in the medium, $\left(\frac{dE}{dl}\right)_{rad}$ represents radiative stopping power due to bremsstrahlung emission, and $\left(\frac{dE}{dl}\right)_{nuc}$ represents nuclear stopping power due to elastic coulomb collisions. The leading contribution in stopping power is primarily due to electron collisions and can be estimated using the Bethe-Bloch formula described in Equation 2.1.

According to ICRU report No. 60 (ICRU, 1998b), linear energy transfer (LET) is also referred as restricted linear stopping power, L_Δ, and can be expressed as:

$$L_\Delta = \frac{dE_\Delta}{dl}. \tag{4.6}$$

The term dE_Δ in Equation (4.6) accounts the energy loss due to electronic collisions as the charged particles traverse through a medium of length *dl*. Equation (4.6) does not include the kinetic energy of secondary electrons freed from atoms in excess of

"Δ". In other words, the subscript "Δ" sets the limit in eV above which the kinetic energy of secondary electrons is not included. ICRU Report No. 60 also presents Equation (4.6) as (ICRU, 1998a):

$$L_{\Delta} = S_{\text{elec}} - \frac{dE_{\text{KE},\Delta}}{dl}. \tag{4.7}$$

S_{elec} represents electronic stopping power and the second term specifies the sum of kinetic energies of secondary electrons released greater than Δ. The term L_{Δ} is known as the restricted linear stopping power and can also be written as LET_{Δ}. The linear stopping power that includes the kinetic energy of all the released secondary electrons is called unrestricted linear stopping power and is written as LET_{∞}. For example, LET_{200}CR-39 refers to the restricted linear stopping power in CR-39 PNTD without the kinetic energy of released secondary electrons greater than 200 eV, whereas $\text{LET}_{\infty}H_2O$ represents the total (or unrestricted) linear stopping power in water. In this study, unrestricted linear stopping power has been used to represent LET unless otherwise stated.

4.3 *Absorbed dose and dose equivalent*

Absorbed dose refers to the amount of energy, *dE,* absorbed per unit mass, *dm*, of a material as a result of radiation exposure and can be expressed as:

$$D = \frac{dE}{dm}, \tag{4.8}$$

SI unit of the absorbed dose is Gray (Joule/Kg).

Dose equivalent refers the biological damage for an absorbed dose in matter. According to the International Commission on Radiological Protection (ICRP), dose equivalent is the product of the absorbed dose and LET dependent quality factor, Q (LET):

$$H = Q(\text{LET}) * D. \tag{4.9}$$

The SI unit of dose equivalent is the Sievert.

The quality factor, *Q,* has been adopted from annex A of ICRP Publication No. 60 (ICRP, 1991) as shown below:

$$Q(LET) = \begin{cases} 1.0, & \text{LET} < 10 \text{ keV/µm} \\ 0.32LET - 2.2, & 10 \text{ keV/µm} \leq LET \leq 100 \text{ keV/µm} \\ 300/\sqrt{LET}, & \text{LET} > 100 \text{ keV/µm}. \end{cases} \tag{4.10}$$

A plot of Q value against LET is shown Figure 4.1. It is important to mention that the quality factor is determined based on stochastic endpoints rather than deterministic endpoints. In stochastic processes there is no threshold for biological damage including the induction of cancer, whereas, in deterministic processes, a biological threshold is considered.

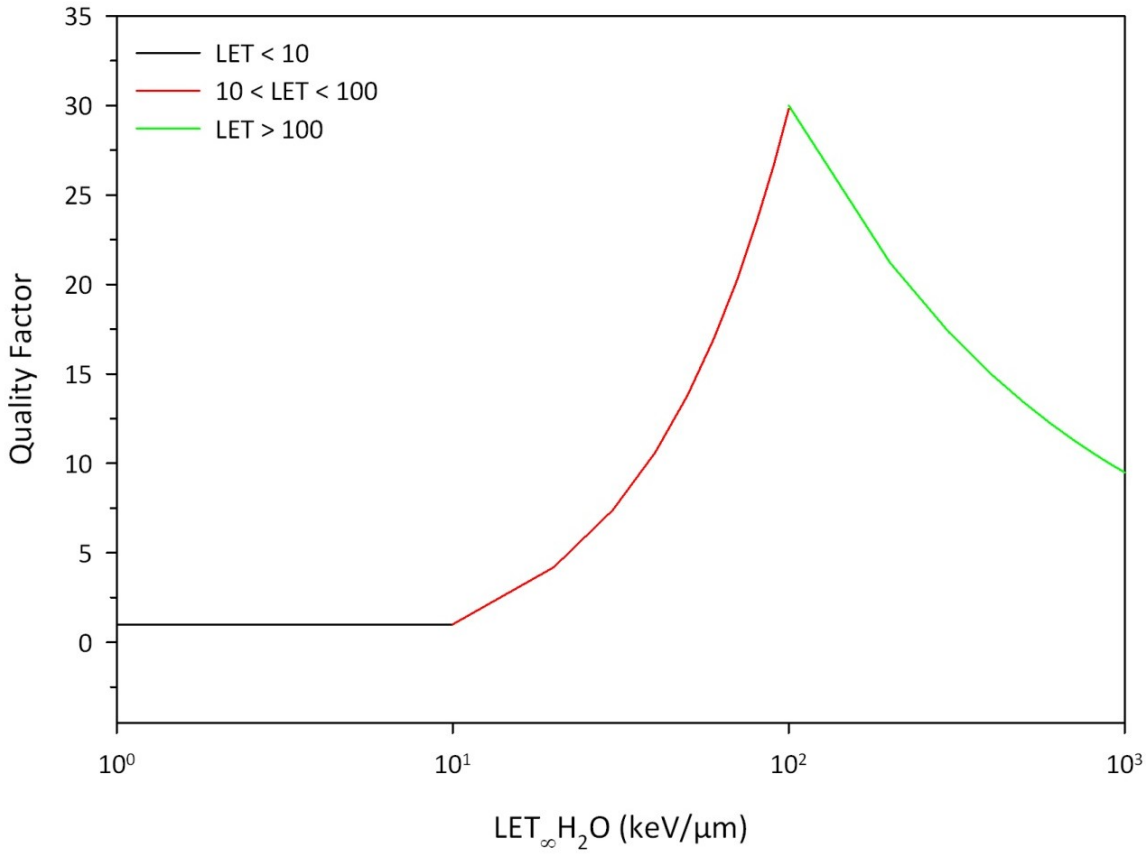

Figure 4.1**:** Quality factor, *Q*, as a function of LET as defined in ICRP Publication No. 60 (ICRP, 1991).

4.3.1 Determination of dose equivalent in CR-39 PNTD

For the determination of fluence, dose, and dose equivalent, from isotropic radiation on the surface of a CR-39 plastic nuclear track detector, consider the diagram shown in Figure 4.2.

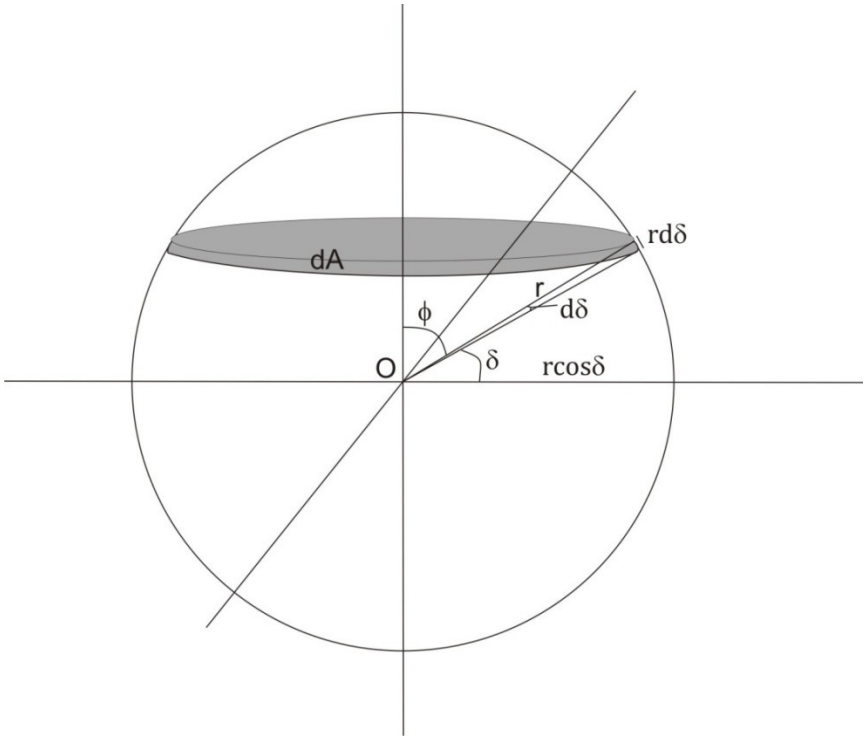

Figure 4.2: Geometry for solid angle calculation (Benton, 2004).

The sphere is centered at a point O on the surface of a nuclear track detector, where r is the radius of the sphere. Using a spherical coordinate system, the differential area, *dA,* on the surface of the sphere is:

$$dA = 4\pi r^2 \sin\phi \, d\phi \,, \tag{4.11}$$

where 4π has been included to account for the isotropic nature of the incoming radiation and ϕ represents the polar angle. From Figure 4.2, a relation between polar angle and dip angle δ (the angle at which particle intersect the detector surface) can be shown to be:

$$\sin\phi = \cos\delta. \tag{4.12}$$

Substituting Equation (4.12) into Equation (4.11) and using the definition of solid angle, it can be shown that:

$$d\Omega = \frac{\vec{n}.\overrightarrow{dA}}{r^2} = \frac{\sin\delta \; dA}{r^2}. \tag{4.13}$$

Using the definition of fluence:

$$\Phi = \frac{d^2n}{dAd\Omega} \tag{4.14}$$

and substituting Equation (4.11), (4.12), and (4.13) into Equation (4.14), it can be shown that:

$$\frac{dn}{dA}\int dn = \Phi 4\pi \int_{\delta_c}^{\pi/2} \cos\delta \sin\delta \; d\delta.$$

The term δ_c represents the track registration dip angle, i.e. the maximum angle at which a track will form for a given value of LET. After a little mathematical manipulation it can be shown that:

$$\Phi = \frac{n}{2\pi A \cos^2 \delta_c} \; .$$

The term $(2\pi A \cos^2 \delta_c)^{-1}$ is called weighting factor, *W*. Depending on the critical value δ_c, the weighting factor varies as a function of LET. Labeling each LET interval by *j*, the differential LET fluence can be expressed as:

$$\Phi_j = W_j n_j \; .$$

The integral LET spectrum can be found by adding the contribution from all LET intervals at which the integral fluence is measured:

$$\Phi(LET \geq LET_{min}) = \sum_{j=max}^{x} W_j n_j \; .$$

LET_{min} represents a lower threshold point at which the integral fluence is being counted. Utilizing this differential LET spectrum, differential LET dose spectrum can be found in units of Gray as:

$$D_j = \frac{1.602 \times 10^{-9}}{\rho} 4\pi \times W_j n_j LET_j \,. \quad (4.15)$$

Similarly, the differential dose equivalent can be found by multiplying dose with the quality factor Q:

$$H_j = \frac{1.602 \times 10^{-9}}{\rho} 4\pi Q_j W_j n_j LET_j \,. \quad (4.16)$$

Q_j represents the quality factor dependent on LET interval. The total dose and dose equivalent can be found by summing the differential dose and dose equivalent over appropriate LET values.

4.3.2 Determination of dose equivalent using FLUKA

FLUKA uses fluence to dose equivalent conversion coefficients for the determination of dose equivalent. The coefficients are determined based on radiation weighting factor, $w_{R,}$ described in ICRP publication No 74 (ICRP, 1996). The subscript "*R*" represents the type of radiation. A list of radiation weighting factors, $w_{R,}$ for neutron of various energy range is shown in Table 4.1 ((ICRP, 1991).

Table 4.1: Radiation weighting factor, w_R, as defined in ICRP-60 (ICRP, 1991) for neutron of different energy range.

Energy	w_R
<10 keV	5
10 keV to 100 keV	10
>100 keV	20
2MeV to 20 MeV	10
>20 MeV	5

Radiation weighting factors are employed in the calculation of equivalent dose, $H_{T,}$ and is recommended by ICRP, in 1991 (ICRP, 1991), to replace the LET dependent dose equivalent. The equivalent dose, H_T is (ICRP, 1991):

$$H_T = \sum_R w_R * D_{T,R,} \tag{4.17}$$

where $D_{T,R}$ is the absorbed dose average over the specific tissue or organ, T. There is another quantity related to dose equivalent is called effective dose and defined as, E (ICRP, 1991):

$$E = \sum_T w_T * H_{T,} \tag{4.18}$$

where w_T is the weighting factor for the tissue, T. The effective dose accounts the sum of the weighted equivalent doses in all tissues and organs of the human body.

FLUKA employs a spline fit over the conversion coefficients recommended by ICRP publication No 74 (ICRP, 1996) for the determination of dose equivalent. This is

shown in Figure 4.3, where fitted line is represented by AMB74 (red line) and ICRP coefficients are represented by ICRP74 (black star). As can be seen from the figure, the ICRP recommended conversion coefficients are limited to a few hundred MeV in neutron energy and undefined for the determination of dose equivalent at higher neutron energies. To circumvent this problem, Pelliccioni (Pelliccion, 1998) calculated conversion coefficients (blue diamond in the figure) for higher neutron energies using the technique suggested by ICRP and implemented in the FLUKA code (Roesler and Stevenson, 2006). The fitted curve AMB74 (red line) includes both the ICRP conversion coefficients and the coefficients extended by Pelliccioni. This study uses AMB74 for the calculation of dose equivalent from secondary neutrons. The term AMB74 in FLUKA represents the ambient dose equivalent conversion coefficients. According to ICRP, the ambient dose equivalent refers the dose equivalent which would be produced in the ICRU sphere (30 cm diameter) at a depth of 1 cm on the radius opposite to the direction of incident radiation (ICRP, 1990).

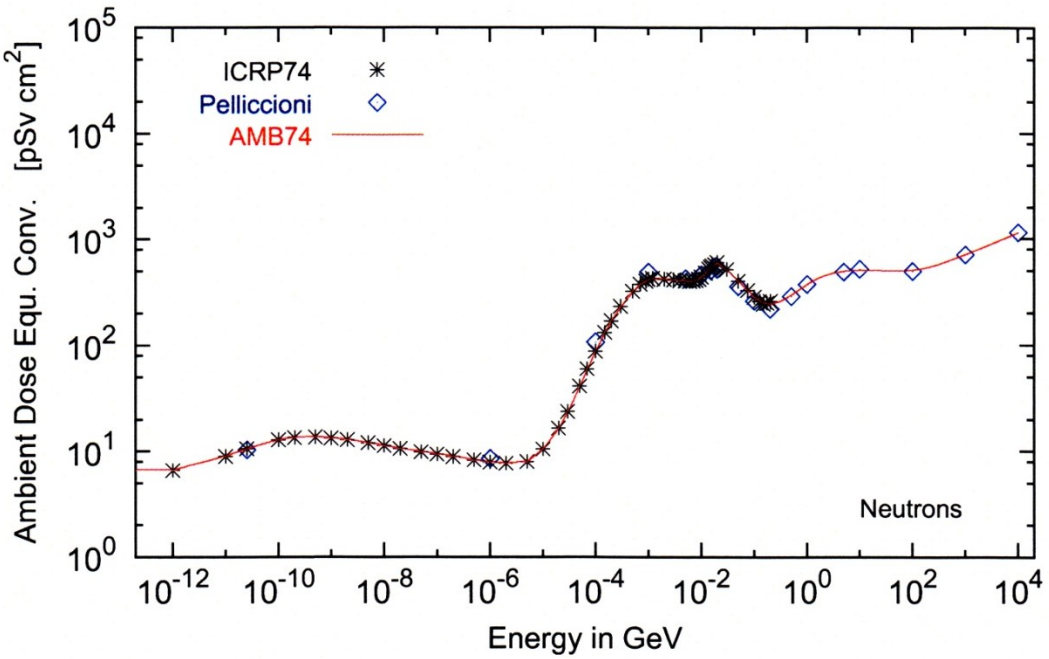

Figure 4.3: Ambient dose equivalent coefficients as a function of neutron energy. Plot taken from (Roesler and Stevenson, 2006).

The reason behind the use of ambient dose equivalent in this study is that the current release of FLUKA does not include any code to calculate neutron equivalent dose. For this reason, it is difficult to assess the difference between neutron equivalent dose and ambient dose equivalent. To solve this problem, a study was carried by Halg et. al. (Halg et al., 2011), where absorbed dose and ambient dose equivalent were scored for neutrons from 10^{-7} to 10^3 MeV using 13 monoenergetic beams in FLUKA. The absorbed dose and ambient dose equivalent due to neutrons were calculated in an ICRP tissue mass of dimension $1 \times 1 \times 0.5$ cm^3. For each neutron energy, the neutron equivalent dose was then calculated by multiplying the average absorbed dose with the neutron weight factor w_R, as shown in Equation (4.17), and a conversion coefficient from fluence to equivalent dose was established.

Using this process, the neutrons dose spectra created by protons inside a phantom were evaluated at 0, 5, 10, 15, 20, 25, and 30 cm depth. The ratio of neutron equivalent dose to ambient dose equivalent H*(10) is shown in Figure 4.4.

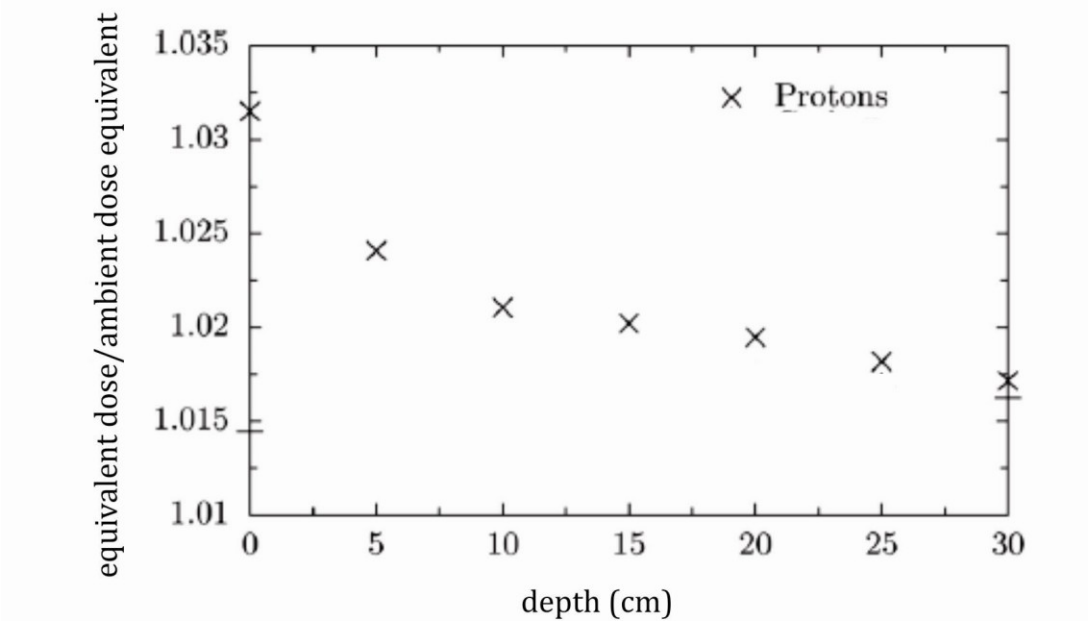

Figure 4.4: Ratio of neutron equivalent dose to ambient dose equivalent calculated for a proton beam. Data taken from (Halg et al., 2011).

As can be seen from this figure, the largest difference between the equivalent dose and ambient dose equivalent is less than 4%. Since the difference is much smaller than the uncertainty in the neutron dosimetry measurement themselves, the neutron dosimetry community considers neutron ambient dose equivalent as essentially identical to equivalent dose.

4.4 *Guidelines for secondary radiation exposure*

At present, there are no active regulations or guidelines for the radiation leakage in proton or heavy ion therapy facilities (Moyers et al., 2008). Currently, most radiotherapy facilities follow the recommendations of the American Association of Physicists in Medicine (AAPM) for electron and x-ray therapy. In addition, some states in the USA have their own state regulations for radiation therapy. In 2006, the International Electro-Technical Commission (IEC) recommended that the physical dose due to leakage of primary particles downstream of beam line not exceed 2% of prescribed dose (Moyers et al., 2008). However, no recommendation for secondary neutrons was mentioned. It should be noted that neutron energy and fluence strongly depends on the design of the beam delivery system. Because of this, neutron fluence spectra vary between different proton therapy centers. In addition, due to limited human data on neutron exposure, the complexity of radiobiological effects and their ultimate clinical effect is not yet understood. For these reasons, any recommendations on secondary neutrons exposure in proton radiotherapy could be inadequate. However, as neutrons possess higher RBE than protons of similar energy exposure to neutrons could cause secondary cancers in patients undergoing treatment using proton radiotherapy.

CHAPTER 5

DETECTOR, EXPERIMENT AND SIMULATION

In this study, both experiment and simulation approaches have been implemented to quantify off-axis neutron dose in proton radiotherapy. CR-39 plastic nuclear track detectors (PNTD) have been used to experimentally measure the neutron dose equivalent and Monte Carlo radiation transport Code FLUKA was used to simulate the experiment. CR-39 PNTD can measure the dose from charged particles of $LET_{\infty}H_2O \geq 5$ keV/μm and this allows for measurement of absorbed dose from secondary neutrons without measuring to absorbed dose from primary protons, since primary protons used in proton radiotherapy possess an $LET_{\infty}H_2O$ lower than 5 keV/μm.

5.1 *Detector*

This section describes different types of detector that are currently in use in proton radiotherapy for neutron detection. The rationale for using CR-39 PNTD is mentioned. The underlying principle behind the track formation in CR-39 PNTD and the importance of chemical etching procedure to enlarge the tracks is described. The

process of calibrating CR-39 PNTD to different ion/energy combinations is also mentioned.

5.1.1 Neutron detectors

Commonly used detectors in neutron dosimetry vary depending on the incident neutron energy. Historically, there are two widely used detectors in neutron dosimetry: Rem meters and Bonner spheres. Rem meters are more common in neutron detection in the area of health physics, while Bonner spheres are better suited as a laboratory instruments for the measurement of neutron energy spectra across a wide range of neutron energy.

The term Rem stands Roentgen Equivalent Men, an early unit of dose equivalent. A Rem meter uses a gas filled detector, either BF_3 or ^3He, which have high neutron cross sections to thermal and slow neutrons. A thick layer of polyethylene moderator surrounding the detector is used to slow down the neutrons. After being moderated in energy, the low energy neutrons reach the detector region and are captured by the gas nuclei of the detector.

Rem meter was originally developed in 1960s, where boron tri-fluoride (BF_3) was used as detector filling gas. This is commonly known as a Snoopy meter. A Snoopy meter is very useful for the detection of neutrons from fission sources, i.e. from 0.1 eV to 10 MeV. However, if the incident neutron energy is higher than 10 MeV, the

moderator is unable to thermalize these neutrons. This causes a significant decrease in neutron detection sensitivity. To accommodate higher energy neutrons, another type of Rem meter, known as the SWENDI Rem meter was designed in 1990s, where helium-3 (^{3}He) is used as detector filling gas and the polyethylene moderator is embedded within a tungsten powder shell. When neutrons of higher energy pass through the moderator, the combination of tungsten powder shell and polyethylene can thermalize the higher energy neutrons. This increases the sensitivity of the meter up to 5 GeV.

Another common type of neutron detector are Bonner spheres. Bonner spheres consist of polyethylene spheres of various diameters and ^{3}He, BF3, or Li-glass scintillator as detector. In this type of detector, the increasing thickness of the sphere increases the detector response to higher energy neutrons because greater moderator thickness is needed to thermalize higher energy neutrons. Unfolding the neutron energy spectra from Bonner sphere requires the response of a detector to various energies and a standard algorithm to produce an approximate spectrum. This process involves greater uncertainty in the approximated neutron spectra.

Although the use of a SWENDI detector is more common in proton radiotherapy than a Snoopy or a Bonner spheres, all these detectors possess the following limitations: a) they are bulky and cannot be placed inside a phantom for the measurement of organ equivalent dose, b) the sensitivity of these detectors varies depending on the incident neutron energy, c) and dose equivalent is measured from

fluence using fluence to dose equivalent conversion coefficients, adding greater uncertainty to the process. For these reasons, experimental measurement of neutron dose in proton radiotherapy remains a challenging problem and this forces the community to pursue numerical simulations.

An ideal, alternative detector in neutron dosimetry is CR-39 plastic nuclear track detector (PNTD). CR-39 plastic nuclear track detector (PNTD) is a transparent thermoset plastic polymer, polyallyldiglycol carbonate ($C_{12}H_{18}O_7$). In 1970s, P.B. Price (Cartwright et al., 1978) first introduced CR-39 PNTD for cosmic ray research and around the same time E.V. Benton (Cassou and Benton, 1978) first used it for radiation dosimetry. Since then, CR-39 PNTD has been the most common type of solid state nuclear track detector (SSNTD) used in radiation dosimetry. CR-39 PNTD is sensitive to the charged particles of $LET_{\infty}H_2O$ from 5 to 1500 keV/μm. As a result, CR-39 PNTD possesses a sensitivity to protons of energy $\leq$ 10 MeV, alpha particles of energy $\leq$200 MeV, and heavy ions ($Z \geq 3$) for all energies. Neutrons of energy between 1 and $\sim$ 20 MeV are detected from recoil proton tracks produced in elastic interactions between neutrons and hydrogen nuclei of the detector material. Neutrons of energy greater than 20 MeV are detected via tracks from recoil heavy ions (from C and O nuclei) in non-elastic target fragmentation interactions.

CR-39 PNTD is an ideal detector for neutron dosimetry in proton radiotherapy for the following reasons: a) CR-39 PNTD is made of a near-tissue equivalent polymer (composed of C, H, and O), i.e. it has tissue like sensitivity to the neutrons (Benton et

al., 1986), b) the threshold LET ($LET_{\infty}H_2O \geq 5$ ($LET_{\infty}H_2O \geq 5keV/\mu m$) to register tracks in the detector is higher than the LET of the primary protons of the beam, so that primary protons do not create tracks, and c) unlike other detectors, CR-39 PNTD is not bulky and can be placed at different locations inside a phantom to measure different organ doses.

This study uses CR-39 PNTD for the entire experiment. CR-39 PNTDs used in this study were manufactured by American Technical Plastics, Inc., Stratford, CT, where each sheet was about 600 micrometer thick and each detector was cut to 4 x 4 cm^2 to place inside the phantom or in air.

5.1.2 Formation of tracks in CR-39 PNTD

When a charged particle passes through the detector material, it delivers part of its kinetic energy to the atoms surrounding its path and causes ionization and excitation. This primary ionization causes a large number of chemical bonds of the plastic to break along the particle's trajectory. This path of chemically reactive broken bonds is called a latent damage trail. This latent damage trail is too small to observe by an optical microscope. For this reason, the detectors are etched in a highly reactive chemical solution (50^0C, 6.25 N NaOH for this work) for a set period of time to enlarge the tracks so that they are visible under an optical microscope. The chemical solution etches the detector at a rate higher along the latent damage trail than it etches the bulk of the plastic. The rate at which etching progresses along

the trail is called the track etch rate, $V_{T,}$ and the etching rate of the bulk of the plastic is called bulk etch rate, V_B. Figure 5.1 illustrates such a nuclear track as a result of the chemical etching process.

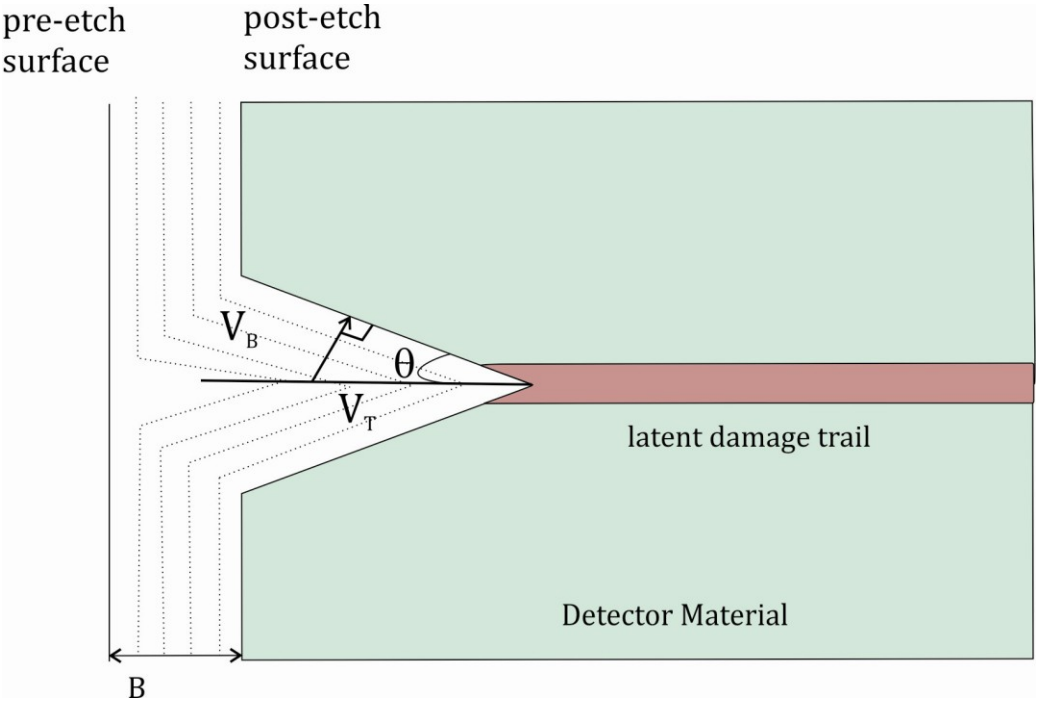

Figure 5.1 Nuclear track formation as a result of etching process (Henke and Benton, 1971).

Figure 5.1 shows a two dimensional view of the track etching process. The bulk etch rate V_B propagates in all directions except along the damage trail and this property results in a three dimensional conical pit referred to as a nuclear track. The area of the elliptical opening of each conical pit is proportional to the LET of the incident particle that formed the track. For a nuclear track to be formed, the ratio of track etch rate to bulk etch rate, also known as reduced etch rate ratio, V_r, needs to be greater than 1. Alternatively, the track etch rate, $V_{T,}$ needs to greater than bulk etch

rate, V_B. The reduced etch rate ratio, V_r, is an important parameter for the dimensions of the tracks since V_r is proportional to the LET of the charged particles that created the track. The reduced etch rate ratio, V_r, is (Henke and Benton, 1971):

$$V_r = \frac{V_T}{V_B}. \tag{5.1}$$

From Figure 5.1, the cone angle, θ, the angle between the wall of the track and the axis of the track, can be written in connection with the reduced track etch ratio as:

$$\sin\theta = \frac{1}{V_r} = \frac{V_B}{V_T}. \tag{5.2}$$

To determine V_r, the semi major axis and semi minor axis of the elliptical opening of the tracks need to be measured. The semi major and semi minor axes depend on the cone angle θ, the dip angle δ (the angles at which particle hits the detector surface, Figure 5.2), and the bulk etch B (the amount of material removed in the etching process). Geometrically these parameters are illustrated in Figure 5.2. The semi major axis, a, and semi minor axis, b, are related to the cone angle, θ, and dip angle, δ, as shown in Equations (5.3) and (5.4) (Henke and Benton, 1971):

$$a = \frac{B\cos\theta}{\sin\delta + \sin\theta}, \tag{5.3}$$

$$b = B\sqrt{\frac{\sin\delta - \sin\theta}{\sin\delta + \sin\theta}}. \tag{5.4}$$

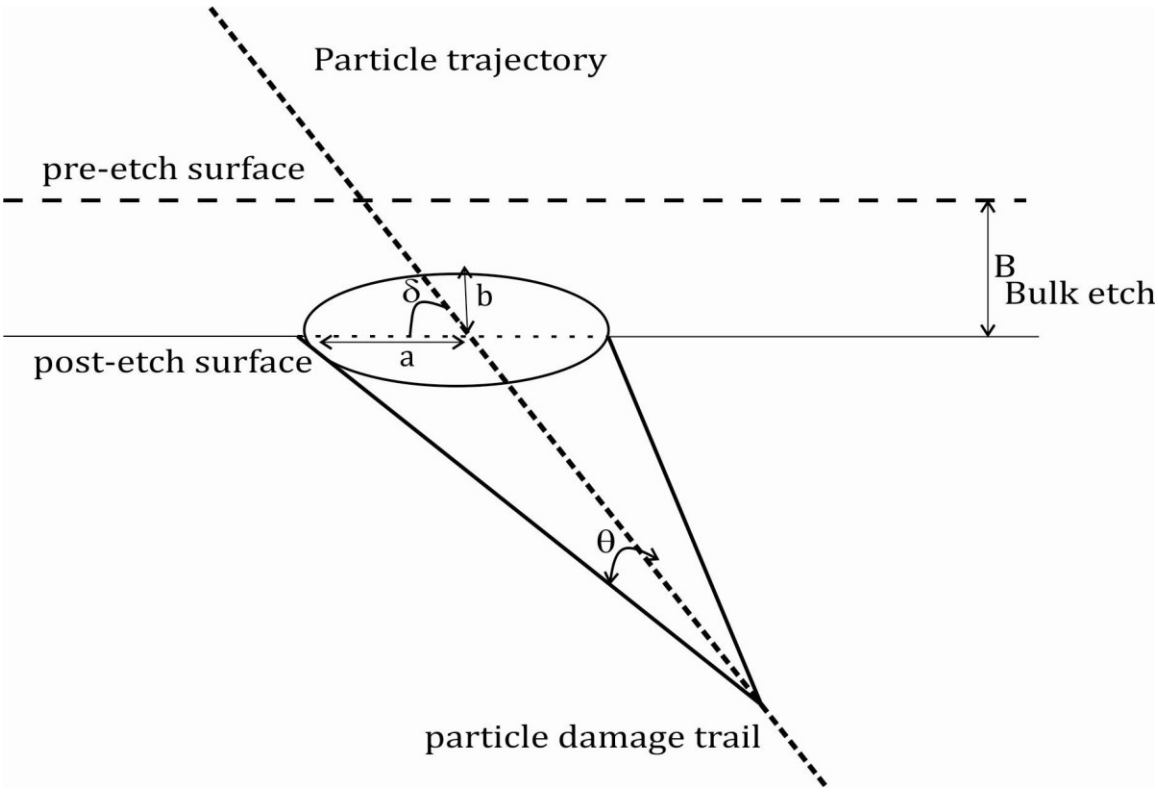

Figure 5.2: Etched nuclear track with several geometrical parameters (Henke and Benton, 1971).

Using Equations (5.3) and (5.4), the reduced etch ratio, V_r, can be found (Benton, 2004):

$$V_r = \sqrt{\frac{1 + 4\left(\frac{a}{B}\right)^2}{\left(1 - \left(\frac{b}{B}\right)^2\right)^2}} \,. \tag{5.5}$$

As mentioned above, V_r needs to be greater than 1 for track formation and this serves as an important condition for the determination of absorbed dose. The bulk etch, B, is determined from the difference in mass of the detector due to the etching process (Henke et al., 1986):

$$B = \frac{(m_1 - m_2)\bar{t}_2}{2m_2}\left(1 - \frac{P\bar{t}_2}{2A}\right), \qquad (5.6)$$

where m_1 and m_2 are the masses before and after etching, $\bar{t}_2$ is the mean post-etch thickness, P is the perimeter, and A is the one-sided surface area of the detector.

5.1.3 Importance of short-etch and long-etch methods

CR-39 PNTD is etched for a predetermined amount of time. For relatively accurate measurement of LET spectrum, use of both short-etch and long-etch methods are suggested. The usual duration of short-etch and long-etch in NaOH solution at 50^0C, 6.25 N is 36 hours and 168 hours, respectively, corresponding roughly to B values of 8 μm and 40 μm, respectively. This is because the shorter range particle that can be deleted by CR-39 PNTD is on the same order as the value of B. High LET short-range target fragments produced in nuclear interactions of highly energetic protons or neutrons with heavy nuclei of the detector material or the material near to it often have ranges < 40 μm. At the same time, some etching is required to make the track large enough to see with an optical microscope. A short etch of 8 μm serves as a compromise. In dosimetry of high energy neutons, fragments (most commonly C and O recoiled nuclei) contribute significantly to the LET (≥ 5 keV/μm) spectrum.

The standard long etch method typically removes about ~40 μm of surface material and, therefore, removes tracks that might be formed from these short range target fragments. This ultimately leads to an error in the determination of the LET

spectrum. In order to overcome this error in LET determination, a second detector with relatively short etch period is analyzed (Benton, 2004).

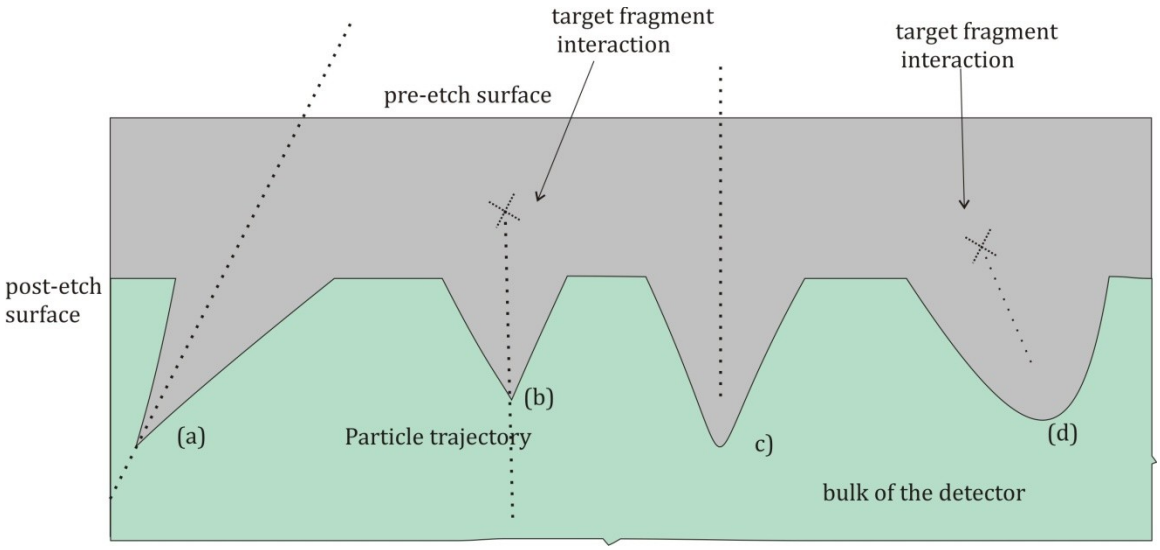

Figure 5.3: Cross sectional view of different types of track formed in PNTD (Benton, 2004).

Figure 5.3 illustrates several track formation patterns and the reasons why LET spectra measured from a short-etch detector needs to be combined with measurements from a long-etch detector. In this figure, case *a* represents the situation where the particle travels through both pre-etch and post-etch surfaces of the detector and forms a standard elliptical track with sharp conical tip. This kind of tracks provides relatively accurate LET information. Case *b* represents a target fragmentation event which occurs in the layer removed by chemical etching and stops in the volume of the detector. Such tracks have sharp conical tip, but since the particles do not pass through the pre-etch surface, the tracks formed in this situation are smaller than they would be if they were passed through the pre-etch

surface. As a consequence, the LET for case b is under measured. Case *c* shows a track where the particle passes though the pre-etch surface and stops with in the volume of the detector. As can be seen from the figure, the end of the track is not sharp but rounded instead. This is because the etchant in this case reached deeper than the stopping point of the particle in the detector. This type of tracks is referred to as an over-etched track and without special treat LET will be over measured. Case *d* represents a combination of cases *b* and *c,* where the tracks are small and over-etched. This case also leads to error in the LET measurement.

In order to minimize the number of improperly measured tracks (cases *b*, *c* and *d*) without impacting measurement of the good tracks (case *a*), a short etch detector is used in addition to a long etch detector. Since a long etch detector is effective for low LET (≤ 50 keV/μm), a combination of short-etch and long-etch method covers the LET range from 5 to 1500 keV/μm. In this study, two layers of detectors were exposed under identical conditions, one of them was processed with long duration etch and the other was processed with a short duration etch.

5.1.4 Response of CR-39 PNTD

The response function of CR-39 PNTD is required to generate LET spectrum and eventually dose and dose equivalent from the tracks measured in the detector. For this purpose, a particular batch of CR-39 PNTD from the same manufacturer was exposed to various ion/energy combinations at two particle accelerators: HIMAC in

Japan, and the NASA Space Radiation Laboratory at the Brookhaven National Laboratory (BNL), USA. The aim is to expose the detector to particles of known LET, then measure the reduced etch ratio, V_r, and finally to plot LET_{200}CR-39 versus V_r-1. A polynomial is then fit to determine LET as a function of the reduced etch rate ratio. This is because a fitted function to the plot of LET_{200}CR-39 against V_r-1 best represents the track size with the LET of the particle, where LET_{200}CR-39 represents the restricted energy loss from charged particles in CR-39 PNTD restricted to only the secondary electrons of energy ≤200 eV (Henshaw et al., 1981). The fitted polynomial for 168 hour etch is:

$$y = 2.11 + 1.045x + .06073x^2 - 0.1188x^3 - 0.02921x^4 , \quad (5.7)$$

and for 36 hour etch is:

$$y = 2.037 + 0.6963x + 0.09776x^2 - 0.3216x^3 , \quad (5.8)$$

where $x = \log(V_r - 1)$ and $y = \log(\text{LET}_{200}\text{CR-39})$. The conversion of LET_{200}CR-39 to $LET_{\infty}H_2O$ is done using the formula(Benton, 2004) :

$$\log(\text{LET}_{\infty}\text{H}_2\text{O}) = 0.1689 + 0.984 \log(\text{LET}_{200}\text{CR-39}). \quad (5.9)$$

This LET value represents the LET spectrum and later used for the calculation of dose and dose equivalent. A linear correction was also made to the LET spectra for the measured tracks. This is because the measured LET spectra showed protons LET at ~120 keV/μm, but that should be within ~95 keV/μm. The source of error in the LET spectra could be due to the temperature effect during the chemical etch.

5.2 *Experimental approach*

The purpose of this study was to measure the off-axis dose equivalent outside the treatment volume produced by secondary neutrons. For this purpose, four different experimental configurations were designed to study the secondary neutrons created by the beam shaping components and by the phantom material. According to the setup, the experiments were named as solid-phantom, in-air, hollow-phantom, and cylindrical-phantom configurations. In all four configurations, CR-39 PNTDs were placed in nearly identical locations from beam isocenter. In solid-phantom configuration, layers of CR-39 PNTDs were placed inside a solid phantom to simulate the dose equivalent that a patient would receive in different organs during actual treatment. The in-air configuration was designed to observe the neutrons dose equivalent in the absence of a phantom. The hollow-phantom configuration was created by placing a hole along the beam direction in the solid phantom to observe the dose equivalent pattern if the primary beam does not interact with phantom material. The cylindrical phantom-phantom configuration was designed to observe the dose equivalent if the primary beam interacts only along the beam path in the phantom material.

The dimension of each CR-39 PNTD detector used in the experiment was $4 \times 4 \times 0.05$ cm^3. A polyethylene phantom of 0.96 gm/cm^3 density was placed in front of the snout to represent a patient in solid-phantom configuration. The phantom was built by assembling polyethylene blocks, each having a dimension of

$20 \times 20 \times 5$ cm^3. Using these blocks, a phantom of 60 cm in length and 20 cm in width was created for the experiment. As shown in the figure (Figure 5.4, top), three columns of polyethylene blocks were assembled to construct the phantom along the beam direction, where the thickness of the phantom differed along the length. The thickness of the first and the third column was 35 cm, and the thickness of the second column was 52 cm to cover the 135° angled detectors.

Figure 5.4, and Figure 5.5 represents the schematic diagram of the setup and the actual photograph of the experiment for solid-phantom and in-air configuration, respectively. In solid-phantom configuration (Figure 5.4), detectors were placed inside a solid phantom and located at 7.5 cm, 17.5 cm, 28 cm, and 35 cm from the beam isocenter at 45°, 90°, and 135° from the primary beam axis. In in-air configuration (Figure 5.5), no phantom was present and detectors were placed in the air at locations identical to those inside the solid-phantom configuration except at 90° where detectors were placed at larger distances from isocenter (40 cm and 50 cm). Twelve set of CR-39 PNTDs were used for each experimental configuration. The dotted circles, in Figure 5.4, represent the detectors location inside the phantom but detector is not visible in the actual photograph. The filled circles and white rectangular objects illustrated in Figure 5.5, shows the detector location for in-air configuration.

solid-phantom

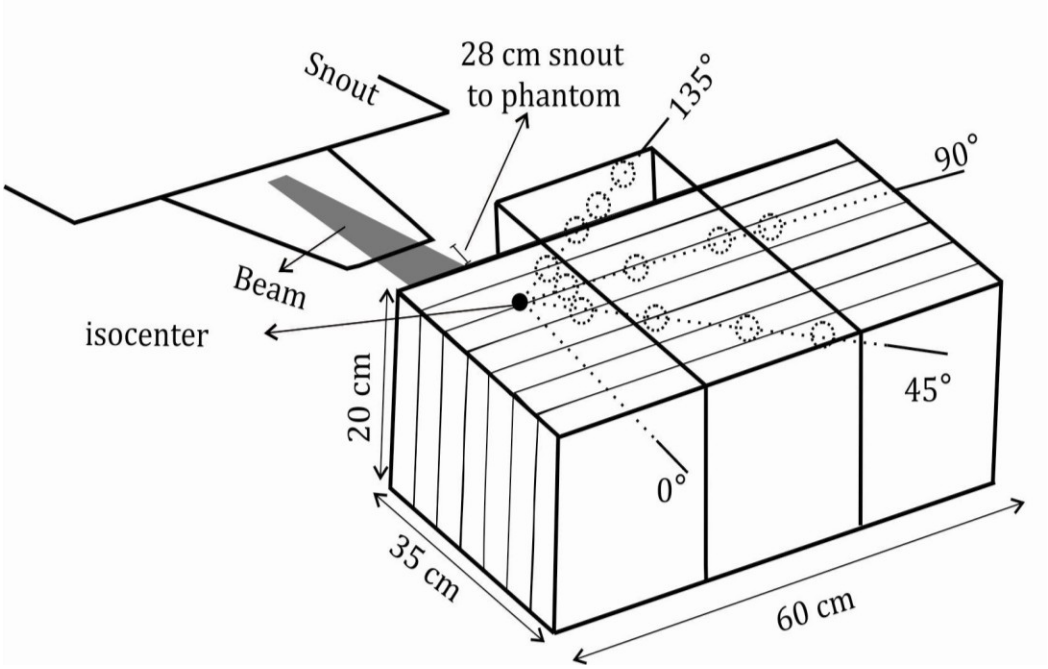

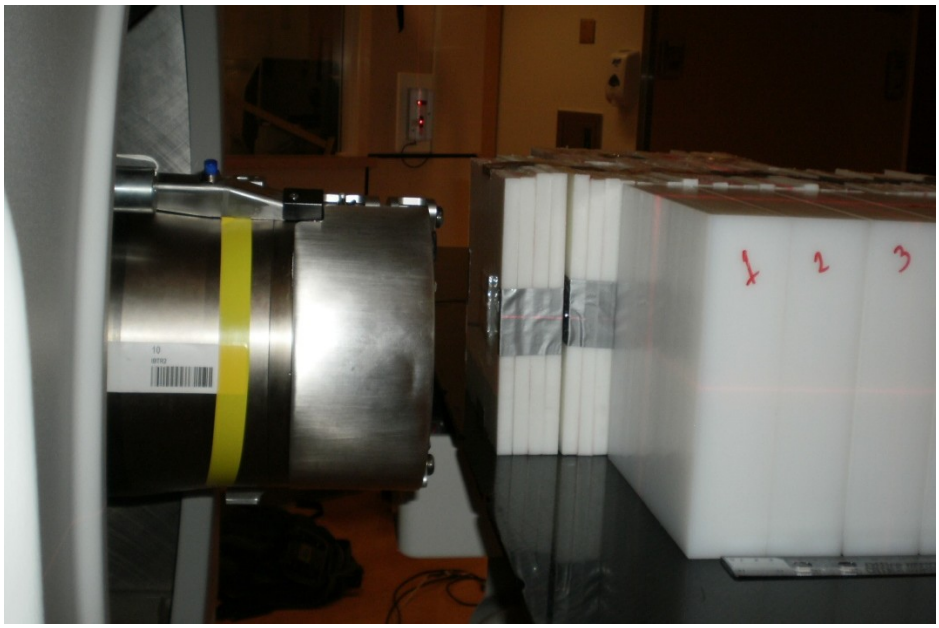

Figure 5.4: (top) Diagram of the solid-phantom experimental setup. Dotted circles represent the detectors locations inside the phantom (top). Picture was taken during the actual experiment (bottom).

in-air

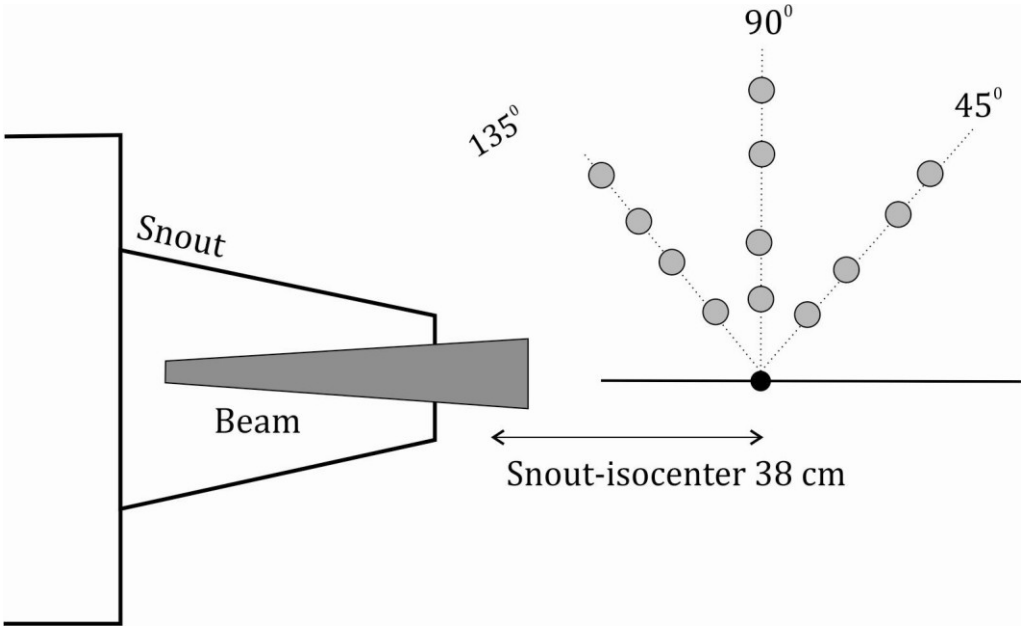

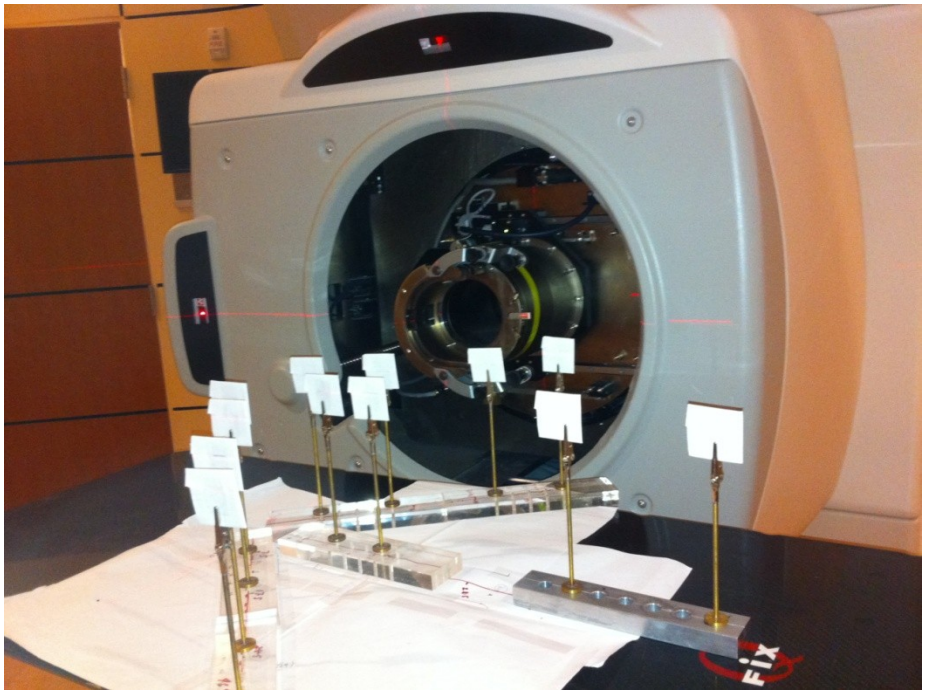

Figure 5.5: Diagram of the in-air experimental setup. Circles represent the detectors locations in the air. Picture was taken during the actual experiment (bottom).

The schematic diagram of the setup and the actual photograph of the experiments for hollow-phantom and cylindrical-phantom are shown in Figure 5.6 and Figure 5.7, respectively. The dotted circles, in Figure 5.6 , represent the detectors location inside the phantom but detector is not visible in the actual photograph. The filled circles and white rectangular object (in the photograph), in Figure 5.7, shows the detector location at cylindrical-phantom configuration. The photograph of the cylindrical-phantom configuration is also shown Figure 5.7.

In hollow-phantom configuration (Figure 5.6), the dimension and the density of the phantom material was same as was in solid-phantom configuration, except that a 5.5 cm diameter hole was bored along the center of the first column of polyethylene blocks of the phantom. The hollow part of the phantom was placed along the direction of the primary proton beam. Detectors were placed inside the phantom at 7.5 cm, 17.5 cm, 28.5 cm, 35.5 cm for 45°, and 90°, but at 135° three detectors were used at 7.5 cm, 17.5 cm, 35.5 cm from beam isocenter. A total of eleven set of detectors were used in each experimental configuration. In cylindrical-phantom configuration (Figure 5.7), a cylinder (same phantom material) of 5.5 cm diameter and 35 cm length was placed along the beam direction. The detectors location from beam isocenter was identical to those inside the hollow-phantom configuration except at 90° where the largest distance of the detector was 40 cm from isocenter.

hollow-phantom

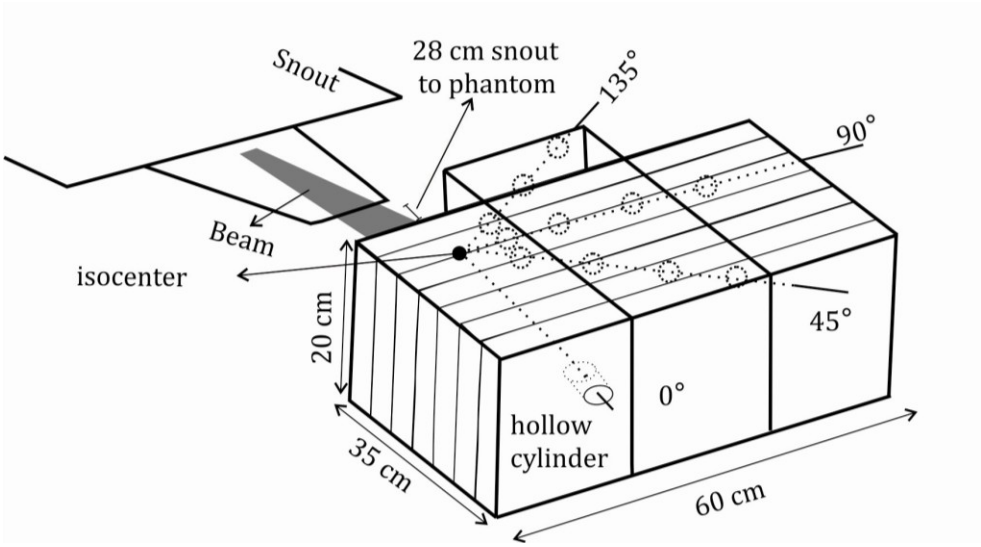

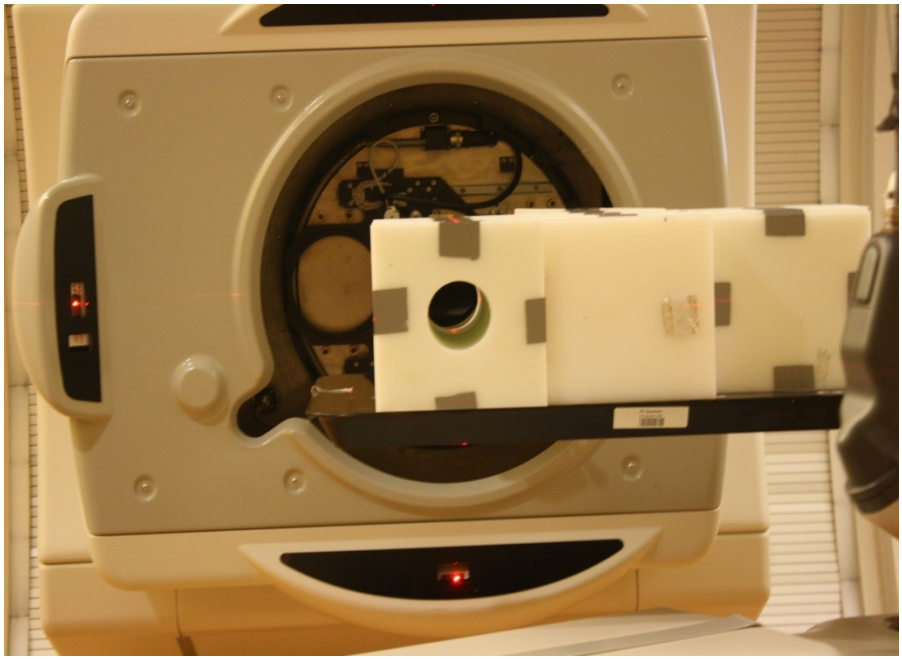

Figure 5.6: Diagram of the hollow-phantom experimental setup where dotted circles represent the detectors locations inside the hollow phantom (top), picture taken during the actual experiment (bottom).

cylindrical-phantom

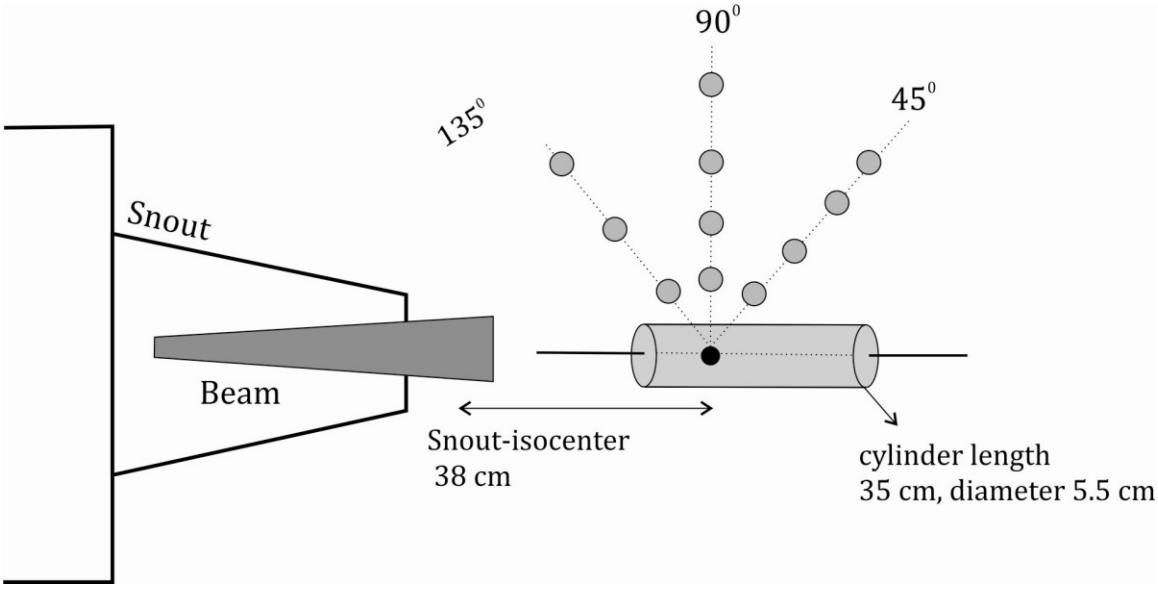

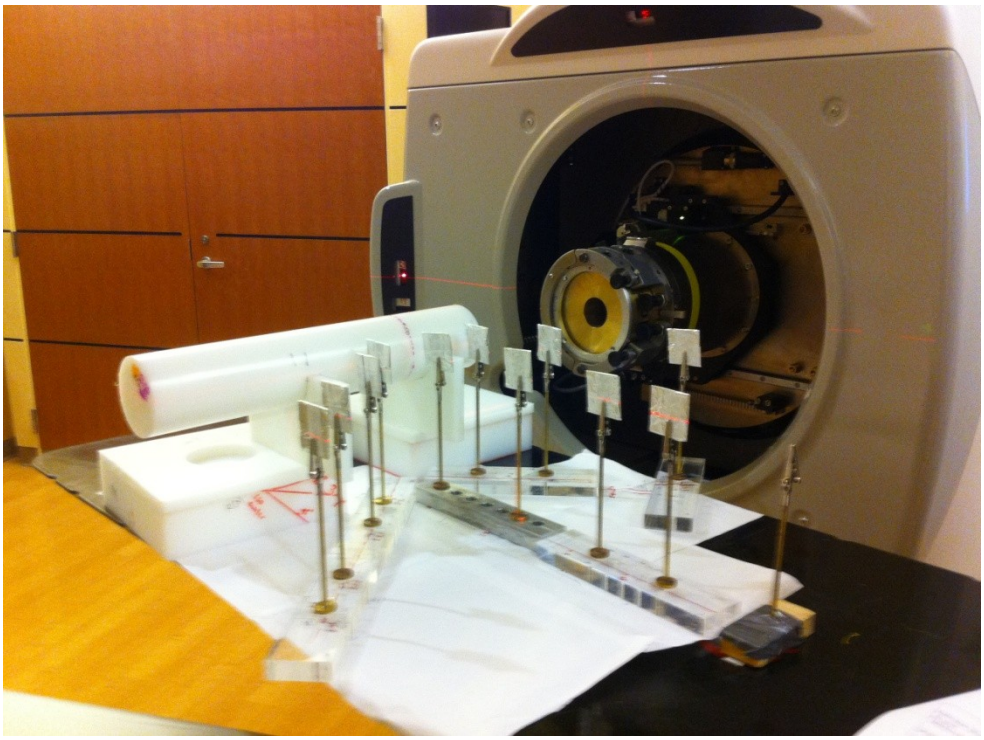

Figure 5.7: Diagram of the cylindrical-phantom experimental setup where filled circles represent the detectors locations (top), picture taken during the actual experiment (bottom).

Three proton beams of 78 MeV, 162 MeV, and 226 MeV were used for all the experimental configurations. A common set of treatment parameters was used: a 4 cm spread out Bragg peak (SOBP), a 5 cm diameter patient brass aperture, a 10 cm from surface to isocenter, a 28 cm distance from snout to surface of the phantom, a 18 x 18 cm^2 uncollimated beam, and no range compensator. These treatment parameters will treat a patient of imaginary tumor of 5 cm diameter and 4 cm width. The air distance was chosen 28 cm to replicate commonly used value (20-30 cm) in proton radiotherapy. It is to be noted that air distance is patient dependent. For example, in ocular cases or in head and neck, air distance is carefully chosen to improve the dose fall-off pattern at the distal end of the target in order to avoid the dose in critical structure. The isocenter inside the phantom was chosen 10 cm to replicate more common practical scenario. No compensator was used in this experiment because no dose conformation was required around the contour of the treatment volume. Also, range compensator is usually made of plastic and it does not contribute significant secondary neutrons off-axis to treatment volume.

5.3 *Simulation*

This section describes the basic approach used in Monte Carlo radiation transport codes employ for modeling a simple experiment. An introduction is given on the radiation transport code FLUKA. The simulation of a simplified snout for uniform scanning proton beam is described. The interaction of the proton beam with

different components of snout and the production of secondary particles and their propagation is also shown graphically.

5.3.1 The Monte Carlo radiation transport code FLUKA

The term Monte Carlo refers to the use of a repeated random sampling technique for the simulation of a physical event. The probable behavior of a physical event can be simulated from the outcome of a large number of trials of that system, where each of the trials is simulated by a computer and based on a sequence of random numbers. By using random numbers, this method simulates a physical problem via z probabilistic approach and is sometimes called a virtual experiment.

In simulations of secondary neutron production in the ProCure beam delivery system, the physical behavior of the problem is predicted by the interaction of proton beam as it passes through the complex mass distribution represented by the beam delivery system and a phantom patient. Individual primary proton's interaction with the geometrical mass distribution at each point along proton's trajectory is determined via the probability of the many different interactions processes (cross sections). The outcome of the interaction at each point is determined based on weighted random numbers. This process also includes the probability of the generation of secondary particles and the probability of interactions of these secondary particles with the mass. This process continues until all the particles produced as a result of the incident primary proton either stop or

leave the volume of interest. The calculation progresses repeatedly due to a large number of primary protons so as to obtain convergence on an average with good statistics. Finally, different parameters, e.g., LET, dose, or dose equivalent are scored by adding up the outcomes at a particular location of interest within the volume.

This study uses the Monte Carlo radiation transport code FLUKA for the simulation of the experiment. FLUKA is an integrated Monte Carlo radiation transport code that is widely used in many areas of physics and engineering including high energy experimental physics, cosmic ray research, medical physics, shielding design for radiotherapy vaults, radiation detector design, etc. (Andersen et al., 2004, Aiginger et al., 2005, Ballarini et al., 2007, Battistoni et al., 2007, Fassò et al., 2005). FLUKA was primarily developed to model the secondary radiation environment produced by particle accelerators at the European Organization for Nuclear Research (CERN). Later, the code was adapted for use in medical physics for the calculation of dosimetric quantities including LET, dose, and dose equivalent. The interaction of sixty different particles and their propagation inside the matter can be simulated using FLUKA. Electrons and photons from 1 keV to thousands of TeV, neutrons down to thermal energy, hadrons of up to 20 TeV, and all the corresponding anti particles can be tracked down with excellent accuracy.

FLUKA consists of three main components: a) geometry, b) physics, and c) scoring. In the beginning, the geometry of the problem is described in terms of combinatorial geometry. In this process, basic bodies like cylinders, spheres, parallelepipeds, etc.

are combined using Boolean operations (addition, subtraction, union, etc.) to describe complex 3D mass distribution of the problem. The material properties are then assigned to each object. After the geometry of the problem is fully described, an additional region called the “black hole” must be defined surrounding the region of interest. The purpose of the “black hole” is to halt the simulation of particles that leave the region of interest.

The physics component sets the appropriate cross sections such as those for inelastic nuclear interactions, and elastic scattering, and nucleus-nucleus interactions for a particle to propagate through the matter (FLUKA, 2013). FLUKA can also transport particles based on the energy of those particles. This enhances the efficiency since user can decide to propagate only particles within a given energy range and ignore particles with energy below this range. This capacity can effectively reduce the computation time. The transport of all particles except neutrons can be enabled for energies as low as 1 keV. Neutrons can be transported to even lower energies, i.e. 10^{-5} eV. The cross sections for neutron interactions is divided into 260 energy groups (Ferrari et al., 1997) with the lowest energy being 10^{-5} eV. The secondary electron production threshold (minimum energy required to produce a secondary electron) can be as low as 1 keV for all particles except neutrons.

The scoring component determines the quantity of interest in the region of interest. Since FLUKA estimates quantities using probabilistic approach, the scored quantity

always possess an uncertainty. The greater the number of primary particles in the simulation, the better is the statistical uncertainty. FLUKA can score a large number of quantities including particle fluence, dose, dose equivalent, beam current, LET, track length, energy spectra, Z spectra, and energy deposition.

In this work, the transport and secondary electron production thresholds were both set to 100 keV for all particles except neutrons. This means that all particles except neutrons with energy equal to or greater than 100 keV were transported. The transport and threshold value could be decreased to 1 keV, but such a low energy threshold would significantly increase the computation time. To score dose equivalent, a separate routine was used for neutrons of energy 1 to 20 MeV, because the interaction cross section for water decreases significantly for neutrons with energy greater than 20 MeV. In all the locations, dose equivalent was calculated with a statistical uncertainty equal to or less than 10%.

5.3.2 Simulation of simplified snout

In the simulation, a simplified snout, currently in use at ProCure Proton Therapy Center, Oklahoma City, OK, was modeled. The simplified snout consists of a snout base (brass), a snout wall (stainless steel), and a patient specific aperture (brass). Cross sectional and FLUKA geometry diagrams of the snout geometry are shown in Figure 5.8.

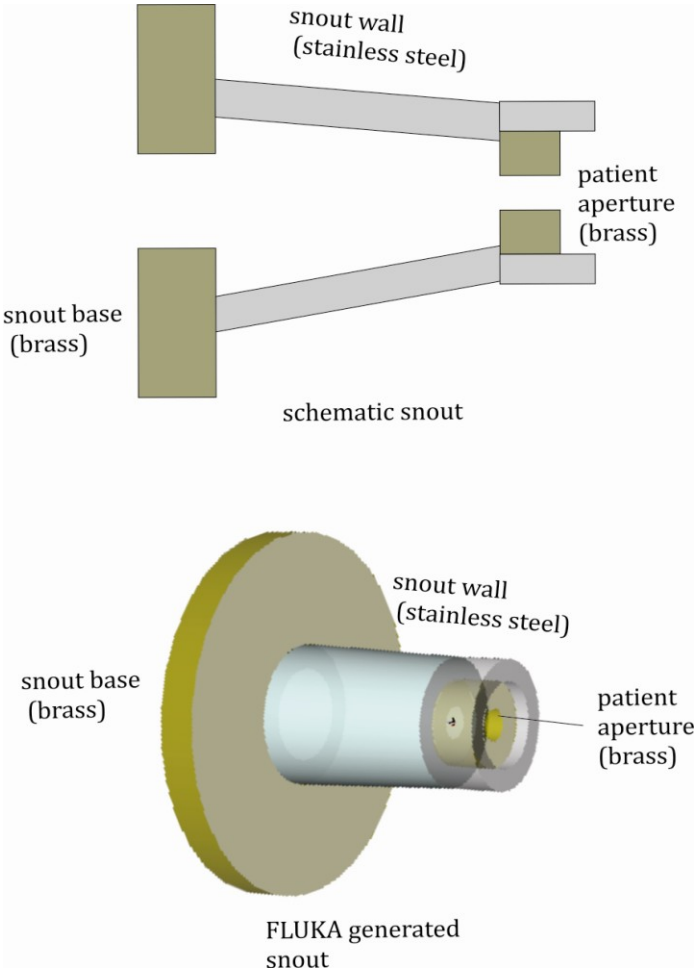

Figure 5.8: The cross sectional diagram of the snout (top), FLUKA geometry generated diagram of the snout (bottom). The snout is used at ProCure Proton Treatment Center, Oklahoma City, OK (Figure not drawn to scale).

The choice of simplified snout was made based on the fact that it contains the major neutron producing components of the beam delivery system. Neutron production in the range modulator and range compensator were not considered since they are composed of mostly low-Z material and the production of neutron in low-Z material was not considered to be significant. Among different components, by far the largest contribution from secondary neutrons to the patient comes from the patient aperture. The patient aperture is composed of brass and placed close to the patient.

For this reason, about 80% to 90% of the total secondary neutrons that may reach the patient come from the patient aperture. This is why the simulation of the simplified snout is adequate for the study of secondary neutrons and their respective contribution to the total dose equivalent.

The simulation was carried for identical treatment parameters and beam energies as described in the experimental section. Water was chosen as the material of the detector because, like water, CR-39 PNTD has a tissue-like sensitivity to neutrons. The dimension of the detector, placement of detector, dimensions of the phantom, phantom material, exactly mimics the same experimental design. All four experimental configurations were simulated.

5.3.3 Beam interaction with snout and phantom

As described in the experiment, an uncollimated beam of 18 × 18 cm^2 was used in the simulation. The beam of 18 × 18 cm^2 cross sectional area was created by defining appropriate divergence of the beam. According to beam commissioning report for the ProCure Proton Therapy Center, Oklahoma City, Ok (Zheng et al., 2011), a 18 × 18 cm^2 beam in front of the patient aperture is equivalent to a point source of protons that uniformly diverge to a 20 × 20 cm^2 area after travelling through 2 m in air. This beam was then allowed to propagate through the snout, where the patient aperture shapes the unmodulated field down to 5 cm diameter, after which it passed into the phantom.

The interaction of the beam with the snout and the phantom in 3D is shown in Figure 5.9. This plot illustrates how the proton point source diverges for the purpose of creating an 18 × 18 cm^2 unmodulated field in front of the aperture. As a result of interaction of the beam with the snout, secondaries (blue lines) are produced and scatter in all directions. This plot was created for a very low number of primary protons (10^3) for 162 MeV proton beam. However, for the determination of the dose equivalent at each location, about ~10^8 primary protons were transported. A 2D view of the beam interaction with the snout and phantom is shown in Figure 5.10.

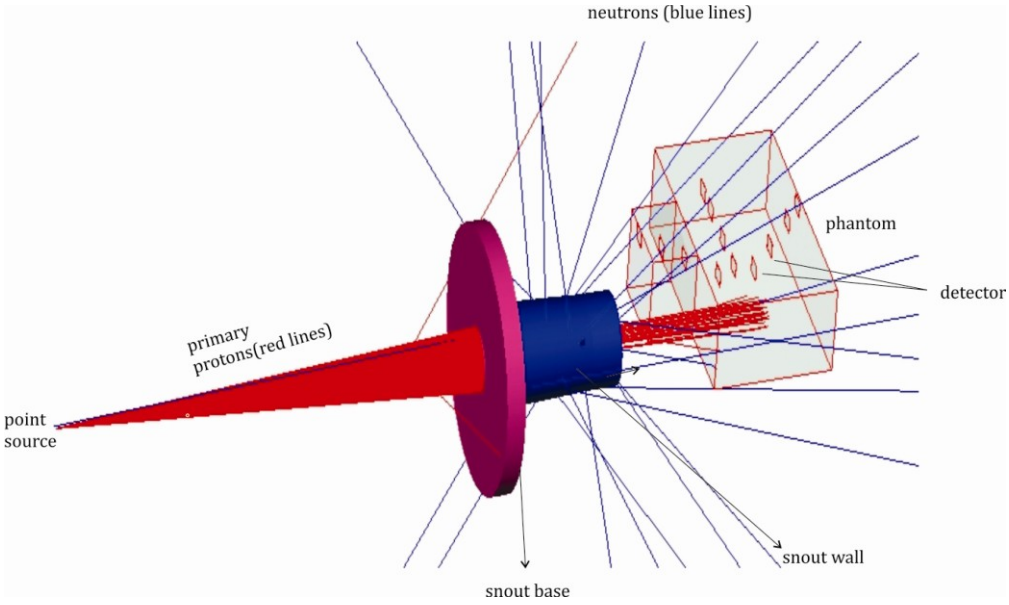

Figure 5.9: FLUKA simulated 3D view of a 162 MeV proton beam interacting with the snout and phantom.

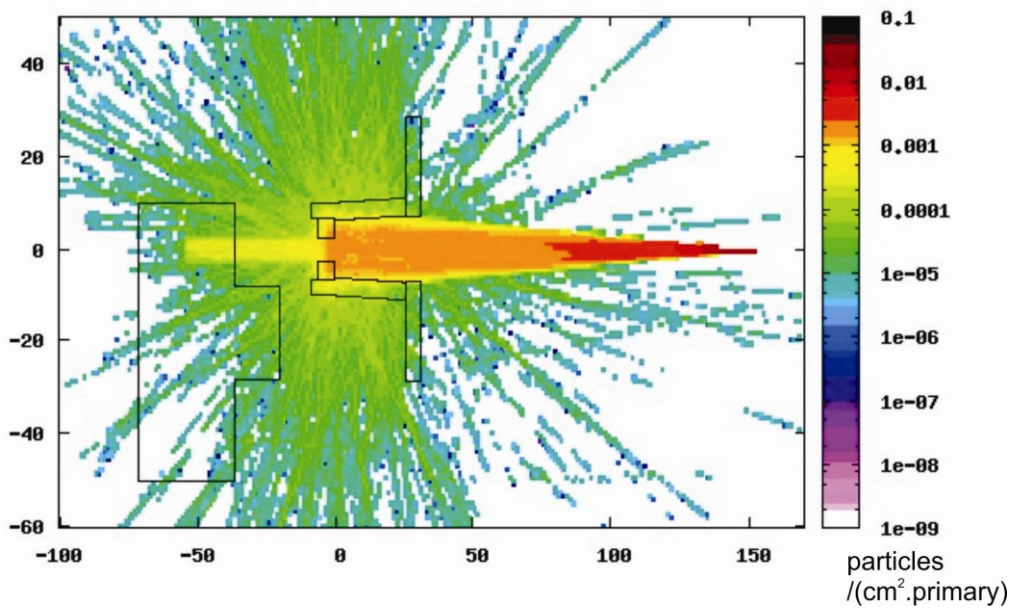

Figure 5.10: FLUKA simulated 2D view of 162 MeV primary beam interaction with snout and the phantom.

CHAPTER 6

EXPERIMENT AND SIMULATION METHODS

This chapter presents the readout method of the CR-39 PNTDs used in this study. An example of LET spectrum, dose spectrum and dose equivalent spectrum are plotted using the data obtained from the CR-39 PNTDs. The method of determining SOBP in the FLUKA simulations is described. Simulated SOBP for three different beam energies- 78 MeV, 162 MeV, and 162 MeV-is also shown.

6.1 *Analysis of CR-39 PNTDs*

This section describes the read-out method of CR-39 PNTDs. The instrument used to analyze the CR-39 PNTD and the method to determine the LET, dose and dose equivalent spectra are described. Examples of LET, dose and dose equivalent spectra from both short-etch and a long-etch detectors are shown.

6.1.1 CR-39 PNTDs read-out process

After the chemical etch, CR-39 PNTDs were analyzed using standard optical microscope. The readout process consists of locating all the tracks within a given

area on the surface of the etched detector and measuring the semi major axis, *a*, and a semi minor axis, *b,* of each individual track. A photomicrograph illustrating the tracks formed on the surface of CR-39 PNTD is shown in Figure 6.1, where the semi major and semi minor axis is visible in the inset picture.

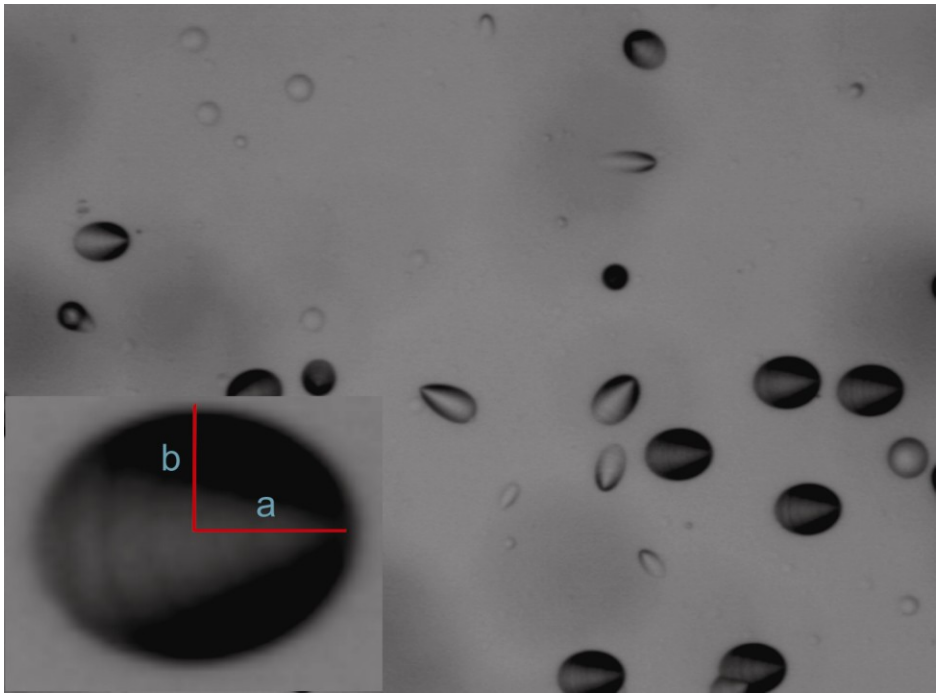

Figure 6.1: A photomicrograph of the tracks formed on a sample CR-39 PNTD detector. The inset shows the semi-major, *a*, and semi-minor, *b*, axes labeled on a nuclear track. The field-of-view has dimensions of 682 × 524 μm. Each nuclear track is ~16 μm in diameter.

PNTD analysis used a Samaica nuclear track detector system manufactured by ELBEK GmbH, Siegen, Germany (Trakowski et al., 1984, Dreute et al., 1986, Wiegel et al., 1986, Noll et al., 1988, Rusch et al., 1991). The ELBEK computerized microscope system consists of a light illuminated optical microscope, a CCD camera, a computer controlled x-y stage, an autofocus system, a video frame grabber and a PC, as shown in Figure 6.2. Customized software is used for the detection and

analysis of the photomicrograph image. In the readout process, a PNTD is first placed on the x-y microscope stage and then the computer calibrates the stage to a predefined set of coordinates. A particular objective is chosen for the scanning of the tracks. After calibration, the customized software is used to capture the image and to fit the circular and elliptical tracks of that image. The result of the fitting parameters such as semi major, semi minor axis, dip angle is saved as a text file for further processing.

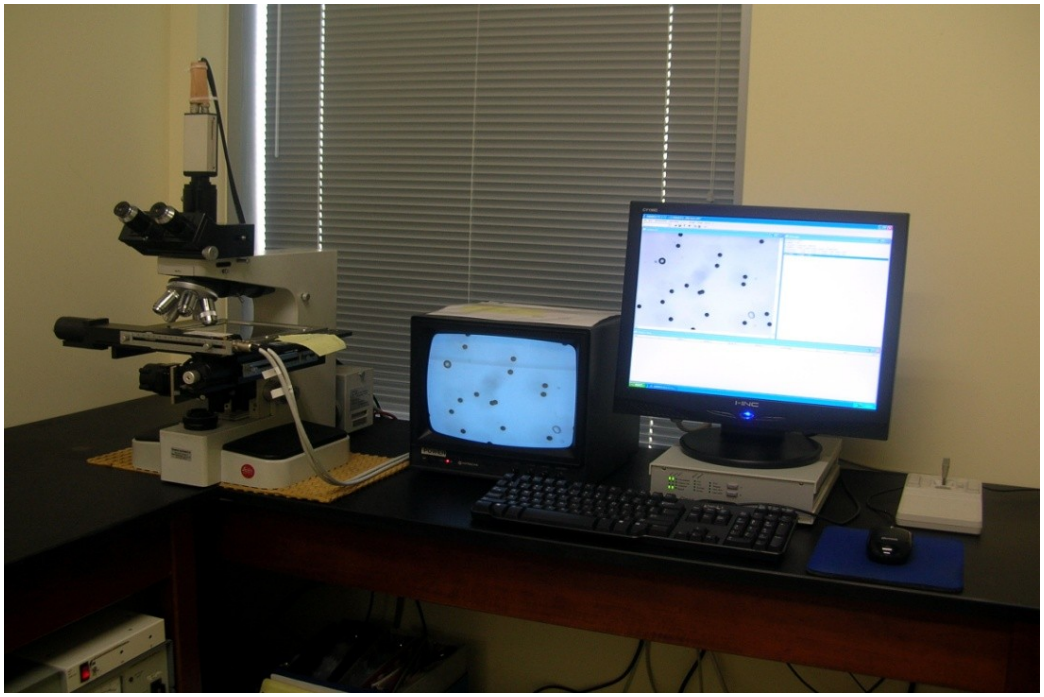

Figure 6.2: Photograph of Track detector analysis system used to read-out CR-39 PNTDs (Dewitt, 2011).

This text file is further processed using a MATLAB program developed for this experiment. This program generates LET spectrum, dose and dose equivalent from the track data contained in the text file. This processing involves, a) the

determination of reduced etched ratio, V_R , from the semi-major, a, and semi-minor, b, axes using Equation (5.5), b) calculation of $\mathrm{LET}_{\mathbf{200}}$CR-39 from detector response function shown in Equation (5.7) or (5.8), c) conversion of $\mathrm{LET}_{\mathbf{200}}$CR-39 to $\mathrm{LET}_{\infty}\mathrm{H_2O}$ using Equation (5.9).

A generated differential fluence LET spectra for a 162 MeV proton beam inside the phantom at solid-phantom configuration at 35.5 cm from isocenter and 90° to primary beam is shown in Figure 6.3. The data is shown for both long-etch (blue line) and short-etch (red line) detector. Since long-etch detectors cannot register short range tracks of relatively higher LET, a cross over point in the range from 30 to 100 keV/μm is usually chosen to combine the two LET spectra into a single spectrum. The combined LET spectrum as shown in Figure 6.4 is used for measuring the dose and dose equivalent. The integral fluence is then generated from this combined LET spectrum as shown in Figure 6.5. The integral plot starts adding the contribution of higher LET first and then continues adding up till the lowest LET value. The variable slope of the plot indicates the contributions of various LETs to the total spectrum. The relatively steep slope in the region, 20 to 50 keV/μm, illustrates the greater contribution of these LETs to the integral spectrum, whereas the leveling off of the spectrum below 10 keV/μm indicates that the LET below 10 keV/μm does not contribute much to the total fluence.

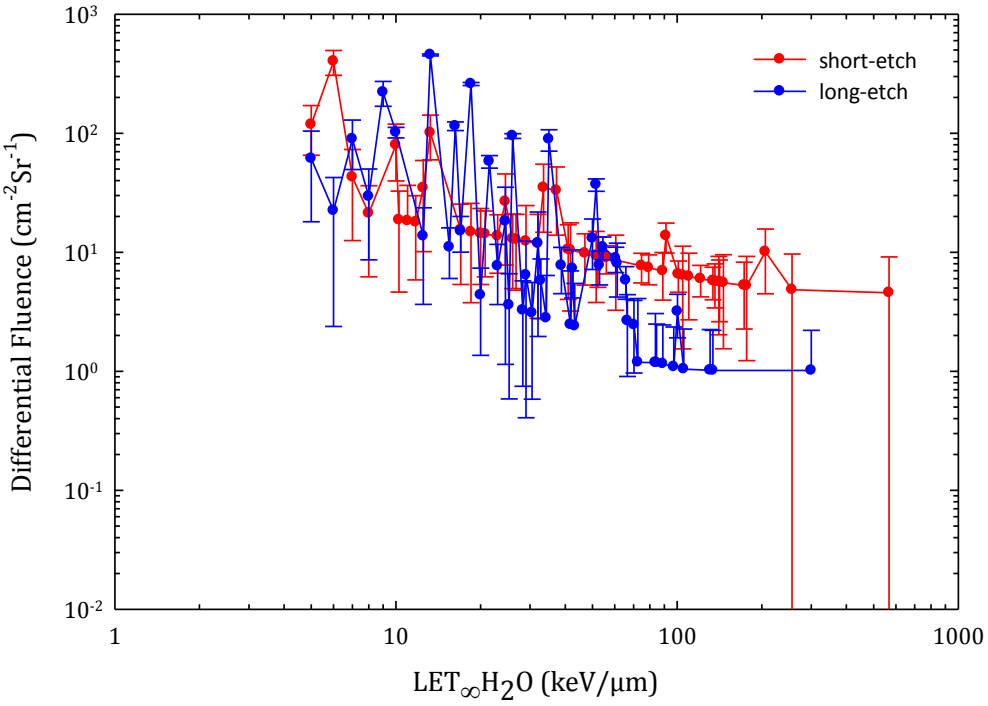

Figure 6.3: Differential LET fluence spectrum for 162 MeV proton beam for solid-phantom configuration at 35.5 cm from isocenter and 90° to the primary proton beam.

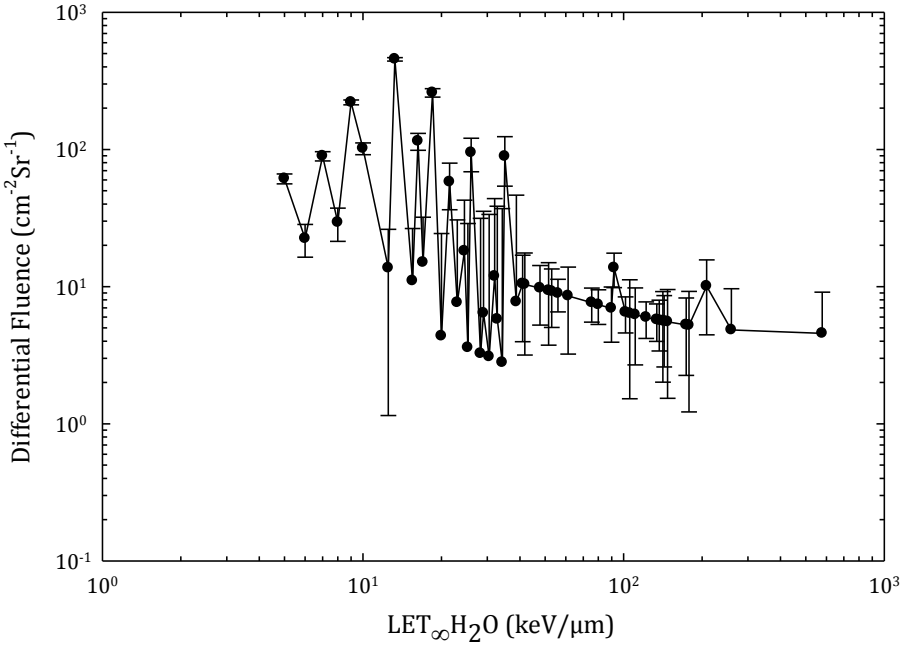

Figure 6.4: Combined LET differential fluence spectrum of long-etch and short-etch detector of 162 MeV proton beam for solid-phantom configuration at 35.5 cm from isocenter and 90° to the primary proton beam.

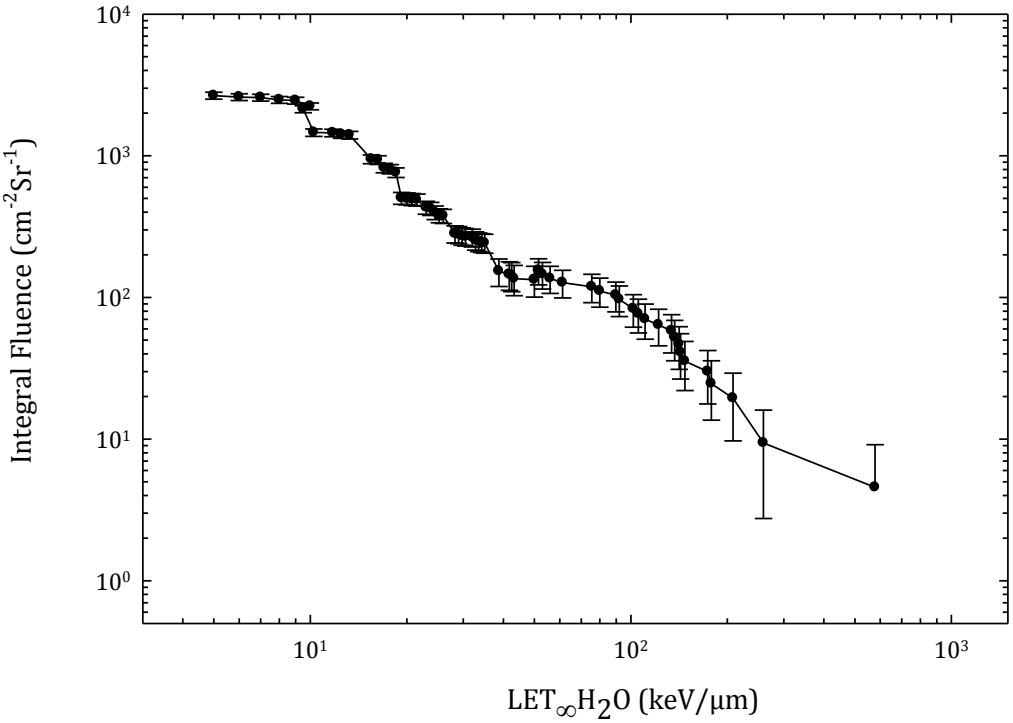

Figure 6.5: Integral LET fluence spectrum combining long-etch and short-etch detector of 162 MeV proton beam inside the solid phantom at 35.5 cm from isocenter and 90° to the primary proton beam

An integral LET dose and dose equivalent plot is shown in Figure 6.6 and Figure 6.7 respectively. The plots of dose and dose equivalent show that although the higher LET (>100 keV/μm) tracks are less abundant, their contribution to the total dose and dose equivalent is significant. The near flat slope <70 keV/μm in the integral dose equivalent plot shows that the total dose equivalent does not change much for the LET less than 70 keV/μm. The dose or dose equivalent at the lowest LET in the integral plots indicate the total contribution of the quantity of interest. This procedure was used for determining the total dose (Equation 4.15) and dose equivalent (Equation 4.16) at each detector location.

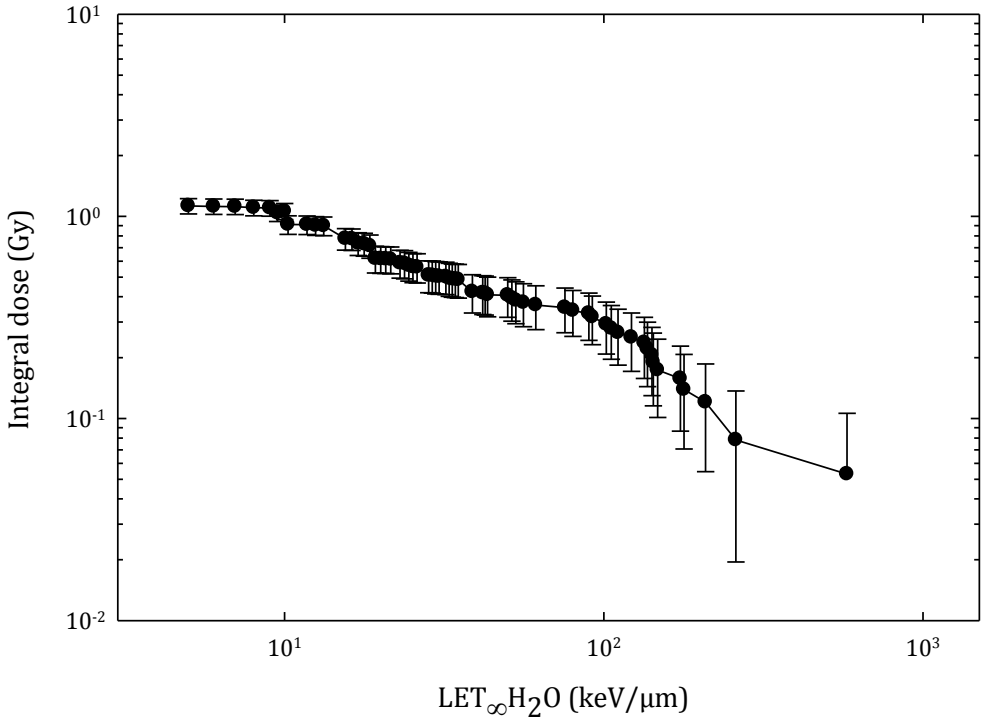

Figure 6.6: Integral LET dose spectrum combining long-etch and short-etch detector of 162 MeV proton beam inside the solid phantom at 35.5 cm from isocenter and 90° to the primary proton beam

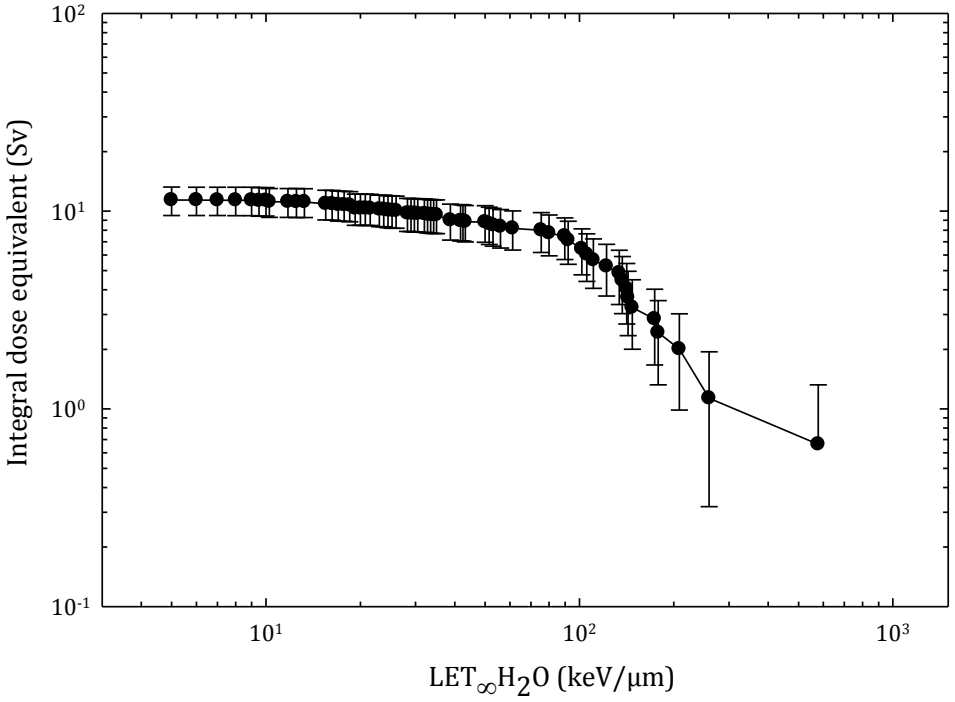

Figure 6.7: Integral LET dose spectrum combining long-etch and short-etch detector of 162 MeV proton beam inside the solid phantom at 35.5 cm from isocenter and 90 degree to the primary proton beam

6.2 *Simulation of SOBP*

This section describes the method that is used to simulate SOBP using FLUKA. In addition, the method to determine dose equivalent is also described. Calculated SOBP for all three beams used in this study is shown.

6.2.1 Calculation of SOBP

For the simulation of the SOBP, the effect of each layer of the range modulator was simulated by running an individual primary beam of a specific energy. A weighting factor, $w_{i,}$ was assigned for each layer and the dose for the SOBP was calculated by performing a weighted sum:

$$D/p = \sum_{i} w_i \, (D/p)_{i.} \qquad 6.1$$

The subscript, *i,* represents the number of the beam used in the process to produce the SOBP. The distal peak (highest energy) carries the highest weight and the proximal peak (lowest energy) carries the lowest weight.

A calculation of a 4 cm SOBP for the 226 MeV proton beam is explained in this section. The first step was to determine the distal and proximal edge of the desired SOBP. For a 226 MeV proton beam, the distal edge is 32 cm in water. To cover a 4 cm SOBP depth, the proximal edge needs to be at 28 cm, corresponding to a 208.5

MeV proton beam. Two more energies, 219 MeV and 213 MeV were used in between the distal and proximal edge for the overall uniformity of dose. Each beam was then run for the individual Bragg-peak. The dose at each Bragg-peak was then used to produce the SOBP by doing a weighted sum following Equation 6.1. The Bragg-peak of each individual beam and the weighted SOBP for 226 MeV protons is shown in Figure 6.8. The generated SOBP of 78 MeV, 162 MeV, and 226 MeV proton beam is shown in Figure 6.9.

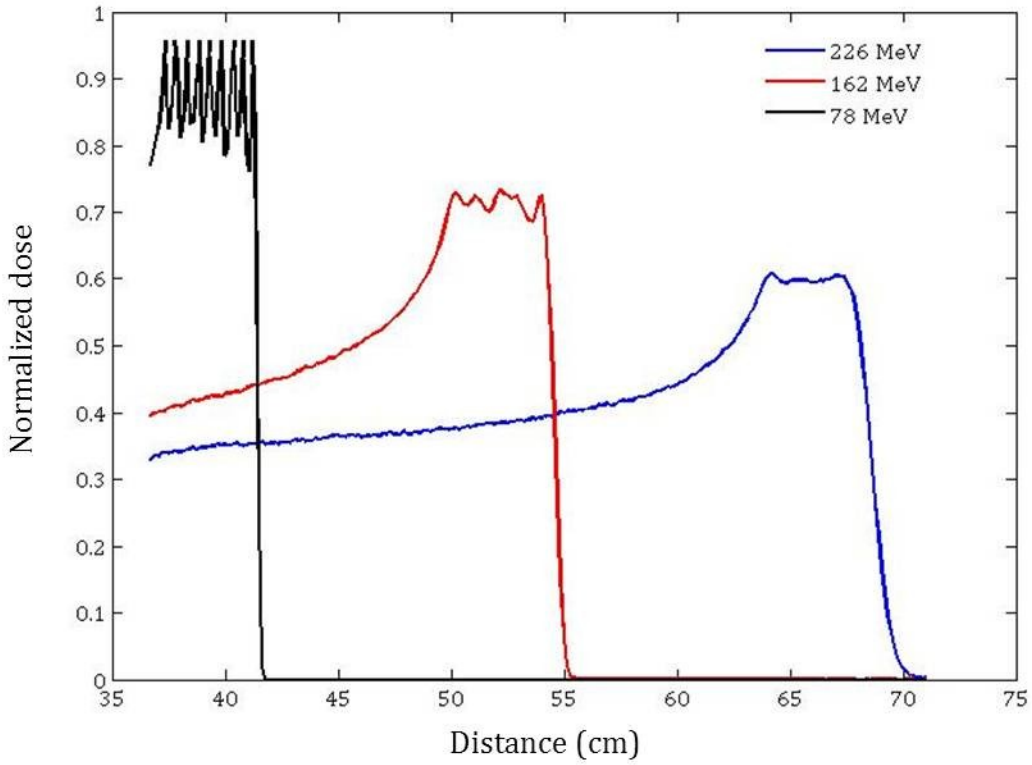

Figure 6.8: Bragg-peak of individual primary proton beam and the calculated SOBP for the maximum energy of 226 MeV.

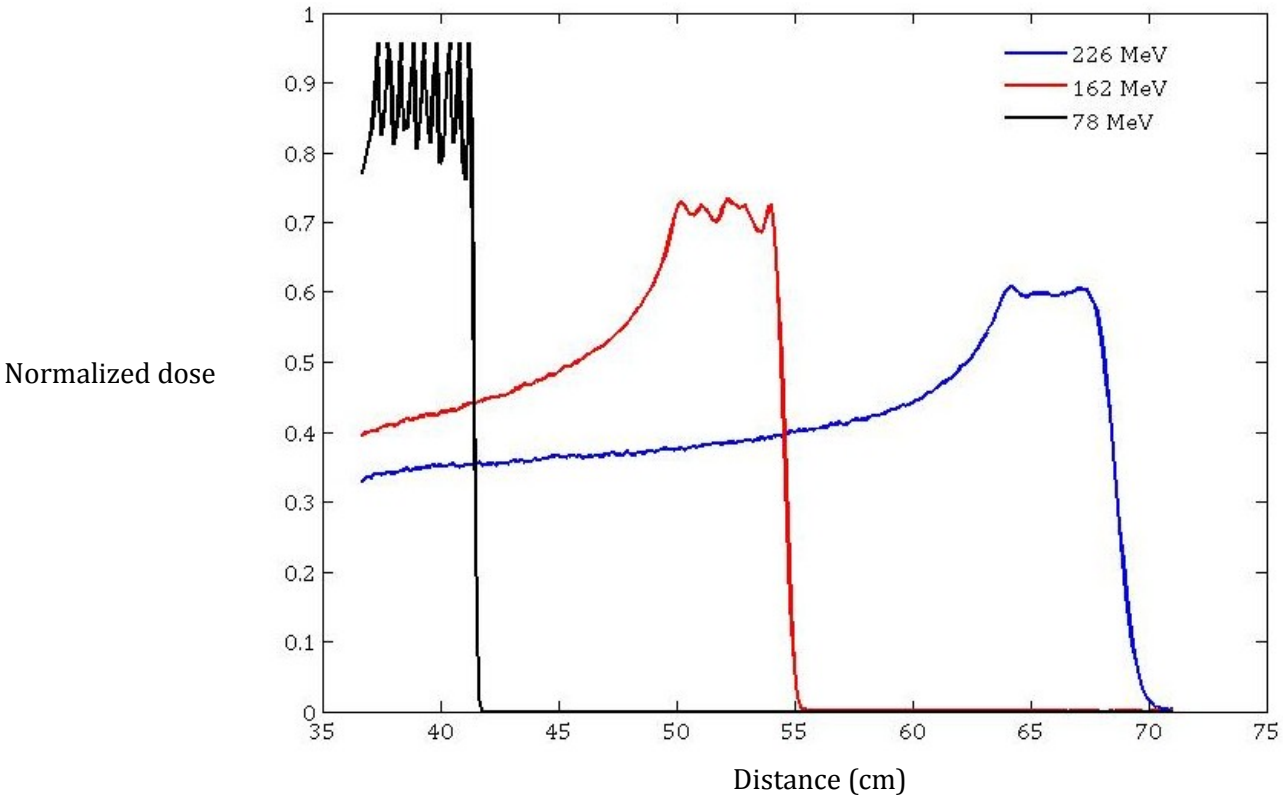

Figure 6.9: The generated SOBP for 78 MeV, 126 MeV and 226 MeV proton beam.

Figure 6.9 shows that the dose uniformity in the SOBP region is better for the 226 MeV proton beams compared to 162 MeV and 78 MeV. This is because the width of the Bragg-peak is inherently greater for 226 MeV protons than the other two beams and this makes the SOBP region more uniform. The relatively larger width of the Bragg-peak for higher energy occurs due to the range straggling effect. In order to make a more uniform SOBP dose region for the 162 MeV and 78 MeV proton beams, a large number of beams could be used. However, this is not practical in an actual treatment situation.

After being determination of SOBP, the SOBP dose is used to normalize the dose equivalent as shown:

$$\frac{H_n}{D_p} = \sum_i \frac{\left(\frac{H_p}{p}\right)}{\left(\frac{D_p}{p}\right)}. \qquad 6.2$$

H_n/p represents the dose equivalent due to secondary neutrons per unit primary proton and Dp/p represents the dose at SOBP per unit primary proton. H_n/D_p represents the ratio of dose equivalent due to secondary neutrons to primary proton dose. This method is used in this study to represent the FLUKA simulated neutron dose equivalent, where for each energy $\sim 10^8$ primaries and 5 different runs were performed to produce the dose equivalent at each detector's location.

CHAPTER 7

RESULTS

This chapter presents the off-axis dose equivalent results from secondary neutrons at different locations in all four experimental configurations. Several layers of CR-39 PNTDs were placed inside the phantom (solid-phantom and hollow-phantom configurations) and in the air (in-air and cylindrical-phantom configurations) for the determination of dose equivalent. The dose equivalent values due to experiment and simulation are shown as the ratio of dose equivalent to absorbed proton dose (H_n/D_p) at each detector location. H_n/D_p as functions of distance, energy, and angle are presented. Comparisons of measured and simulated H_n/D_p for different configurations are also described.

7.1.1 H_n/D_p for solid-phantom, in-air, hollow-phantom, and cylindrical-phantom configuration

Table 7.1 lists the experimentally measured and FLUKA simulated dose equivalent H_n/D_p values due to solid-phantom, in-air, hollow-phantom, and cylindrical-phantom configurations for a 78 MeV proton beam. H_n/D_p is listed at each detector's location for different angles and distances inside the phantom and in

air. The angle was measured from primary beam direction and the distance of the detector was measured from the beam isocenter. For the solid-phantom configuration (inside the phantom), the experimentally measured H_n/D_p values ranged from 0.31±0.08 mSv/Gy to 7.47±1.42 mSv/Gy and the FLUKA simulated H_n/D_p values ranged from 0.11 ± 0.01 mSv/Gy to 3.81 ± 0.02 mSv/Gy. For the in-air configuration (in the air), the experimentally measured H_n/D_p values ranged from 2.50±0.22 mSv/Gy to 9.25±1.48 mSv/Gy and the FLUKA simulated H_n/D_p ranged from 1.21 ± 0.06 mSv/Gy to 5.12 ± 0.27 mSv/Gy. For the hollow-phantom configuration (inside the phantom), the experimentally measured H_n/D_p values ranged from 2.12 ± 0.19 mSv/Gy to 7.31 ± 0.78 mSv/Gy and the FLUKA simulated H_n/D_p values ranged from 0.13±0.01 mSv/Gy to 7.29 ± 0.02 mSv/Gy. For the cylindrical-phantom configuration (in the air), the experimentally measured H_n/D_p values ranged from 2.72±0.28 mSv/Gy to 35.61 ± 1.48 mSv/Gy and the FLUKA simulated H_n/D_p values ranged from 2.06 ± 0.12 mSv/Gy to 11.41 ± 0.41 mSv/Gy.

Table 7.1: Experimentally measured and FLUKA simulated ratios of neutron dose equivalent to proton absorbed dose (H_n/D_p) for a 78 MeV primary proton beam at detector locations in the solid-phantom, in air, inside the hollow-phantom, and outside the cylindrical-phantom configuration. All the distance is measured from beam isocenter.

Proton Beam (MeV)	Angle	Dist. in phantom (cm)	(H_n/D_p) (mSv/Gy)		Dist. in air (cm)	(H_n/D_p) (mSv/Gy)	
			Exp.	FLUKA		Exp.	FLUKA
		solid-phantom			**in-air**		
78	45°	7.5	1.35±0.10	1.51 ± 0.02	7.5	6.71±1.21	2.71±0.12
		17.5	0.85±0.06	0.43 ± 0.01	16.3	4.12±0.50	2.11±0.07
		28.5	0.56±0.11	0.21 ± 0.01	28.5	3.91±0.31	1.52±0.08
		35.5	0.31±0.08	0.11 ± 0.01	35	2.50±0.22	1.21±0.06
	90°	7.5	2.36±0.15	1.91 ± 0.02	12.5	6.61±0.41	3.41±0.17
		17.5	1.24±0.11	0.52 ± 0.02	18.2	2.71±0.16	2.82±0.12
		28.5	0.71±0.11	0.23 ± 0.01	40	1.42±0.07	2.23±0.11
		35.5	0.49±0.07	0.13 ± 0.01	50	1.35±0.08	1.91±0.07
	135°	7.5	7.47±1.42	3.81 ± 0.02	9.3	9.25±1.48	4.31±0.21
		18.2	1.71±0.11	1.41 ± 0.02	17.2	6.53±0.87	5.03±0.26
		25.5	1.12±0.07	1.02 ± 0.02	29.5	3.24±0.21	5.12±0.27
		35.5	2.31±0.17	1.43 ± 0.01	33	3.11±0.21	4.71±0.23
		hollow-phantom			**cylindrical-phantom**		
	45°	7.5	4.68±2.14	2.14±0.15	7.5	9.64±1.01	8.21±0.41
		17.5	3.29±1.09	1.11±0.07	16.3	5.15±0.51	6.66±0.31
		28.5	2.47±0.22	0.41±0.03	28.5	4.27±0.41	6.15±0.29
		35.5	2.12±0.19	0.23 ±0.01	35	2.72±0.28	2.06±0.12
	90°	7.5	3.01±0.36	3.97±0.23	7.5	15.98±1.45	9.36±0.75
		17.5	2.61±0.29	1.64±0.09	17.5	7.95±0.65	8.94±0.71
		28.5	2.33±0.27	0.51±0.02	32	6.68±0.58	4.57±0.41
		35.5	2.03±0.23	0.35±0.01	40	4.26±0.38	6.02±0.56
	135°	7.5	7.31±0.78	7.29± 0.71	7.5	35.61±1.48	11.41±0.41
		17.5	3.23±0.32	3.61±0.32	17.5	9.08±0.87	9.41±0.32
		35	4.88±0.54	4.47±0.41	35	6.25±0.21	10.56±0.42

Figure 7.1 shows the dose equivalent per proton absorbed dose (H_n/D_p) for a 78 MeV proton beam for solid-phantom configuration. Solid lines are the experimentally measured data and dotted lines are the FLUKA simulated data. In general, H_n/D_p decreases as a function of distance for both measured and simulated data at all angles (45°, 90°, and 135°) inside the phantom. This is expected because as the distance from the beam isocenter increases, more neutrons are attenuated inside the phantom, leading to a decrease in H_n/D_p with distance. An exception is that an increase of H_n/D_p is observed at 35.5 cm at 135°. The reason behind the increase is: a) at 135°, the detector was closer to snout which led to a higher neutron fluence, and b) at 35.5 cm, the detector was closer to the front surface of the phantom, causing the neutrons not to be attenuated as much as they would have at greater depths in the phantom.

Figure 7.2 shows the experimentally measured and FLUKA simulation data of H_n/D_p as a function of distance from isocenter for a 78 MeV proton beam for in-air configuration. A decreasing trend in H_n/D_p with distance is again visible in air except that at 135° an increase of H_n/D_p with distance is visible in the FLUKA simulated result. Overall, higher values of H_n/D_p can be seen in air versus inside the phantom at all angles.

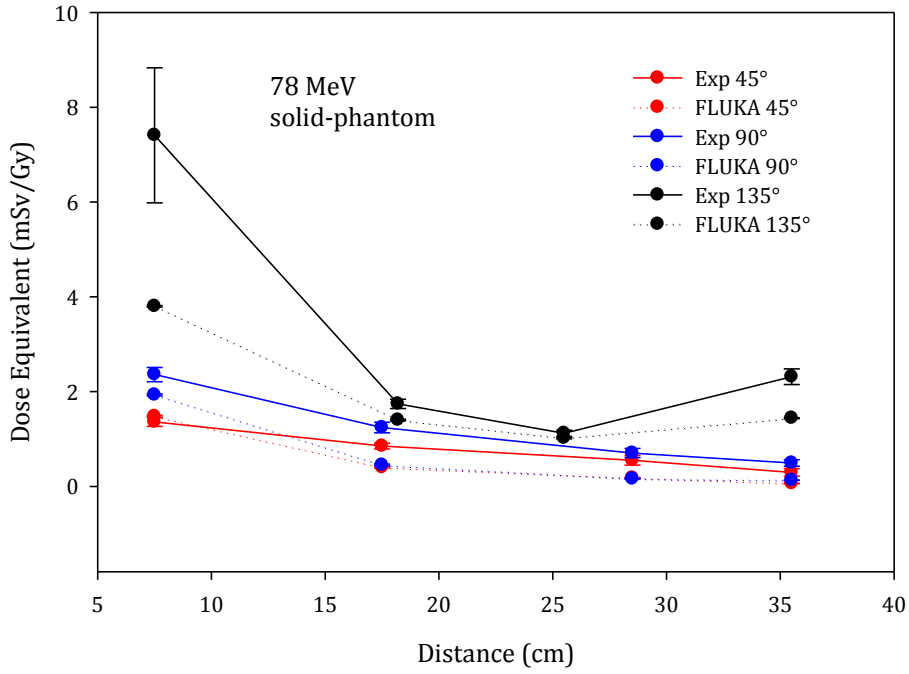

Figure 7.1: Experimentally measured (solid) and FLUKA simulated (dotted)neutron dose equivalent per therapeutic proton absorbed dose, H_n/D_p, for a 78 MeV proton beam inside the phantom for solid-phantom configuration at increasing distances from isocenter at 45°, 90° and 135° to the direction of the beam.

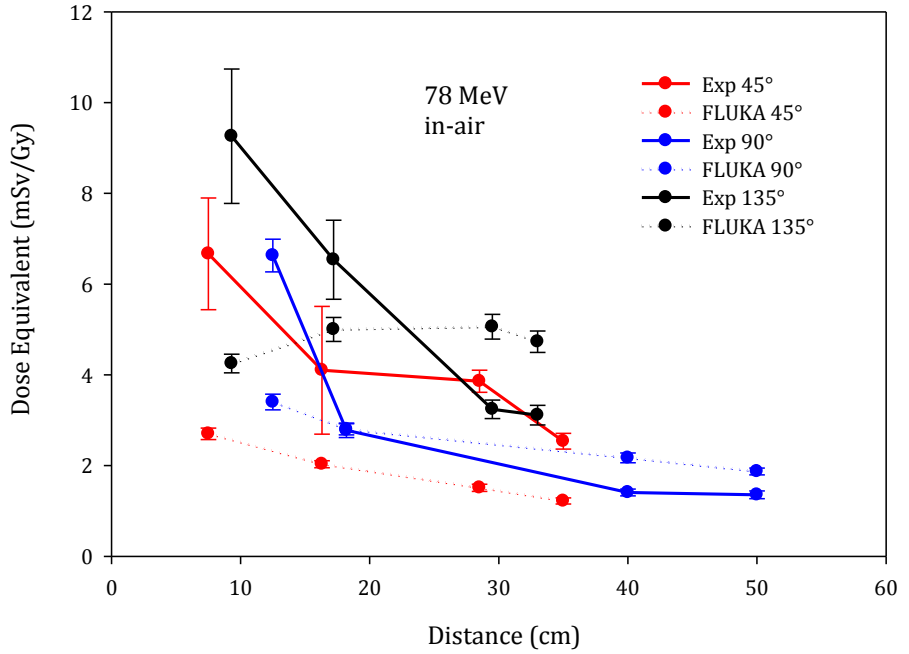

Figure 7.2: Experimentally measured (solid)and FLUKA simulated (dotted) neutron dose equivalent per therapeutic proton absorbed dose, H_n/D_p, for a 78 MeV proton beam in the air for in-air configuration at increasing distances from isocenter at 45°, 90° and 135° to the direction of the beam.

To help clarify the increased H_n/D_p values in air with distance at 135° in the FLUKA simulated data (dotted black line in Figure 7.2), a FLUKA simulation of the neutron fluence spectrum for a 78 MeV proton beam for the in-air configuration at 135° to the primary beam is shown in Figure 7.3. This plot is shown for neutrons of energy from 1 to 20 MeV, since H_n/D_p was scored in this energy range. As can be seen, at smaller distance (9.3 cm), the fluence is lower while at larger distance (33 cm), the fluence is higher. This is because at larger distances from isocenter (33 cm), the detector is actually closer to the snout where a significant number of neutrons are present due to evaporation processes. This higher fluence of neutrons leads to higher dose equivalent in the FLUKA simulated results. However, at 135° the experimentally measured H_n/D_p value (solid black line in Figure 7.2) shows a decrease in dose equivalent as the distance increases. The disagreement between experiment and simulation at 135° could be due to the following reasons: a) closer to the snout the primary contribution mostly comes from low energy isotropic neutrons of about 1 MeV, where CR-39 PNTD just starts registering tracks from neutrons, b) differences in the way dose equivalent is calculed, i.e. FLUKA converts fluence to dose equivalent by using tabulated conversion coefficients, while CR-39 PNTD measures dose equivalent based on the incident particle's LET, and c) the difference in actual neutron cross section as exhibited in CR-39 PNTD versus the tabulated and interpolated cross section library used in FLUKA.

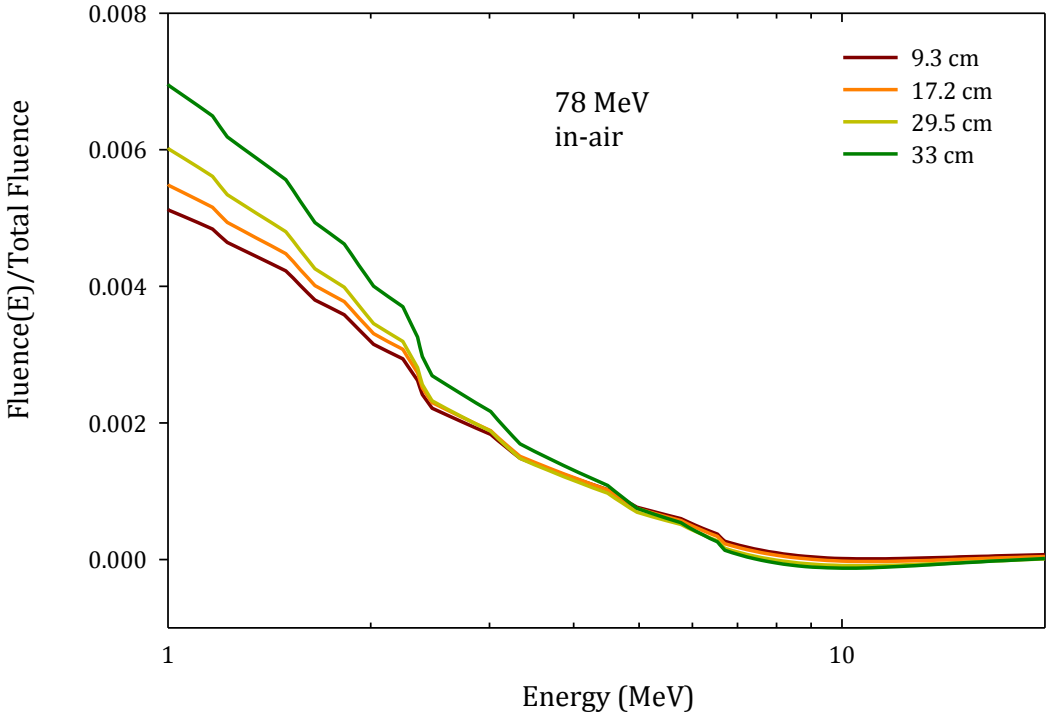

Figure 7.3. FLUKA simulated neutron energy spectra from a 78 MeV proton beam for the in-air configuration at 135° and 9.3 cm, 17.2 cm, 29.5 cm, and 33 cm distances from beam isocenter.

Figure 7.4 shows the experimentally measurements and FLUKA simulations of H_n/D_p as a function of distance from isocenter for the hollow-phantom configuration. In general, H_n/D_p decreases as a function of distance at all angles (45°, 90°, and 135°). An increase in H_n/D_p is again observed at 35 cm at 135° inside the phantom. This is because in the hollow-phantom configuration, detectors were placed inside the phantom at the same locations as inside the solid-phantom configuration. Figure 7.5 shows experimental measurements and FLUKA simulations of H_n/D_p for the 78 MeV proton beam for the cylindrical-phantom configuration. A decreasing trend in H_n/D_p with distance is again visible for the

cylindrical-phantom configuration and is similar to that observed for the in-air configuration.

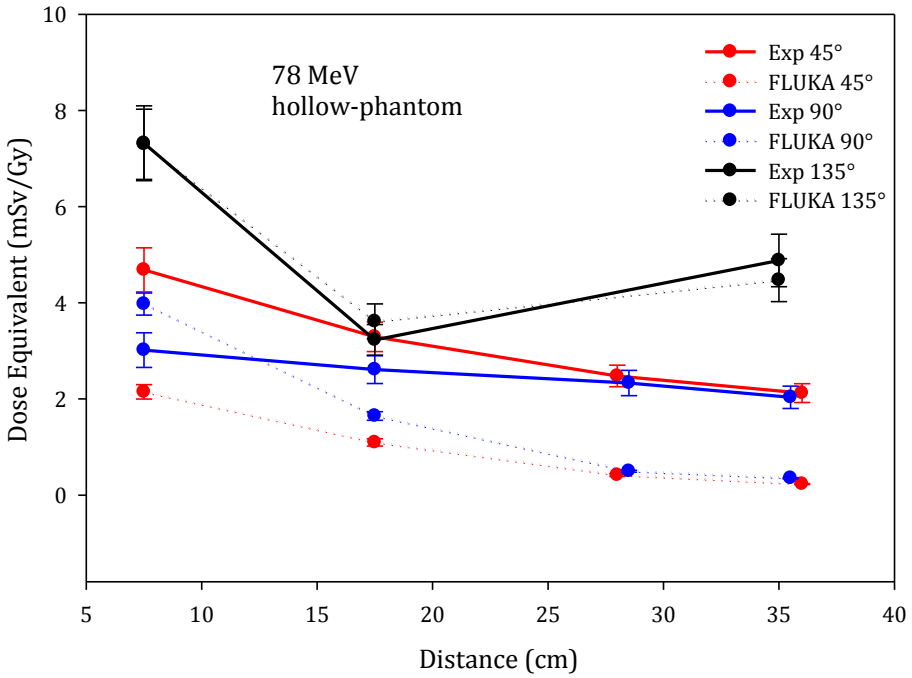

Figure 7.4: Experimentally measured (solid) and FLUKA simulated (dotted) neutron dose equivalent per therapeutic proton absorbed dose, H_n/D_p, for a 78 MeV proton beam for hollow-phantom configuration at increasing distances from isocenter at 45°, 90° and 135° to the direction of the beam.

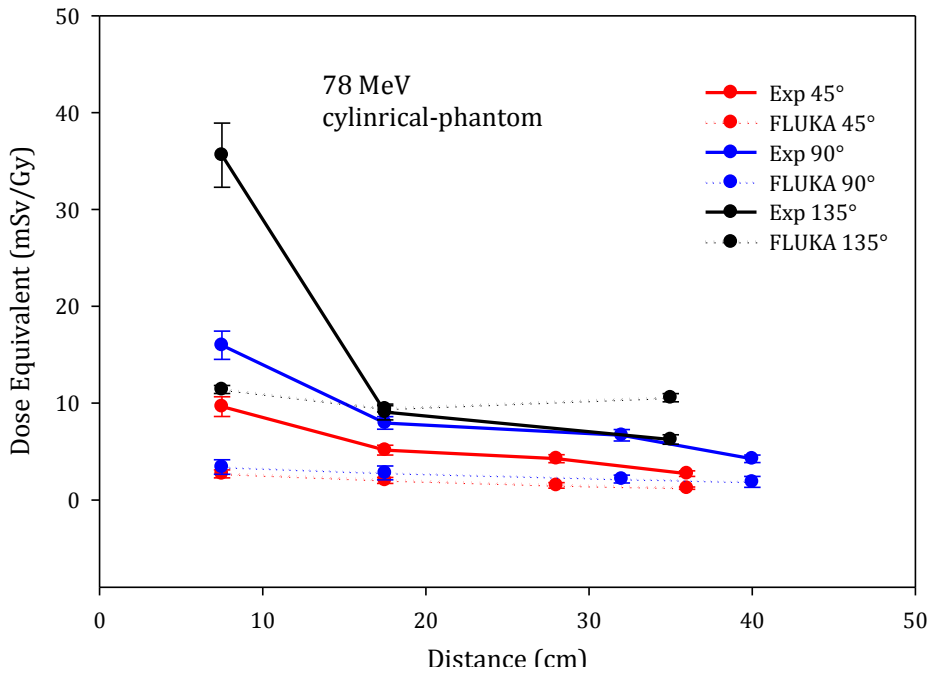

Figure 7.5: Experimentally measured (solid) and FLUKA simulated (dotted) neutron dose equivalent per therapeutic proton absorbed dose, H_n/D_p, for a 78 MeV proton beam for cylindrical-phantom configuration at increasing distances from isocenter at 45°, 90° and 135° to the direction of the beam.

A general decrease in H_n/D_p was observed in all these configurations both inside the phantom (solid-phantom and hollow-phantom) and in air (in-air and cylindrical -phantom) for a 78 MeV proton beam. Also, at 135° to primary beam an increase in H_n/D_p was observed at larger distances from beam isocenter for all the configurations. This is due to this particular location actually being closer to the snout, where many secondary neutrons are produced, than the other locations.

Table 7.2 lists the experimentally measured and FLUKA simulated H_n/D_p values for the solid-phantom, in-air, hollow-phantom, and cylindrical-phantom configurations for a 162 MeV proton beam. For the solid-phantom configuration (inside the

phantom), the experimentally measured H_n/D_p values ranged from 1.29±0.17 mSv/Gy to 12.95±1.72 mSv/Gy and the FLUKA simulated H_n/D_p values ranged from 1.01±0.06 mSv/Gy to 19.31±0.24 mSv/Gy. For the in-air configuration (in the air), the experimentally measured H_n/D_p values ranged from 3.74±0.61 mSv/Gy to 22.61±2.51 mSv/Gy and the FLUKA simulated H_n/D_p values ranged from 9.91±0.34 mSv/Gy to 33.21±0.53 mSv/Gy. For the hollow-phantom configuration (inside the phantom), the experimentally measured H_n/D_p values ranged from 2.25 ± 0.22 mSv/Gy to 29.49 ± 2.51 mSv/Gy and the FLUKA simulated H_n/D_p values ranged from 2.73 ± 0.31 mSv/Gy to 39.92 ± 2.71 mSv/Gy. For the cylindrical-phantom configuration (in the air), the experimentally measured H_n/D_p values ranged from 10.12 ± 0.81 mSv/Gy to 50.01 ± 3.5 mSv/Gy and the FLUKA simulated H_n/D_p values ranged from 20.11 ± 1.59 mSv/Gy to 82.22 ± 9.11 mSv/Gy.

Table 7.2: Experimentally measured and FLUKA simulated ratios of neutron dose equivalent to proton absorbed dose (H_n/D_p) for a 162 MeV primary proton beam at detector locations for solid-phantom, in-air, hollow-phantom, and cylindrical-phantom configuration. All the distance is measured from beam isocenter.

Proton Beam (MeV)	Angle	Dist. in phantom (cm)	(H_n/D_p) (mSv/Gy)		Dist. in air (cm)	(H_n/D_p) (mSv/Gy)	
			Exp.	FLUKA		Exp.	FLUKA
			solid-phantom			**in-air**	
162	45°	7.5	13.31±1.42	14.12±0.6	7.5	17.71±2.21	21.51±0.49
		17.5	2.31±0.27	5.41±0.35	16.3	10.58±1.36	16.01±0.38
		28.5	2.04±0.25	2.01±0.21	28.5	5.26±0.72	11.72±0.35
		35.5	1.29±0.17	1.01±0.06	35	3.74±0.61	9.91±0.34
	90°	7.5	7.01±1.83	16.61±0.6	12.5	12.21±1.26	26.01±0.52
		17.5	4.05±0.82	4.71±0.24	18.2	8.39±1.27	21.02±0.42
		28.5	2.21±0.12	2.12±0.07	40	4.76±0.75	17.02±0.47
		35.5	1.71±0.11	1.40±0.07	50	3.79±0.56	14.01±0.42
	135°	7.5	12.95±1.72	19.31±0.2	9.3	22.61±2.51	33.21±0.53
		18.2	4.12±0.42	13.32±0.6	17.2	13.25±1.46	39.31±0.71
		25.5	3.01±0.41	10.21±0.2	29.5	7.82±1.01	39.22±0.78
		35.5	4.21±0.40	12.51±0.2	33	8. 6±1.12	36.52±0.73
			hollow-phantom			**cylindrical-phantom**	
	45°	7.5	7.68±0.71	16.17±1.56	7.5	45.72±3.31	71.81±5.23
		17.5	5.83±0.53	14.08±1.41	16.3	21.01±2.35	41.14±2.36
		28.5	3.78±0.37	7.17±0.65	28.5	14.89±1.32	28.45±2.27
		35.5	2.25±0.22	2.73±0.31	35	10.12±0.81	20.11±1.59
	90°	7.5	8.11±0.74	34.53±3.89	7.5	37.45±3.77	65.97±5.27
		17.5	3.60±0.61	8.97±1.07	17.5	15.01±1.19	55.67±4.38
		28.5	3.22±0.46	6.23±0.75	32	7.92±0.71	46.03±3.65
		35.5	2.33±0.31	10.61±1.27	40	5.61±0.46	33.20±2.63
	135°	7.5	29.49±2.51	39.92±2.71	7.5	50.01±3.51	82.22±9.11
		17.5	7.58±0.71	27.25±1.12	17.5	15.51±1.13	89.18±6.23
		35	16.38±1.65	29.72±1.56	35	16.56±1.32	62.50±6.54

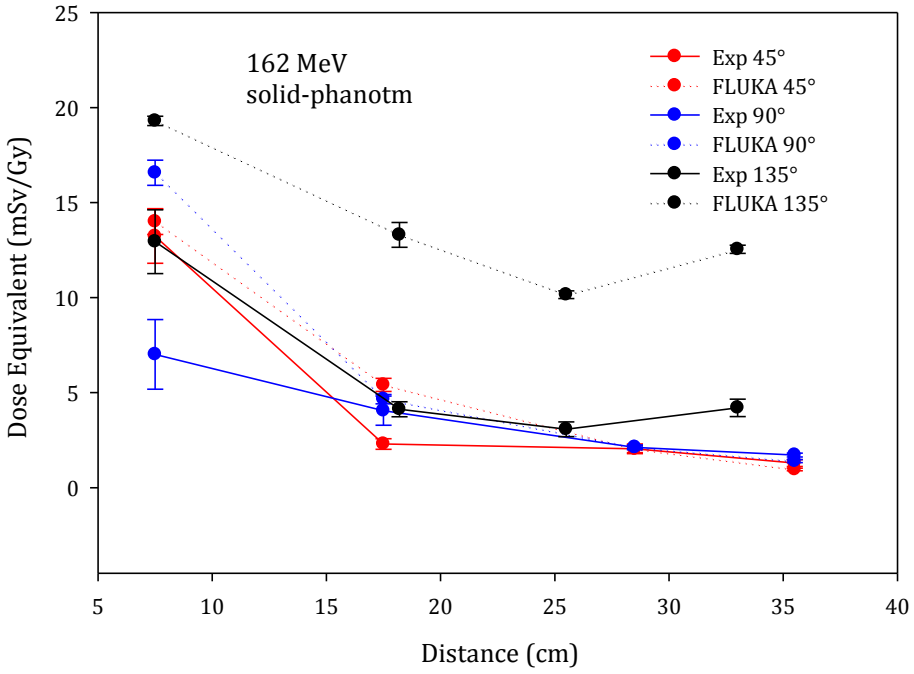

Figure 7.6: Experimentally measured (solid) and FLUKA simulated (dotted) neutron dose equivalent per therapeutic proton absorbed dose, H_n/D_p, for a 162 MeV proton for solid-phantom configuration at increasing distances from isocenter at 45°, 90° and 135° to the direction of the beam.

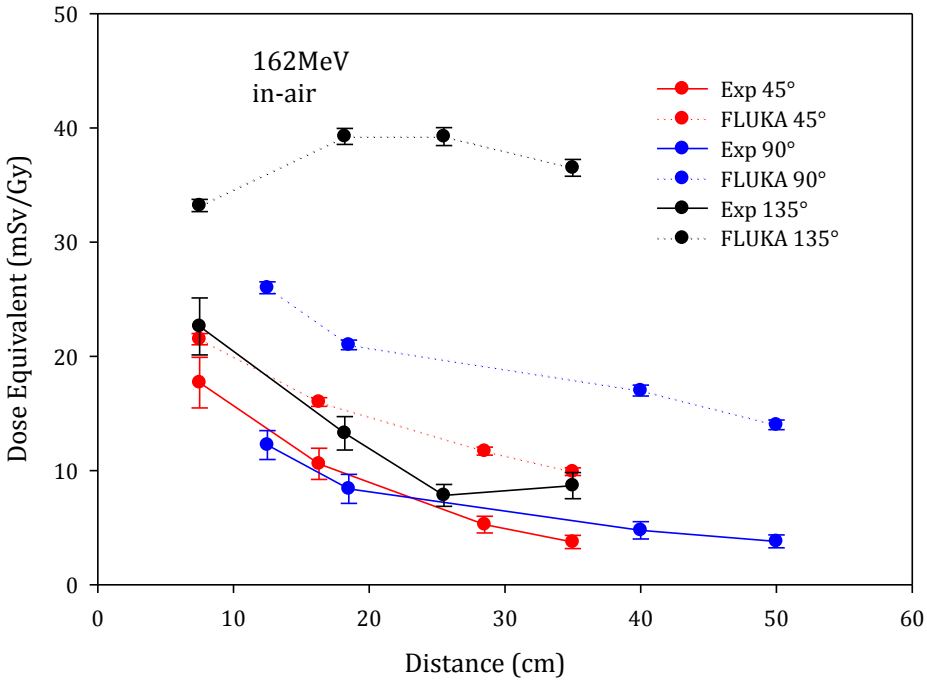

Figure 7.7: Experimentally measured (solid) and FLUKA simulated (dotted) neutron dose equivalent per therapeutic proton absorbed dose, H_n/D_p, for a 162 MeV proton beam for the in-air configuration at increasing distances from isocenter at 45°, 90° and 135° to the direction of the beam.

Figure 7.6, Figure 7.7, Figure 7.8, and Figure 7.9 represents the H_n/D_p for a 162 MeV proton beam for solid-phantom, in-air, hollow-phantom, and cylindrical-phantom configurations, respectively. A general decrease in H_n/D_p was observed for all these configurations both inside the phantom (solid-phantom and hollow-phantom) and in the air (in-air and cylindrical -phantom). Similar to the 78 MeV proton beam, an increase in H_n/D_p inside the phantom was observed at 35.5 cm distance at 135° to primary beam direction. In air, the FLUKA simulated H_n/D_p also increased as a function of distance.

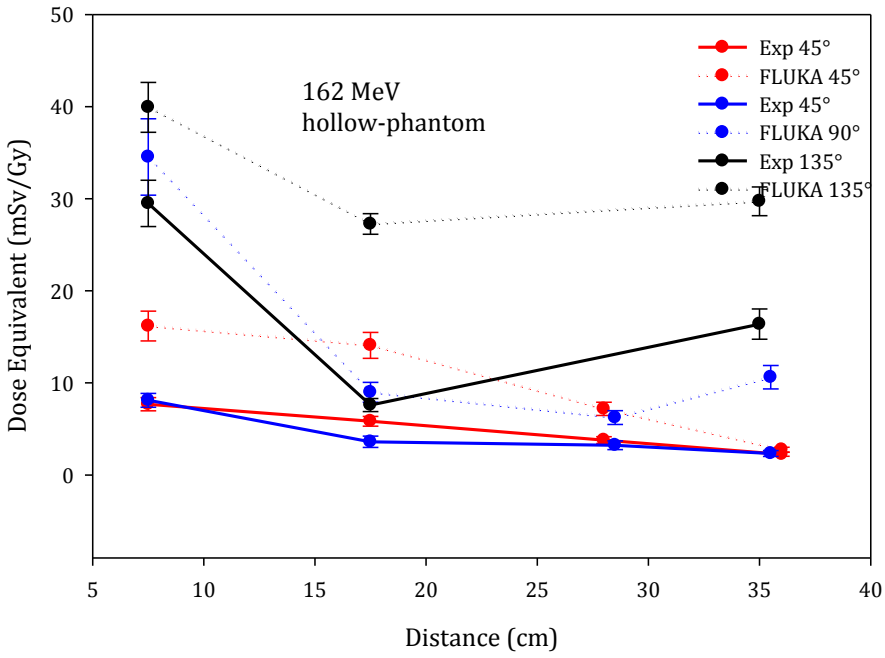

Figure 7.8: Experimentally measured (solid) and FLUKA simulated (dotted) neutron dose equivalent per therapeutic proton absorbed dose, H_n/D_p, for a 162 MeV proton beam for hollow-phantom configuration at increasing distances from isocenter at 45°, 90° and 135° to the direction of the beam.

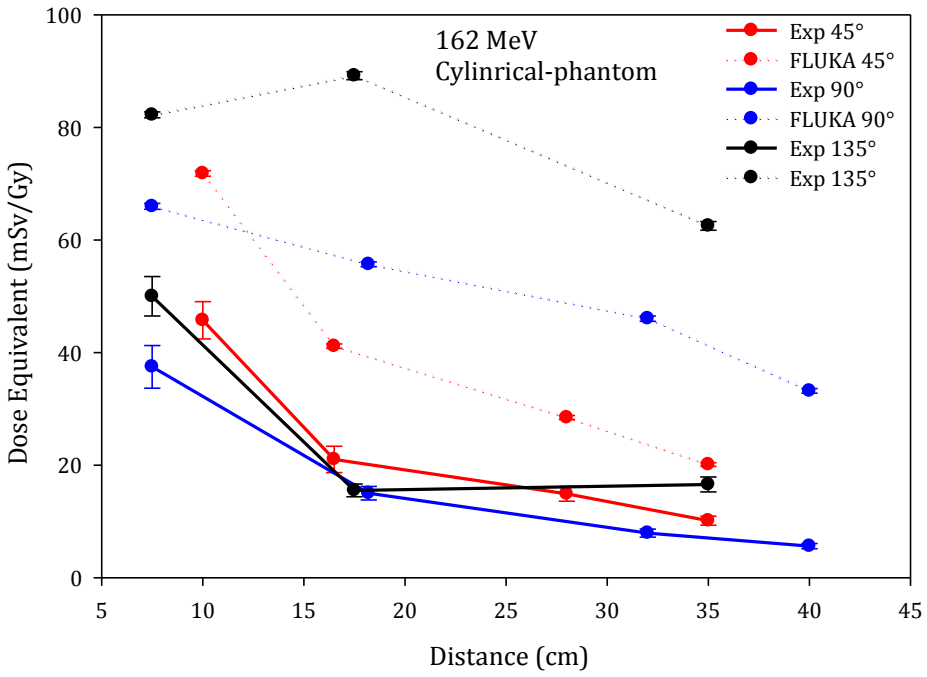

Figure 7.9: Experimentally measured (solid) and FLUKA simulated (dotted) neutron dose equivalent per therapeutic proton absorbed dose, H_n/D_p, for a 162 MeV proton beam for cylindrical-phantom configuration at increasing distances from isocenter at 45°, 90° and 135° to the direction of the beam.

Table 7.3 lists the experimentally measured and FLUKA simulated H_n/D_p values for the solid-phantom, in-air, hollow-phantom, and cylindrical-phantom configurations for a 226 MeV proton beam. For the solid-phantom configuration (inside the phantom), the experimentally measured H_n/D_p values ranged from 1.81 ± 0.42 mSv/Gy to 37.11 ± 1.72 mSv/Gy and the FLUKA simulated H_n/D_p values ranged from 2.51 ± 0.14 mSv/Gy to 69.21 ± 1.11 mSv/Gy. For the in-air configuration (in the air), the experimentally measured H_n/D_p values ranged from 4.82 ± 0.61 mSv/Gy to 37.41 ± 2.42 mSv/Gy and the FLUKA simulated H_n/D_p values ranged from 24.81 ± 0.82 mSv/Gy to 85.31 ± 1.81 mSv/Gy. For the hollow-phantom configuration (inside the phantom), the experimentally measured H_n/D_p values ranged from 2.09 ± 0.21 mSv/Gy to 25.42 ± 2.33 mSv/Gy and the FLUKA simulated H_n/D_p values ranged from 10.95 ± 0.89 mSv/Gy to 135.66 ± 6.71 mSv/Gy. For the

cylindrical-phantom configuration (in the air), the experimentally measured H_n/D_p values ranged from 10.21 ± 0.94 mSv/Gy to 46.20 ± 3.96 mSv/Gy and the FLUKA simulated H_n/D_p values ranged from 50.06 ± 1.23 mSv/Gy to 153.15 ± 8.51 mSv/Gy.

Figure 7.10, Figure 7.11, Figure 7.12, and Figure 7.13 show H_n/D_p as a function of distance from beam isocenter for a 226 MeV proton beam for solid-phantom, in-air, hollow-phantom, and cylindrical-phantom configurations, respectively. A general decrease in H_n/D_p was observed for all configurations both inside the phantom (solid-phantom and hollow-phantom) and in the air (in-air and cylindrical-phantom) configurations. Similar to the 78 MeV and 162 MeV proton beams, an increase in H_n/D_p inside the phantom was observed at a distance of 35.5 cm at 135° to the primary beam direction. In the air, the FLUKA simulated H_n/D_p was also observed to increase as a function of distance.

Table 7.3: Experimentally measured and FLUKA simulated ratios of neutron dose equivalent to proton absorbed dose (H_n/D_p) for a 226 MeV primary proton beam at detector locations for solid-phantom, in-air, hollow-phantom, and cylindrical-phantom configurations. All distances are measured from beam isocenter.

Proton Beam (MeV)	Angle	Dist. in phantom (cm)	(H_n/D_p) (mSv/Gy)		Dist. in air (cm)	(H_n/D_p) (mSv/Gy)	
			Exp.	FLUKA		Exp.	FLUKA
			solid-phantom			**in-air**	
226	45°	7.5	24.61±2.41	28.61±0.8	7.5	31.81±1.6	54.01±1.25
		17.5	5.23±0.91	12.11±0.6	16.3	12.91±1.3	40.31±1.08
		28.5	2.82±0.61	5.01±0.25	28.5	7.82±1.01	30.11±0.91
		35.5	1.81±0.42	2.51±0.14	35	4.82±0.61	24.81±0.82
	90°	7.5	16.61±1.57	35.41±0.9	12.5	23.06±2.4	66.11±1.32
		17.5	6.64±0.92	11.51±0.5	18.2	11.51±1.3	57.41±1.32
		28.5	4.81±0.57	5.52±0.25	40	8.53±1.11	45.02±1.26
		35.5	3.92±0.47	4.01±0.19	50	7.12±0.92	38.31±1.14
	135°	7.5	37.11±2.41	69.21±1.1	9.3	37.41±2.4	85.31±1.80
		18.2	13.81±1.01	33.12±0.8	17.2	19.61±2.4	106.71±1.92
		25.5	10.20±0.63	38.03±0.8	29.5	18.62±1.9	111.01±1.99
		35.5	17.40±1.56	58.04±0.9	33	16.72±1.8	101.01±2.32
		hollow-phantom			**cylindrical-phantom**		
	45°	7.5	17.25±1.54	51.91±4.1	7.5	35.67±3.18	107.44±2.36
		17.5	6.11±0.48	14.17±1.1	16.3	27.44±2.35	66.32±1.08
		28.5	4.37±0.39	8.52±0.65	28.5	19.47±1.73	53.27±0.98
		35.5	3.93±0.38	12.98±1.0	35	10.21±0.94	50.06±1.23
	90°	7.5	22.18±2.27	74.68±7.6	7.5	46.20±3.96	131.35±1.23
		17.5	5.05±0.53	30.96±2.5	17.5	21.16±1.74	85.95±1.32
		28.5	3.27±0.32	11.39±1.0	32	12.61±1.19	85.44±1.56
		35.5	2.09±0.21	10.95±.89	40	10.22±1.03	59.54±1.78
	135°	7.5	25.42±2.33	135.66±6.	7.5	45.79±3.61	153.15±8.51
		17.5	13.46±1.23	71.99±3.6	17.5	16.95±2.75	163.48±7.45
		35	22.46±2.21	81.11±4.0	35	29.62±1.71	153.36±6.25

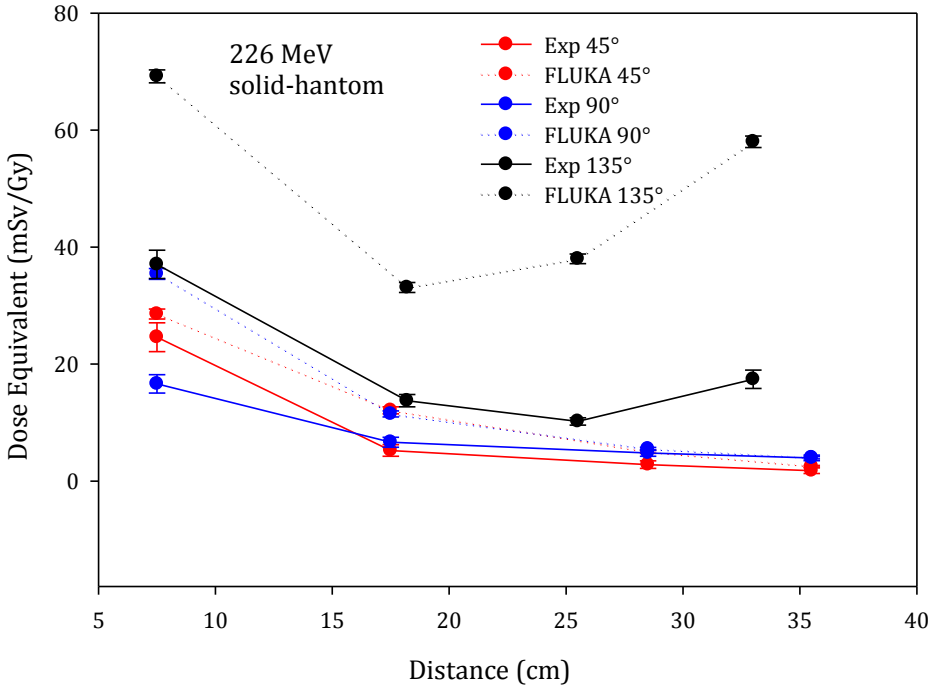

Figure 7.10: Experimentally measured and FLUKA simulated neutron dose equivalent per therapeutic proton absorbed dose, H_n/D_p, for a 226 MeV proton beam inside the phantom at increasing distances from isocenter at 45°, 90° and 135° to the direction of the beam.

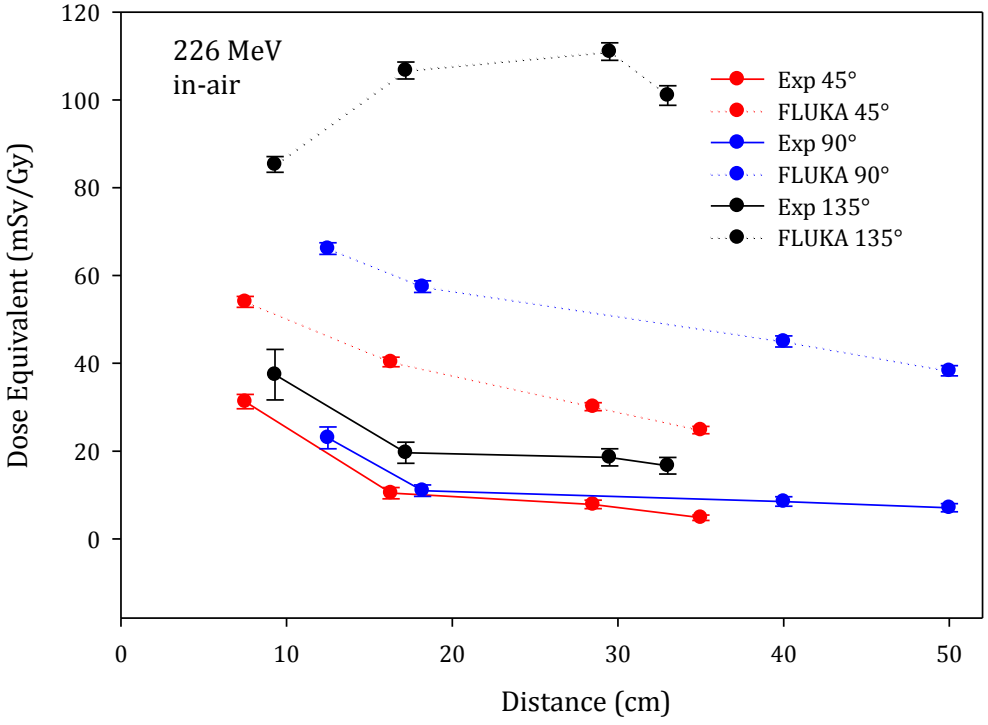

Figure 7.11: Experimentally measured and FLUKA simulated neutron dose equivalent per therapeutic proton absorbed dose, H_n/D_p, for a 226 MeV proton beam in air at increasing distances from isocenter at 45°, 90° and 135° to the direction of the beam.

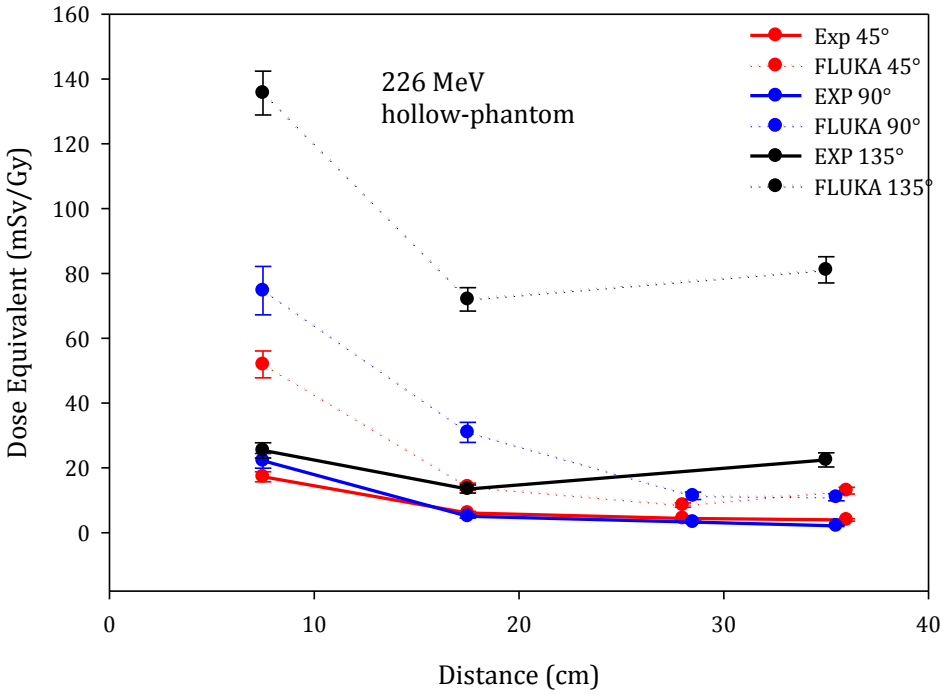

Figure 7.12: Experimentally measured and FLUKA simulated neutron dose equivalent per therapeutic proton absorbed dose, H_n/D_p, for a 226 MeV proton beam for hollow-phantom at increasing distances from isocenter at 45°, 90° and 135° to the direction of the beam.

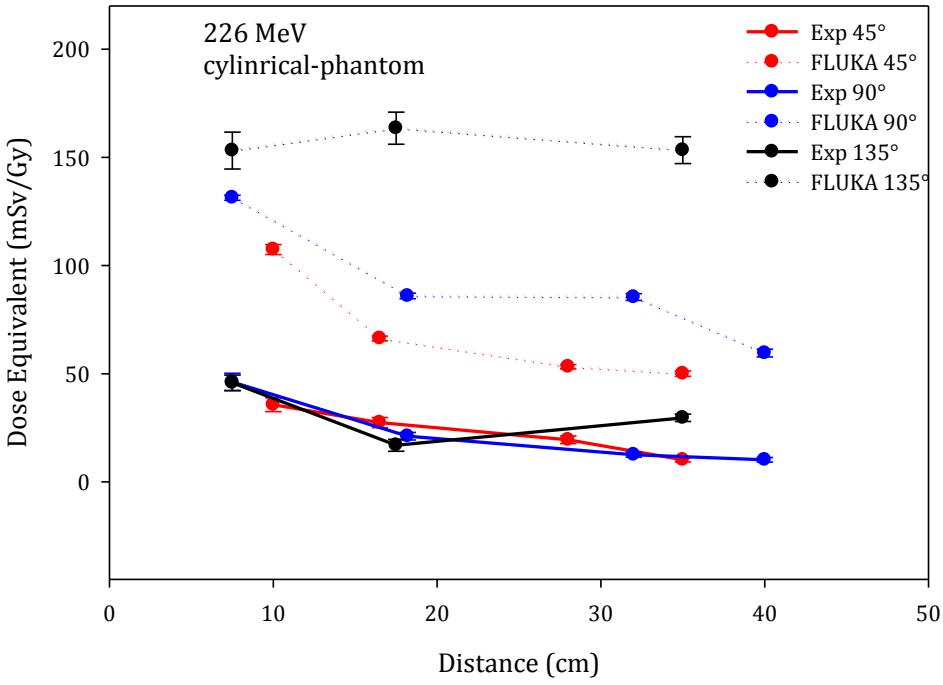

Figure 7.13: Experimentally measured and FLUKA simulated neutron dose equivalent per therapeutic proton absorbed dose, H_n/D_p, for a 226 MeV proton beam for cylindrical- phantom set up at increasing distances from isocenter at 45°, 90° and 135° to the direction of the beam.

The overall uncertainty in the experimentally measured H_n/D_p values were estimated to be 20%, while for the FLUKA simulation data, the uncertainty was less than or equal to 10%. For all configurations, both inside the phantom and in air, the simulated result agreed with experiment within a factor of 3 at most of the locations, but in few locations the agreement varied by up to a factor of 9.

7.1.2 Comparison of H_n/D_p among different configurations

Figure 7.14 and Figure 7.15 show the comparison of H_n/D_p between solid-phantom and in-air configurations for the experimentally measured and FLUKA simulated results, respectively. Figure 7.16 and Figure 7.17 shows the comparison of H_n/D_p between hollow-phantom and cylindrical-phantom configurations, for the experimentally measured and FLUKA simulation results, respectively. The results are shown for three different energies, 78 MeV, 162 MeV and 226 MeV, and three different angles, 45°, 90°, and 135°. Solid lines represent H_n/D_p inside the phantom (solid-phantom and hollow-phantom) and dotted lines represent H_n/D_p in air (in-air and cylindrical-phantom). The hollow-phantom configuration is labeled as "hop" and cylindrical-phantom configuration is labeled as "cyp" in the figures.

In general, H_n/D_p is higher in air than inside the phantom for all three angles. This is due to the fact that more neutrons were stopped, i.e. fewer neutrons reached the detector locations, inside the much denser phantom than in air. The largest difference in H_n/D_p between in-air and solid-phantom configurations and between

hollow-phantom and cylindrical-phantom configurations was observed for the 78 MeV proton beam. The experimentally measured H_n/D_p values varied by up to a factor of 7, while the FLUKA simulation H_n/D_p values varied by up to a factor of 18. This is probably due to the fact that secondary neutrons from 78 MeV proton are lower in average energy compared to the neutrons produced by 162 MeV and 226 MeV proton beam. For this reason, neutrons from 78 MeV are more easily attenuated inside the phantom than in air compared to neutrons from 162 MeV and 226 MeV proton beam.

The general trend of higher H_n/D_p values in air at all angles for both experiment (Figure 7.14 and Figure 7.16) and FLUKA simulation (Figure 7.15 and Figure 7.17) shows that the production of neutrons by beam shaping components (external neutrons) is much greater than the production of neutrons inside the phantom (internal neutrons). It is important to note that the phantom may produce significant numbers of thermal and epithermal neutrons (less than 1 MeV) but since CR-39 PNTD is not sensitive to neutrons in this energy regime, this study (both experiment and simulation) neglected neutrons of energy less than 1 MeV.

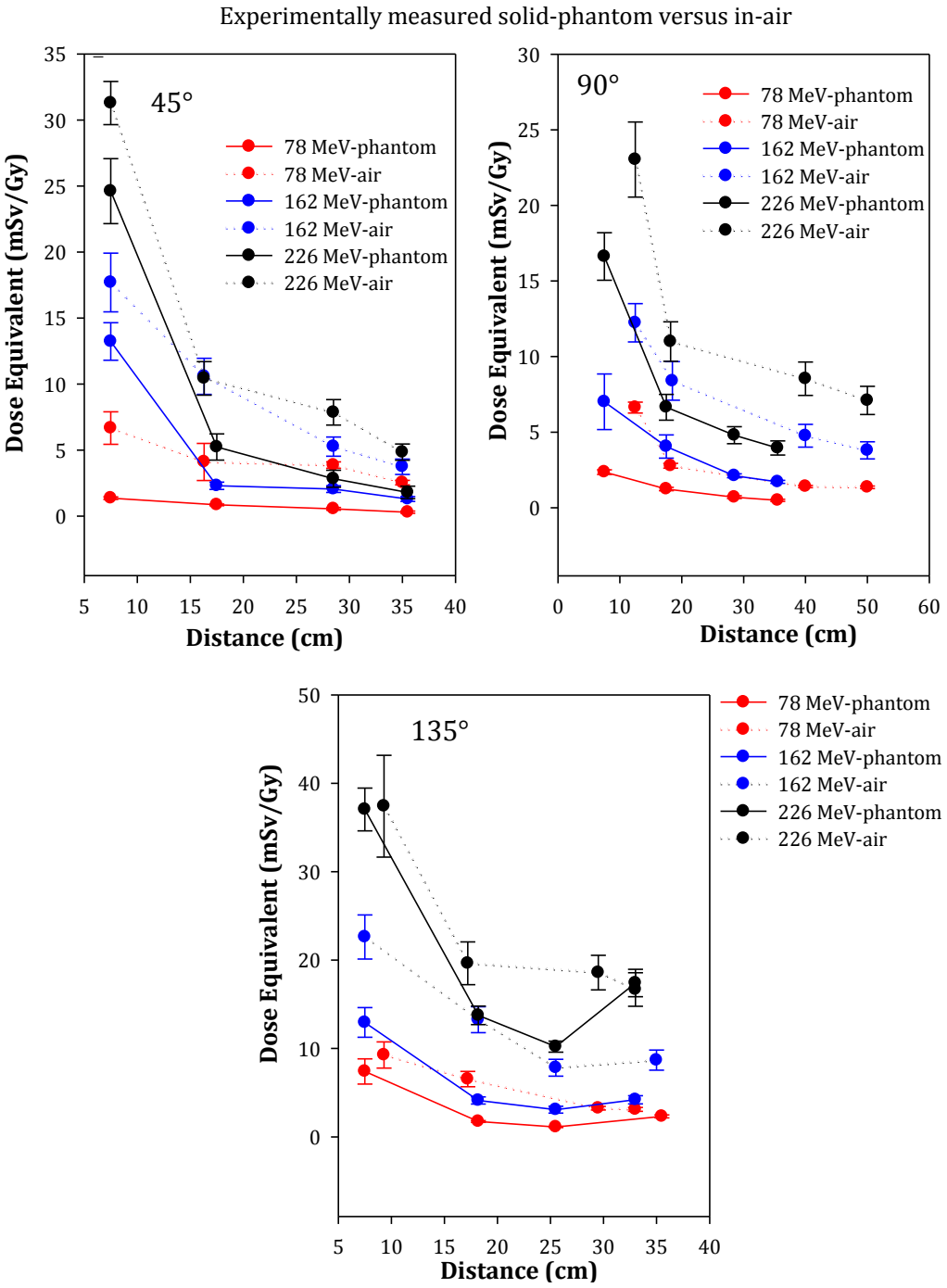

Figure 7.14: Experimentally measured dose equivalent per therapeutic proton absorbed dose, H_n/D_p, for 78MeV, 162 MeV, and 226 MeV proton beam for solid-phantom and in-air configuration at increasing distances from isocenter at 45°, 90° and 135° to the direction of the beam.

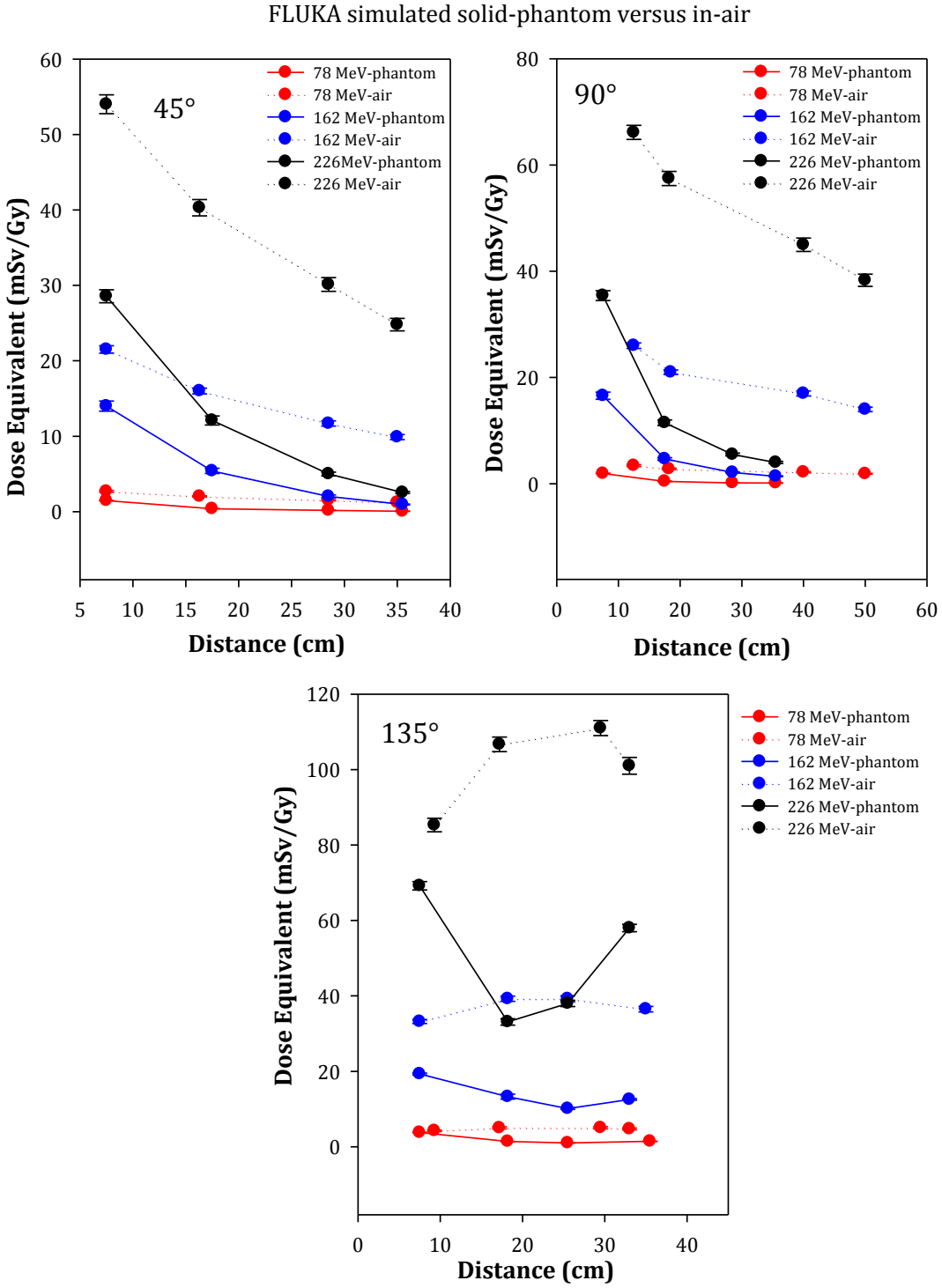

Figure 7.15: FLUKA simulated dose equivalent per therapeutic proton absorbed dose, H_n/D_p, for 78 MeV, 162 MeV, and 226 MeV proton beam for solid-phantom and in-air configuration at increasing distances from isocenter at 45°, 90° and 135° to the direction of the beam.

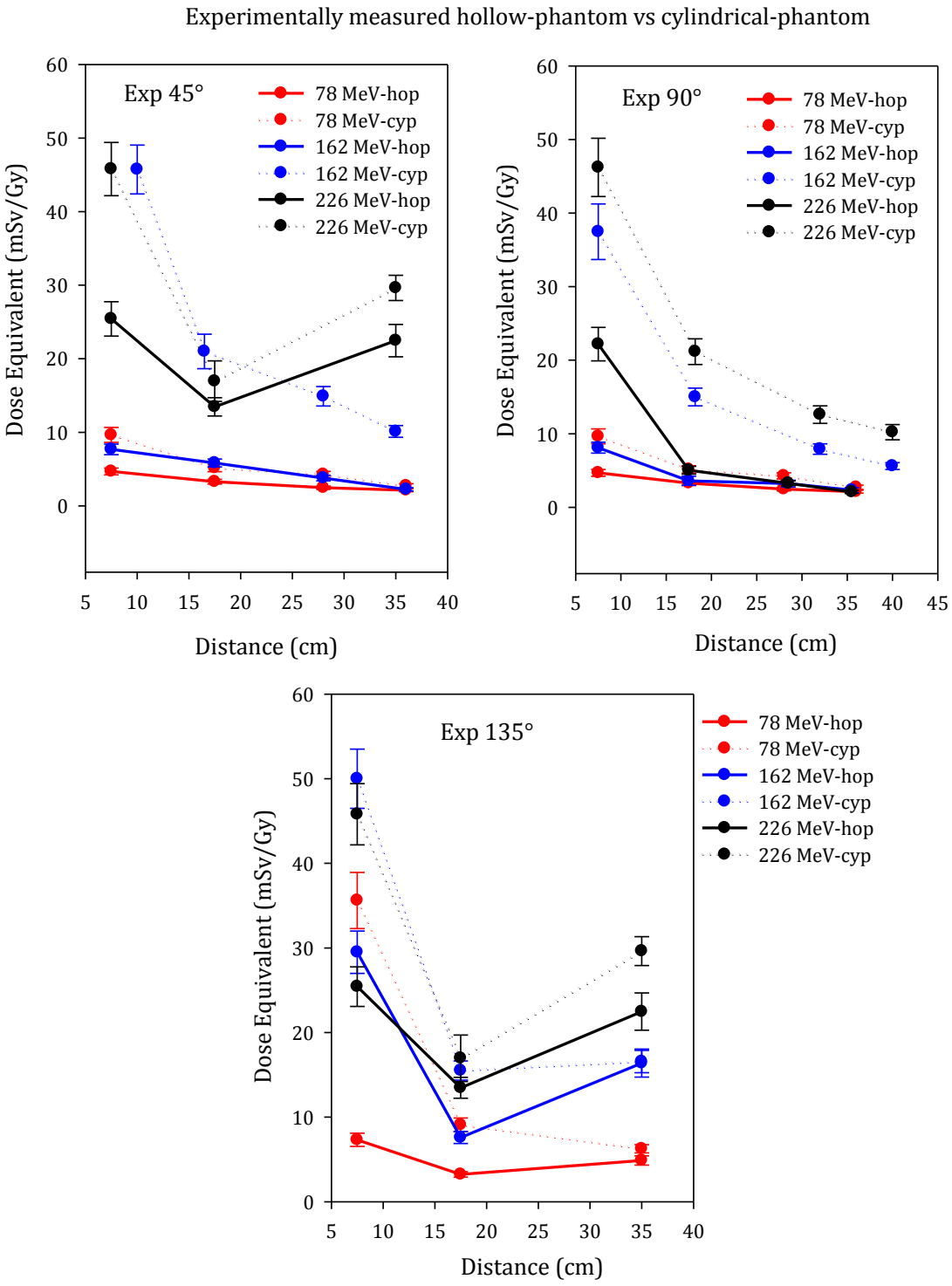

Figure 7.16: Experimentally measured dose equivalent per therapeutic proton absorbed dose, H_n/D_p, for 78MeV, 162 MeV, and 226 MeV proton beam for hollow-phantom (labeled as hop) and cylindrical-phantom (labeled as cyp) configuration at increasing distances from isocenter at 45°, 90° and 135° to the direction of the beam.

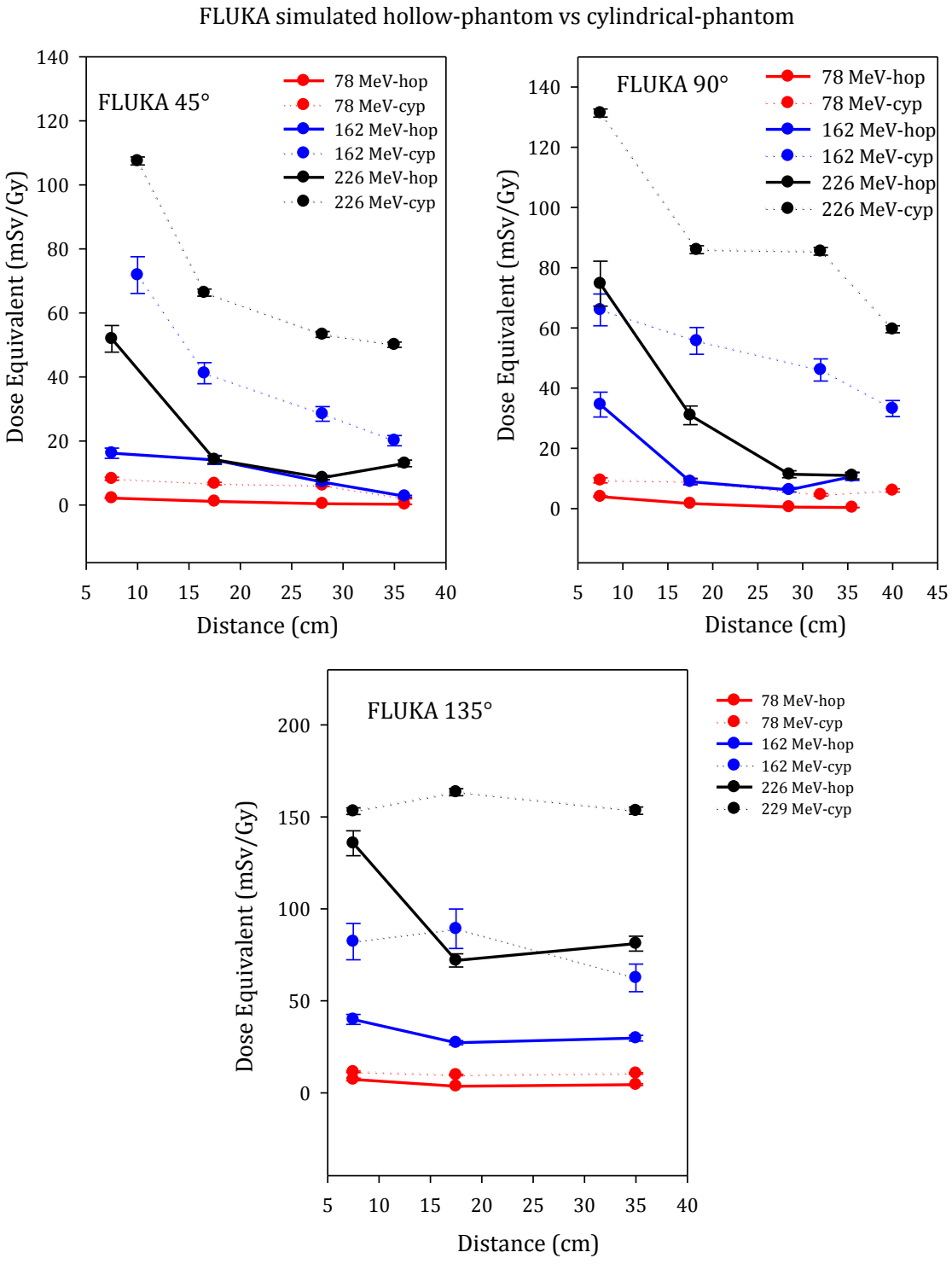

Figure 7.17: FLUKA simulated dose equivalent per therapeutic proton absorbed dose, H_n/D_p, for 78MeV, 162 MeV, and 226 MeV proton beam for hollow-phantom (labeled as hop) and cylindrical- phantom (labeled as cyp) configuration at increasing distances from isocenter at 45°, 90° and 135° to the direction of the beam.

In the hollow-phantom configuration, the contribution of internal neutrons to H_n/D_p should be small since the primary beam passed through the phantom without interacting with phantom material. On the other hand, in the cylindrical-phantom configuration, the contribution of internal neutrons to the H_n/D_p due to the protons interaction with phantom material should be substantial. For example, at 17.5 cm from beam isocenter and 90° to the primary beam, the experimentally measured H_n/D_p for a 226 MeV proton beam is 5 mSv/Gy and 21 mSv/Gy for the hollow-phantom and cylindrical-phantom configurations, respectively. The higher H_n/D_p for the cylindrical-phantom compared to hollow-phantom configuration suggests that the contribution due to internal neutrons could be added to that from external neutrons. However, a higher H_n/D_p (Figure 7.14 and Figure 7.15) for the in-air configuration compared to solid-phantom configuration was also observed even though there was no source of internal neutrons present. Considering this, it is not possible to predict the contribution of internal neutrons based on the four configurations.

To study the difference in H_n/D_p inside the phantom, a comparison of H_n/D_p for the 162 MeV proton beam is shown for the solid-phantom and hollow-phantom configurations. Figure 7.18 and Figure 7.19 shows the experimentally measured and the FLUKA simulation H_n/D_p values inside the phantom for the 162 MeV proton beam, respectively. In general, a higher H_n/D_p was observed in the hollow-phantom (dotted line) than in the solid-phantom configuration (solid line). Ideally, in the hollow-phantom configuration, fewer internal neutrons are expected and the total

H_n/D_p at each location should be less compared to the same locations inside the solid-phantom configuration. However, these results again suggest that the contribution of internal neutrons is much smaller than the contribution of external neutrons to locations off-axis to the treatment volume.

To study the difference in H_n/D_p in the air, a comparison of H_n/D_p for 162 MeV proton beam is shown for in-air and cylindrical-phantom configurations. Figure 7.20, and Figure 7.21 shows the experimentally measured and FLUKA simulated H_n/D_p values in air for the 162 MeV proton beam, respectively. Both experimentally measured and FLUKA simulation results show a higher H_n/D_p in cylindrical-phantom configuration (dotted line) than in the in-air configuration (solid line). This result suggests that the contribution of internal neutrons from the cylindrical phantom could be added to that from external neutrons or that a greater scattering of the external neutrons by the cylindrical phantom leads to an increased in H_n/D_p. For this complicated situation, it is again not possible to quantify H_n/D_p due to internal neutrons based on these four configurations.

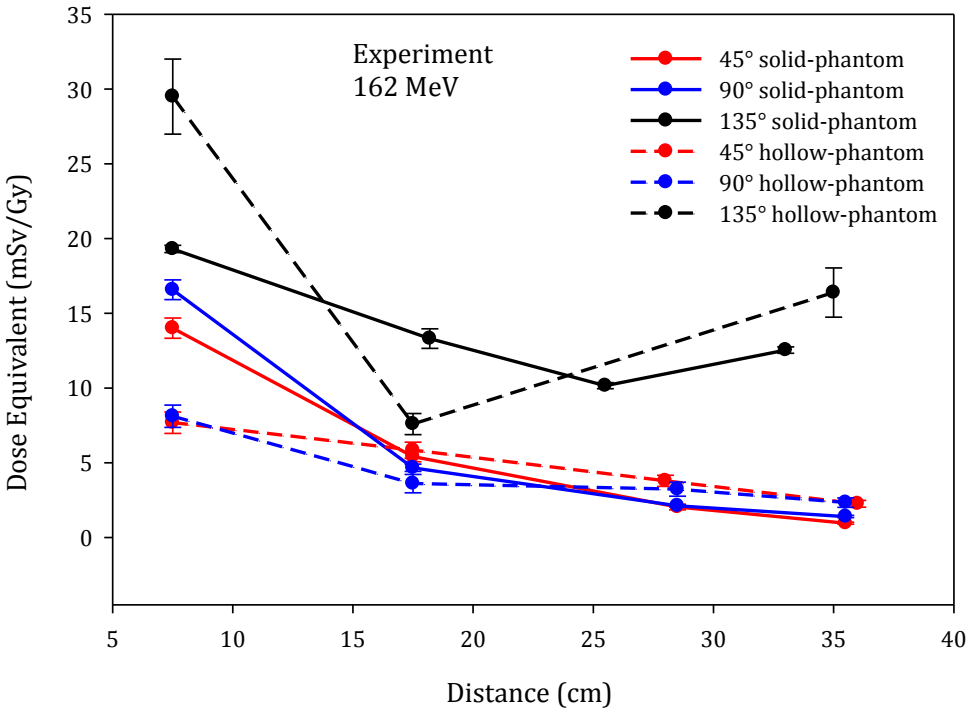

Figure 7.18: Experimentally measured H_n/D_p values as a function of distance from isocenter inside the phantom for solid-phantom and hollow-phantom configurations for a 162 MeV proton beam at 45°, 90°, and 135° to primary beam.

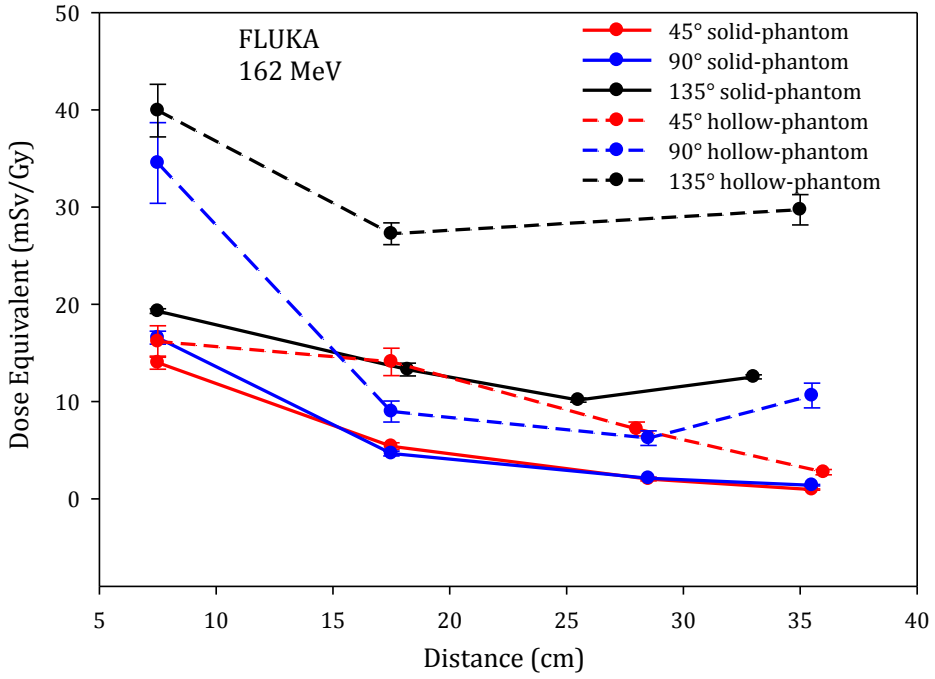

Figure 7.19: FLUKA simulated H_n/D_p values as a function of distance from isocenter inside the phantom for solid-phantom and hollow-phantom configurations for a 162 MeV proton beam at 45°, 90°, and 135° to primary beam.

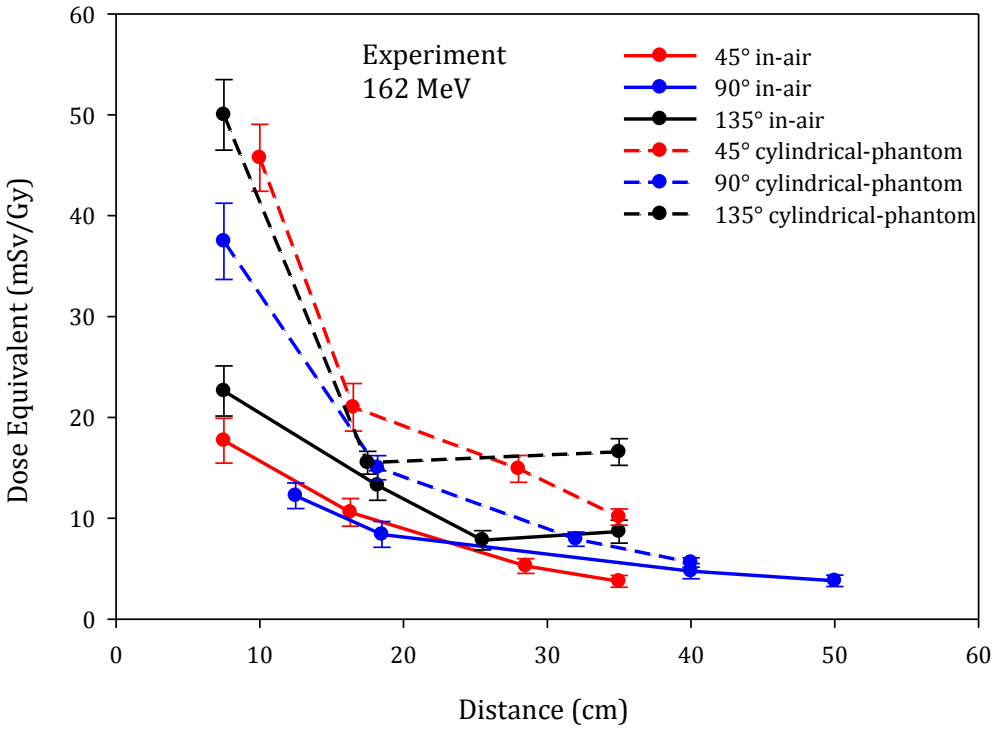

Figure 7.20: Experimentally measured H_n/D_p values in air as a function of distance from isocenter for in-air and cylindrical-phantom configuration for a 162 MeV proton beam at 45°, 90°, and 135° to primary beam.

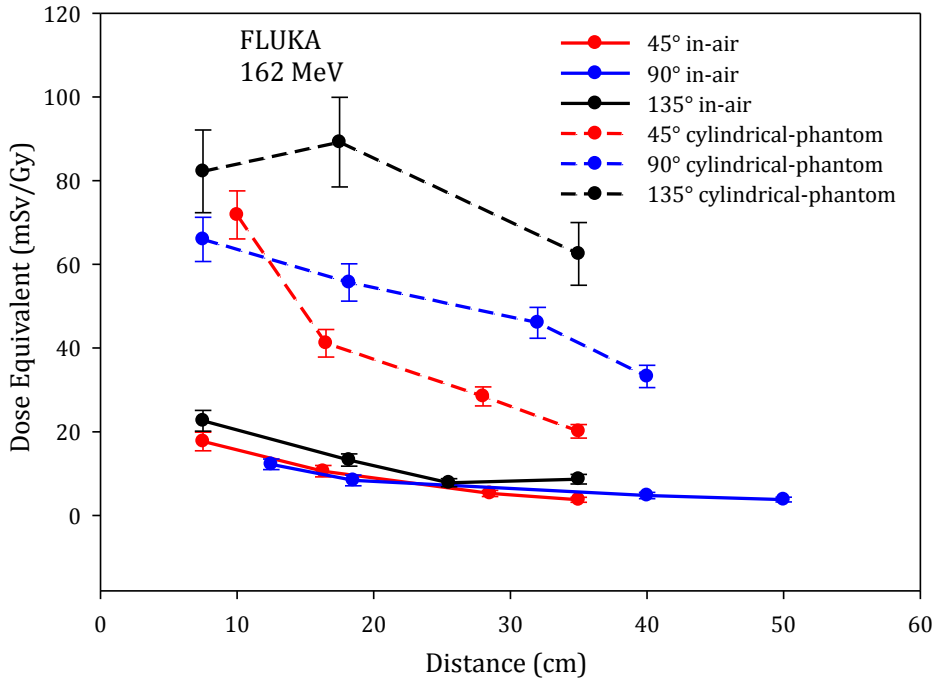

Figure 7.21: FLUKA simulated H_n/D_p values in air as a function of distance from isocenter for in-air and cylindrical-phantom configurations for a 162 MeV proton beam at 45°, 90°, and 135° to primary beam.

7.1.3 *H_n/D_p dependence on energy*

To study the dependence of H_n/D_p on energy, the detector at 17.5 cm from isocenter and at 90° to the primary beam is chosen for all four configurations. The diagram of the setup is shown in Figure 7.22 for the solid-phantom and in-air configurations and a similar setup was used for hollow-phantom and cylindrical-phantom configurations.

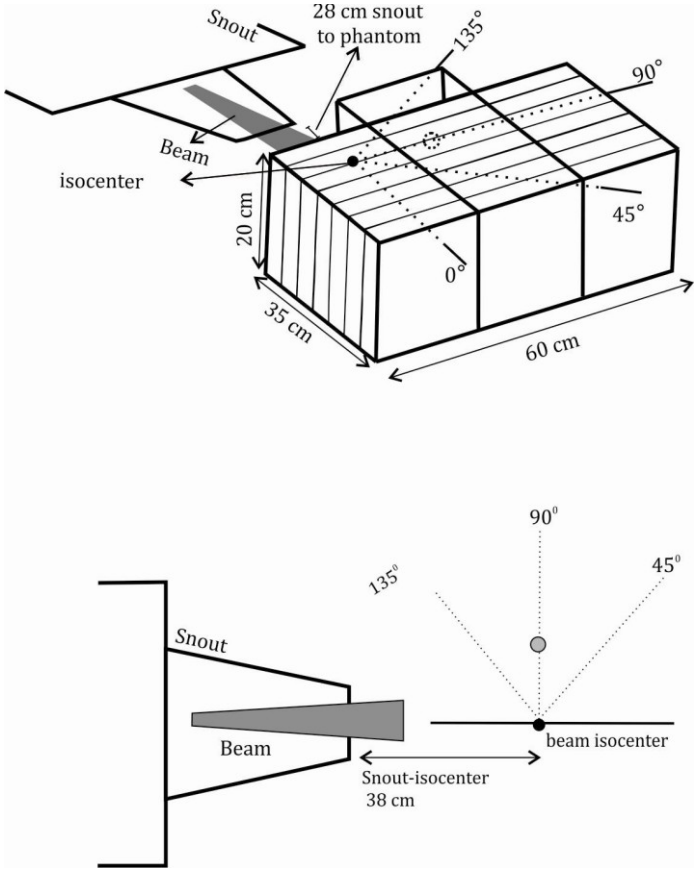

Figure 7.22: Diagram of the locations where dose equivalent was calculated at 17.5 cm from isocenter in solid-phantom (top) and in-air (bottom) configuration.

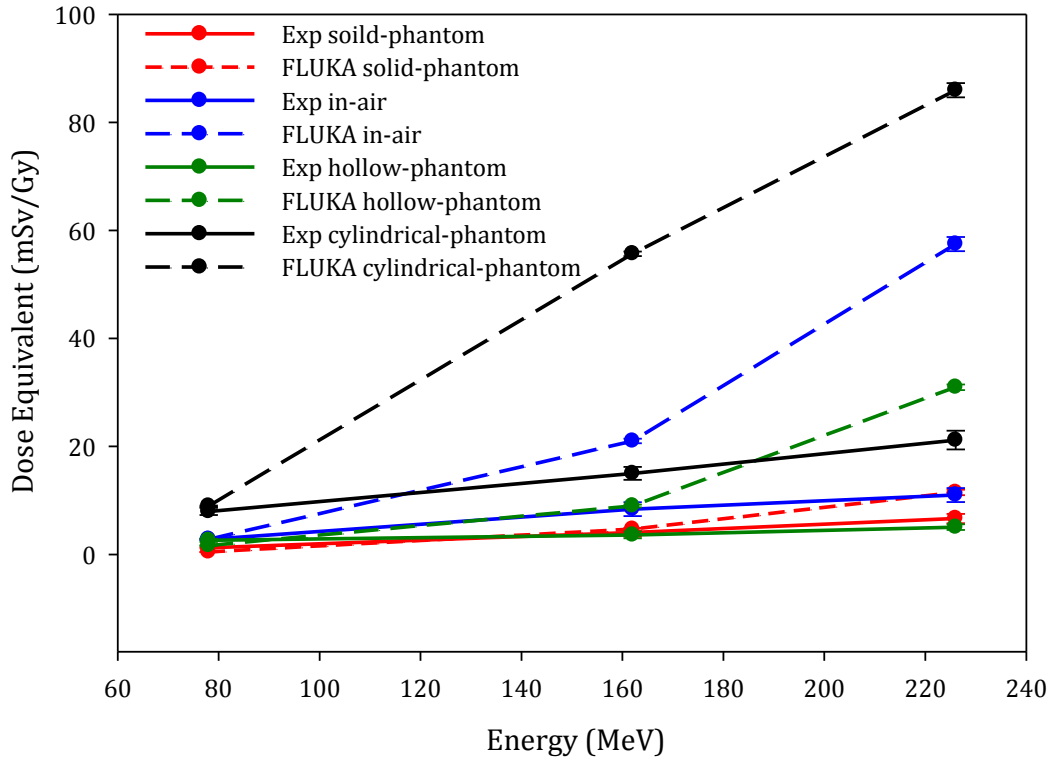

Figure 7.23: Experimentally measured (solid) and FLUKA simulated (dashed) H_n/D_p at 17.5 cm and 90° to primary beam for 78 MeV, 162 MeV and 226 MeV protons for solid-phantom, in-air, hollow-phantom, cylindrical-phantom configurations.

Figure 7.23 shows both the experimentally measured and FLUKA simulation H_n/D_p values at 17.5 cm and 90° to the primary beam for 78 MeV, 162 MeV and 226 MeV proton beams. As the energy of the primary beam increases, the dose equivalent due to secondary neutrons increases. The highest H_n/D_p was observed for 226 MeV proton beam and H_n/D_p progressively decreased for 162 MeV and 78 MeV proton beams. For example, the experimentally measured H_n/D_p value for the solid-phantom configuration decreased from 6.64 ± 0.92 mSv/Gy for 226 MeV protons to 1.24 ± 0.11 mSv/Gy for 78 MeV protons, while for in-air configuration,

H_n/D_p decreased from 11.51 ± 1.31 mSv/Gy for 226 MeV protons to 2.71 ± 0.16 mSv/Gy for 78 MeV protons. The FLUKA simulation H_n/D_p for the solid-phantom configuration decreases from 11.51 ± 0.52 mSv/Gy for 226 MeV protons to 0.52 ± 0.02 mSv/Gy for 78 MeV protons, while for the in-air configuration, the H_n/D_p decreased from 57.41 ± 1.32 mSv/Gy for 226 MeV protons to 2.11 ± 0.17 mSv/Gy for 78 MeV protons. For both experiment and simulation, a greater H_n/D_p is found for higher energy and lower H_n/D_p is found for lower energy inside the phantom (solid-phantom and cylindrical-phantom) and in air (hollow-phantom and cylindrical-phantom). This is expected because higher energy protons create more neutrons when they undergo nuclear interactions in the beam delivery device and in the phantom material, causing greater H_n/D_p at higher energy. The effective beam scan area is also an important parameter in neutron production, since a larger beam scan area results in greater neutron production. In this study, a common beam scan area of 18 × 18 cm^2 was used and since the scan area was substantially greater than the size of the patient aperture (5 cm diameter) used in this study, a greater portion of the field size was stopped by the patient aperture. This caused the 226 MeV undergo more nuclear interactions within the aperture, leading to greater neutron production compared to 162 MeV and 78 MeV proton beam.

7.1.4 H_n/D_p dependence on angle

To study H_n/D_p as a function of angle, the detectors at 17.5 cm distance from the beam isocenter was chosen for all four configurations. The diagram of the setup is

similar to that value shown in Figure 7.22. Both experimentally measured (solid) and FLUKA simulation (dashed) H_n/D_p values for a 162 MeV proton beam are shown in Figure 7.24. As can be seen from this figure, as the angle increases from 45° to 135°, H_n/D_p, in general, also increases. For example, as the angle increase from 45° to 135°, H_n/D_p for the solid-phantom configuration increases by up to a factor of 1.8 in the experiment and by 2.4 in the simulation. For the in-air configuration, the increase factor is 1.3 in the experiment and 2.5 in the simulation. The higher H_n/D_p at 135° suggests that a patient will receive greater H_n/D_p at the locations closer to the snout. Although, the general trend of higher H_n/D_p is visible as the angle increases, at 90° a decrease in H_n/D_p (in-air and hollow-phantom) was observed in the experimentally measured result as the angle increased. It could be that in the 45° detectors, the forward moving neutrons (>~10 MeV) make a significant contribution in addition to isotropic neutrons (<10 MeV), but that at 90° the contribution from forward moving neutrons becomes less, leading to the decrease seen in H_n/D_p. At 135°, the fluence from isotropic neutrons becomes higher as they are closer to the snout and this leads to an increase in H_n/D_p.

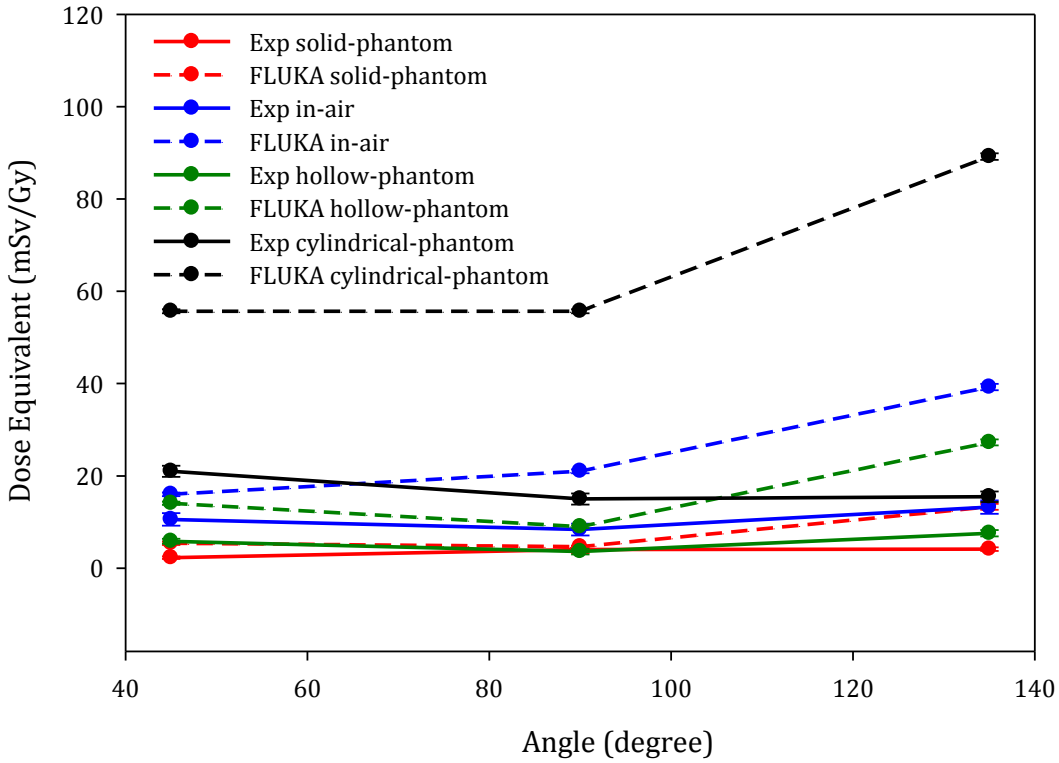

Figure 7.24: : Experimentally measured (solid) and FLUKA simulated (dashed) H_n/D_p as a function of angle at 17.5 cm for a 162 MeV proton beam for solid-phantom, in-air, hollow-phantom, cylindrical-phantom configurations.

7.1.5 Experiment versus simulation

In order to compare results from the FLUKA simulation and experimentally measured H_n/D_p values, the ratio of FLUKA simulation to experimentally measured data is shown in Figure 7.25. In this figure, it can be seen that FLUKA simulation results for each proton beam agrees reasonably well with the experimentally measured data. The agreement is in general within a factor of 2 to 4 for most locations inside the phantom (solid-phantom and hollow-phantom) and in air (in-air

and cylindrical-phantom) but at a few locations, the disagreement is up to a factor of 9.

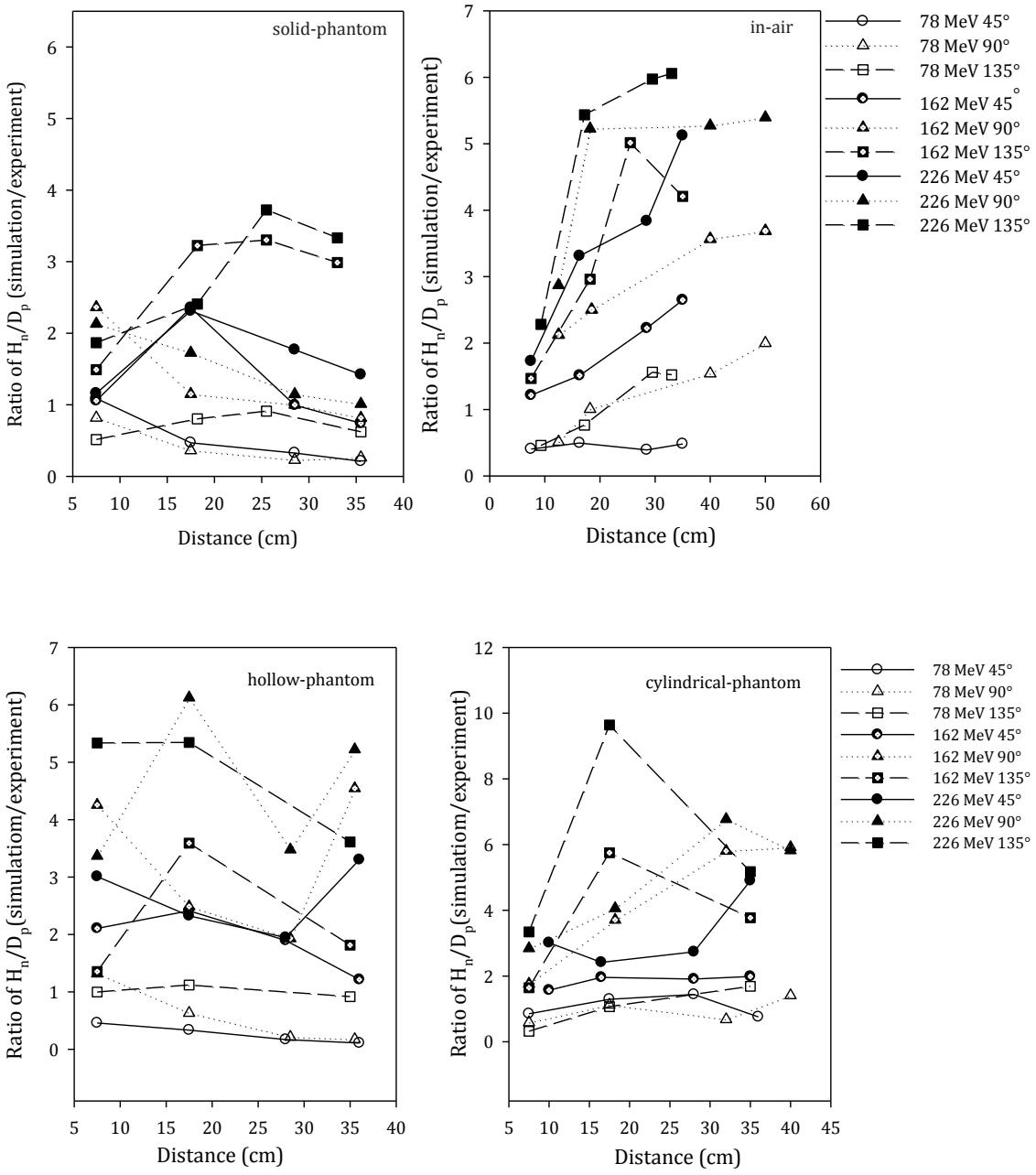

Figure 7.25: Ratio of FLUKA simulation to experimentally measured values of H_n/D_p for 78 MeV, 162 MeV, and 226 MeV protons for solid-phantom (top left), in-air (top right), hollow-phantom (bottom left), and cylindrical-phantom (bottom right) configuration.

The agreement is better inside the phantom than in air. Inside the phantom, the largest disagreement between experiment and simulation is about a factor of 6, and in air this is about a factor of 9. The disagreement is higher for the 162 MeV and 226 MeV proton beams compared to the 78 MeV proton beam. The source of error in this disagreement could be the followings: a) the lack of detail in the simulation of the geometry of the uniform scanning system, and b) a difference in neutron cross sections in experiment and FLUKA simulation. For the energy range (78 MeV to 226 MeV) used in this study, the CR-39 PNTD detector sensitivity is nearly constant and this suggest that FLUKA calculated H_n/D_p could be systematically high for all the configurations.

CHAPTER 8

Discussion and Conclusions

The primary aim of this study was to quantify the dose equivalent due to secondary neutrons for three different primary proton energies, 78 MeV, 162 MeV, and 226 MeV in proton radiotherapy. We investigated the detailed spatial distribution of secondary neutron dose equivalent to primary proton dose, H_n/D_p, inside a phantom and in air for a fixed aperture size, fixed SOBP, and a fixed snout to surface distance using a uniform scanning system at the ProCure Proton Therapy Center, Oklahoma City, OK. Four different configurations, named as solid-phantom, in-air, hollow-phantom, and cylindrical-phantom, have been designed for the purposes of this study. The study was carried out by means of both experiment and simulation, where CR-39 plastic nuclear track detector was used as detector for the experiment and the simulations were performed using the Monte Carlo radiation transport code FLUKA. In solid-phantom configuration, a solid phantom was used to simulate the dose equivalent that a patient would receive in different organs during actual treatment. The in-air configuration was designed to observe the neutrons dose equivalent in the absence of a phantom. The hollow-phantom configuration was created by placing a hole along the beam direction in the solid phantom to observe

the dose equivalent if the primary beam does not interact with phantom material. The cylindrical phantom-phantom configuration was designed to observe the dose equivalent if the primary beam interacts only along the beam path in the phantom material.

Table 8.1: The maximum and minimum H_n/D_p from experiment and simulation of this study inside the phantom due to solid-phantom and hollow-phantom configuration and in air due to in-air and cylindrical-phantom configuration.

Proton beam (MeV)	H_n/D_p (mSv/Gy) inside the phantom (solid-phantom and hollow-phantom)		H_n/D_p (mSv/Gy) in air (in-air and cylindrical-phantom)	
	Maximum	Minimum	Maximum	Minimum
	Experiment			
78	7.47 ± 1.42	0.31 ± 0.08	35.61 ± 1.48	1.35 ± 0.08
162	29.49 ± 2.51	1.29 ± 0.17	50.01 ± 3.51	3.74 ± 0.61
226	37.11 ± 2.41	1.81 ± 0.42	45.79 ± 3.61	4.82 ± 0.61
	FLUKA simulation			
78	7.29 ± 0.71	0.13 ± 0.01	1.21 ± 0.06	11.41 ± 0.41
162	1.01±0.06	39.92 ± 2.71	82.22 ± 9.11	9.91 ± 0.34
226	2.51 ± 0.14	135.66 ± 6.78	153.15±8.51	24.81 ± 0.82

For all these configurations, the ratio of dose equivalent from secondary neutrons calculated outside the treatment volume to primary proton dose, $H_n/D_{p,}$ was

observed to decrease as a function of distance from beam isocenter. Table 8.1 lists the experimentally and FLUKA simulated data for maximum and minimum H_n/D_p inside the phantom (solid-phantom and hollow-phantom) and in air (in-air and cylindrical-phantom) for all four experimental configurations. In this study, the experimentally measured H_n/D_p for both inside the phantom and in air ranged from 0.31 ± 0.08 mSv/Gy to 35.61 ± 1.48 mSv/Gy for 78 MeV, 1.29 ± 0.17 mSv/Gy to 50.01 ± 3.51 mSv/Gy for 162 MeV, 1.81 ± 0.42 mSv/Gy to 37.11 ± 2.41 mSv/Gy for 226 MeV. The FLUKA simulated H_n/D_p ranged from 0.13 ± 0.01 mSv/Gy to 11.41 ± 0.41 mSv/Gy for 78 MeV, 1.01 ± 0.06 mSv/Gy to 82.22 ± 9.11 mSv/Gy for 162 MeV, 2.51 ± 0.14 mSv/Gy to 153.15 ± 8.51 mSv/Gy for 226 MeV proton beam. In addition, both inside the phantom and in air, H_n/D_p due to secondary neutrons increased as the energy of the primary proton beam increased and a higher H_n/D_p was also observed as the angle increased. In general a good agreement between experimentally measured and FLUKA simulated data was observed. Inside the phantom, the experimentally measured and FLUKA simulated H_n/D_p agreed within a factor of 4 and in air the agreement varied up to a factor of 9.

This data suggests that the neutron dose equivalent for a uniform scanning system in a common proton treatment facility may range from 0.3 mSv/Gy to 50 mSv/Gy. The higher H_n/D_p in air than that of inside the phantom suggests that the production of neutrons in the beam shaping components is much higher than inside the phantom.

For the verification of this study and to compare the H_n/D_p from uniform scanning with other mode of beam delivery system, a comparison of our experimentally measured data with published literature is made and shown in

Table **8.2**. These comparisons are not exact as patient specific parameters, snout design, and beam delivery system varies from one facility to the other.

Table 8.2: Comparison of this work with previously published results at different treatment facilities: ProCure Proton Therapy Center at Oklahoma, USA (ProCure), Midwest Proton Radiotherapy Institute (MPRI), the Paul Scherrer Institute Proton Therapy Facility Switzerland (PSI), the Harvard Cyclotron Laboratory, USA (HCL), the Loma Linda University Medical Center, USA (LLUMC).

Facility	Proton beam (MeV)	Beam delivery	Off-axis Distance (cm)	SOBP (cm)	H_n/D_p (mSv/Gy)
This work	78	uniform	35	4	0.49
ProCure , OKC (Zheng et al., 2012)	78	uniform	35	4	0.35
MPRI (Hecksel et al., 2010)	151	uniform	40	10	0.8
PSI (Schneider et al., 2002)	177	pencil	50	10	0.12
This work	162	uniform	50	4	3.79
HCL (Yan et al., 2002)	151	passive	50	8.2	4.8
HCL (Polf and Newhauser, 2005)	160	passive	50	3	3.9
This work	226	uniform	7.5	4	16.61
LLUMC (Moyers et al., 2008)	250	passive	11.5	10	13.6

As shown in the table, Zheng et. al. (Zheng et al., 2012) conducted a study for the same uniform system used in this study at the ProCure Proton Therapy Center, Oklahoma, USA. For a 78 MeV proton beam Zheng et. al. reported 0.35 mSv/Gy at 50 cm off-axis to the primary beam with a $30 \times 30 \times 30\ cm^3$ phantom centered at isocenter for a 4 cm SOBP. In our study, H_n/D_p for the same beam conditions, but at 35.5 cm off-axis to primary beam, was found to be 0.49 mSv/Gy. H_n/D_p measured by Zheng et al. differed by 28% from our measured data. This could be due to the fact that detector distance in the current study was closer to the isocenter than that used in Zheng et al study. In addition, Zheng et. al. measured neutron dose equivalent using a SWENDI-II neutron detector, where the measurements technique of dose equivalent is different than that for CR-39 PNTD and this can enhance the difference in the measured H_n/D_p.

In another study, Hecksel et. al. (Hecksel et al., 2010) reported 0.8 mSv/Gy for a uniform scanning system at 40 cm off-axis to the primary beam with 10 cm SOBP for a 151 MeV proton beam. This study was conducted at the Midwest Proton Radiotherapy Institute, USA (MPRI) using a SWENDII-II neutron detector. This result disagrees with our study by a factor of 4.7 for a 162 MeV proton beam. This disagreement could be due to the difference in dose equivalent measurement technique, difference in SOBP, and difference in energy between our study and that of Hecksel et. al.

For a 177 MeV proton beam, Schneider et. al. (Schneider et al., 2002) conducted a study using pencil beam scanning system at Paul Scherrer Institute (PSI) Proton Therapy Facility, Switzerland. The study was performed with the help of Bonner spheres, CR-39 PNTD and FLUKA Monte Carlo radiation transport code. At 50 cm off-axis to the primary beam, with 10 cm SOBP, the reported H_n/D_p using a Bonner sphere of 25 cm diameter was 0.12 mSV/Gy. At the similar location, the H_n/D_p from our study for a 162 MeV proton beam, disagreed by a factor of 32.5. It is important to note that pencil beam scanning systems do not use any beam shaping components (e.g. patient collimator) to conform the beam to the treatment volume. On the other hand, uniform scanning systems uses beam shaping components to conform the beam to the tumor and this might have caused a greater H_n/D_p in our study.

In a separate study at the Harvard Cyclotron Laboratory (HCL), Yan et al. (Yan et al., 2002) reported 4.5 mSv/Gy at 50 cm off-axis to the primary beam, for a 160 MeV proton beam, 8.2 cm modulation width, and with a phantom at isocenter of 26 cm diameter and 24 cm length. This measurement was done for a passive scattering beam delivery system using a set of Bonner spheres of varying diameters (5.1 cm to 45.7 cm). At a similar location, our measured value was 3.8 mSv/Gy for a 162 MeV proton beam. In another study, Polf and Newhauser (Polf and Newhauser, 2005) numerically simulated similar experimental conditions to those used by Yan et al. (Yan et al., 2002) using the MCNPX Monte Carlo radiation transport code. Polf et. al. reported a 3.9 mSv/Gy for a 160 MeV proton beam, 3 cm modulation width at 90^0 to

the beam axis and 50 cm from the isocenter. Overall, the studies conducted by Yan et. al. and Polf et. al. agree with our study within 15%, suggesting that the production of secondary neutrons in a passive scattering system is similar to that created in a uniform scanning system.

For relatively higher energy (at 250 MeV), Moyers et. al. (Moyers et al., 2008) reported H_n/D_p at multiple off-axis locations for a passive scattering system installed at the Loma Linda University Medical Center, USA (LLUMC). Five different approaches were employed in this study for the measurement of H_n/D_p for a 250 MeV proton beam around the beam delivery system. One of the approach used CR-39 PNTD, where the method to determine the dose equivalent from CR-39 PNTD was identical to the method used in this study. At 11.5 cm off-axis to the primary beam and 15 cm inside the phantom, the reported H_n/D_p was 13.6 mSv/Gy. For a similar location, at 7 cm off-axis and 10 cm inside the phantom, the measured H_n/D_p from this study is 16.6 mSv/Gy. The agreement between this study and the study carried by Moyers et. al. is within 18%. This result again suggests the neutron dose equivalent from a uniform scanning system is similar to that of a passive scattering system.

The overall comparison indicates that the H_n/D_p due to secondary neutrons from a uniform scanning system is of a similar order of magnitude to that of passive scattering systems, but lower than that produced by pencil beam scanning systems. This study suggests that the available snout used in the uniform scanning system

may need to be improved if a reduction in H_n/D_p due to secondary neutrons is to be achieved.

The statistical uncertainty in the FLUKA simulation was calculated to be around 10%, though the fluence to dose equivalent conversion in the simulation could add as much as 30% uncertainty to the values of H_n/D_p (Schneider et al., 2002). On the other hand, the dose equivalent measurements in CR-39 PNTD are model independent, although the measurement process and detector calibration could still lead to up to 25% uncertainty in the measured results. Despite these uncertainties, the quantitative data on H_n/D_p at various distances from isocenter demonstrates the possible neutron exposure that a patient would receive from a common proton treatment facility that employs a uniform beam delivery system. In addition, this data can be used to find the organ equivalent dose, which can help in estimating the risks of secondary cancer for patients undergoing proton radiotherapy. Also, our study can improve the available radiation risk models which could ultimately help the clinicians to make informed decisions in future.

This study did not incorporate the contribution of H_n/D_p from thermal and epithermal neutrons (<1 MeV), because CR-39 PNTD is insensitive to neutrons in that energy region. To incorporate the contribution of neutrons <1 MeV, a new experiment could be performed. For this purpose, a pair of ^{6}LiF foils can be sandwiched between the CR-39 PNTDs, where one of the detectors is covered by a thermal neutron absorber (Gd) and the other is left uncovered. The design of the

experiment could be adapted from the work carried out by Benton et. al. (Benton et al., 2001), where the measurement was done to detect thermal and resonance neutrons during spaceflight. ^{6}LiF has a high cross section for low energy neutrons and the absorption of low energy neutron leads to the ^{6}Li(n,T)α reaction. The α and ^{3}T produced in the uncovered ^{6}LiF will then create tracks to the CR-39 PNTD and these tracks are due to thermal neutrons. The covered foils, on the other hand, will see no thermal neutrons as they will be absorbed by gadolinium (Gd) absorber. The measurement of tracks due to covered and uncovered pair of ^{6}LiF will be due to neutrons of < 1 MeV (as in this study).

This study could not separate the contribution from external and internal neutrons using the current setup. For example, at 35.5 cm from beam isocenter, the experimentally measured H_n/D_p for a 162 MeV is 1.7 mSv/Gy and 2.3 mSv/Gy for solid-phantom and hollow-phantom configuration, respectively. This states that a higher H_n/D_p was observed in the configuration where secondary neutrons due to primary protons were supposed to be minimal. However, this suggests that the production of neutrons in the phantom by the primary proton beam is overwhelmed by the neutrons created in the beam delivery device. In the future, a Monte Carlo simulation can be done to separate the contribution of internal and external neutrons.

In addition, this study did not include any range compensator which may lead to some differences in the actual neutron dose equivalent to tissue surrounding the

treatment volume in an actual patient treatment. The whole study was conducted only for one particular setup of treatment parameters which might be different from an actual treatment scenario. In the future, experiments can be performed for varying patient specific parameters, e.g. various beam scanning areas, different snout size, and different SOBP can be performed for the better estimation of H_n/D_p. This can help in understanding the detailed distribution of neutron dose in proton radiotherapy. Finally, a detailed simulation of the beam delivery system can be done to improve the agreement between experiment and simulation.

References

Aiginger H, Andersen V, Ballarini F, Battistoni G, Campanella M, Carboni M, Cerutti F, Empl A, Enghardt W, Fassò A, Ferrari A, Gadioli E, Garzelli M V, Lee K, Ottolenghi A, Parodi K, Pelliccioni M, Pinsky L, Ranft J, Roesler S, Sala P R, Scannicchio D, Smirnov G, Sommerer F, Wilson T and Zapp N 2005. The FLUKA code: New developments and application to 1 GeV/n iron beams. *Advances in Space Research,* **35,** 214-222.

Akagi T, Higashi A, Tsugami H, Sakamoto H, Masuda Y and Hishikawa Y 2003. Ridge filter design for proton therapy at Hyogo Ion Beam Medical Center *Phys. Med. Biol.,* **48,** N301-N312.

Albertini F. 2011. *Planning and Optimizing Treatment Plans for Actively Scanned Proton Therapy: evaluating and estimating the effect of uncertainties.* PhD, Università degli Studi di Milano.

Andersen V, Ballarini F, Battistoni G, Campanella M, Carboni M, Cerutti F, Empl A, Fassò A, Ferrari A, Gadioli E, Garzelli M V, Lee K a O, Pelliccioni M, Pinsky L S, Ranft J, Roesler S, Sala P R and Wilson T L 2004. The FLUKA code for space applications: recent developments. *Advances in Space Research,* **34,** 1302-1310.

Ballarini F, Battistoni G, Brugger M, Campanella M, Carboni M, Cerutti F, Empl A, Fassò A, Ferrari A and Gadioli E 2007. The physics of the FLUKA code: Recent developments. *Advances in Space Research,* **40,** 1339-1349.

Battistoni G, Muraro S, Sala P R, Cerutti F, Ferrari A, Roesler S, Fassò A and Ranft J 2007. The FLUKA code: Description and benchmarking. *In:* ALBROW, M. & RAJA, R. (eds.) *Proceedings of the Hadronic Shower Simulation Workshop 2006.* Fermilab: AIP Conference Proceedings.

Benton E R. 2004. *Radiation Dosimetry At Aviation Altitude And In Low Earth Orbit.*

Benton E R, Benton E V and Frank A L 2001. Neutron dosimetry in low-earthorbit using passive detectors. *Radiation Measurements,* **33**.

Benton E V, Ogura K, Frank A L, Atallah T M and Rowe V 1986. Response of differernt types of CR-39 to energetic ions. *Int.J.Radiat.Appl.lnstrum., Part D,* **12,** 79-82.

Bethe H 1930. Zur Theorie des Durchgangs schneller Korpuskularstrahlen durch Materie. *Annalen der Physik,* **5**.

Binns P J and Hough J H 1997. Secondary Dose exposures during 200MeV proton therapy *Radiat. Prot. Dos.,* **70,** 441-444.

Cartwright B G, Shirk E K and Price P B 1978. A Nuclear-Track-Recording Polymer of Unique Sensitivity and Resolution. *Nuclear Instruments and Methods,* **153,** 457-460.

Cassou R M and Benton E V 1978. Properties and Applications of CR-39 Polymeric Nuclear Track Detector. *Nuclear Track Detection,* **2,** 173-179.

Chu W T, Ludewigt B A and Renner T R 1993. Instrumentation for treatment of cancer using proton and light-ion beams. *Review of Scientific Instruments* **64,** 2055-2122.
Decimal. 2013. *Decimal, The benchmark for custom radiation therapy* [Online]. Available: http://www.dotdecimal.com/products/protons [Accessed].
Delaney G, Jacob S, Featherstone C and Barton M 2005. The role of radiotherapy in cancer treatment: estimating optimal utilization from a review of evidence-based clinical guidelines. *Cancer,* **104,** 1129-37.
Dendale R, Lumbroso-Le R L, Noel G, Feuvret L, Levy C, Delacroix S, Meyer A, Nauraye C, Mazal A, Mammar H, Garcia P, D'hermies F, Frau E, Plancher C, Asselain B, Schlienger P, Mazeron J J and Desjardins L 2006. Proton beam radiotherapy for uveal melanoma: results of Curie Institut-Orsay proton therapy center (ICPO). *Int J Radiat Oncol Biol Phys,* **65**.
Devita V T, Oliverio V T and Muggia F M 1979. The drug development and clinical trials programs of the division of cancer treatment, National Cancer Institute. *Cancer Clin Trials,* **2,** 195-216.
J M Dewitt, PhD Thesis 2011. Department of Physics. Oklahoma State University, Stillwater, OK RADIATION SHIELDING FOR FUTURE SPACE EXPLORATION MISSIONS.
Dowdell S J. 2011. *Pencil Beam Scanning proton Therapy: The significance of secondary particles* PhD, University of Wollongong.
Dreute J, Trakowski W, Schöfer B, Brechtmann C, Drechsel H, Eversberg H, Fricke W, Beer J, Wiegel B and Heinrich W 1986. The Siegen Automatic Measuring System for Nuclear Track Detectors: Status and New Developments. *Nuclear Tracks,* **12,** 261-264.
Farr J B, Mascia A E, Hsi W C, Allgower C E, Jesseph F, Schreuder A N, Wolanski M, Nichiporov D F and Anferov V 2008. Clinical characterization of a proton beam continuous uniform scanning system with dose layer stacking. *Med. Phys.,* **35,** 4945-4954.
Fassò A, Ferrari A, Ranft J and Sala P R 2005. FLUKA: a multi-particle transport code. CERN, INFN, SLAC.
Ferrari A, Pelliccioni M, Pillon M and Fluence to Effective Dose Equivalent Conversion Coefficients for Neutrons up to 10 Tev R P D, 165-173 (1997). 1997. Fluence to Effective Dose Equivalent Conversion Coefficients for Neutrons up to 10 TeV *Radiat. Prot. Dosim.,* **71,** 165-173.
Fluka. 2013. *A quick look at FLUKA's physics, structure and capabilities* [Online]. Available: http://www.fluka.org/fluka.php?id=man_onl&sub=3 [Accessed].
Goitein M 2008. *Radiation Oncology: A Physicist's-Eye View*, Spingerlink.
Gottschalk B 2004. Passive Beam Spreading in Proton Radiation Therapy.
Halg R A, Besserer J and Schneider U 2011. Comparative simulations of neutron dose in soft tissue and phantom materials for proton and carbon ion therapy with actively scanned beams *Med. Phys.,* **38,** 3149-3156.
Hall E and Giaccia A 2006. Radiology for the Radiologist. Sixth ed. Philadelphia: Lippincott Williams & Wilkins.
Hecksel D, Anferov V, Fitzek M and Shahnazi K 2010. Influence of beam efficiency through the patient-specific collimator on secondary neutron dose equivalent in

double scattering and uniform scanning modes of proton therapy. *Medical Physics,* **37,** 2910.
Henke R P and Benton E V 1971. On Geometry of Tracks in Dielectric Nuclear Track Detectors. *Nucl. Instr. Meth.,* **483,** 483-489.
Henke R P, Ogura K and Benton E V 1986. Standard Method for Measurement of Bulk Etch in CR-39. *Nuclear Tracks,* **12,** 307-310.
Henshaw D L, Griffiths N, Landen O a L and Benton E V 1981. A Method of Producing Thin CR-39 Plastic Nuclear Track Detectors and Their Application in Nuclear Science and Technology. **180,** 65-77.
Neutron Interactions: Part I, 2010, Presentation on Radiation Physics, Available: http://www.uthgsbsmedphys.org/gs02-0093/3.3a-howellneutronlecture01.pdf.
ICRP (International Commission on Radiological Protection) 1991 *ICRP Publication No. 60* (Oxford).
ICRP (International Commission on Radiological Protection), Conversion Coeffcients for use in Radiological Protection against External Radiation, ICRP Publication 74, Ann. ICRP 26, Pergamon Press (1996).
Basic Aspects of High Energy Particle Interactions and Radiations Dosimetry, ICRU report 28.
ICRU. "Microdosimetry". Report of the international Commission on Radiation Units and Measurements, **36,** 1983
Fundamental Quantities and Units of Ionizing Radiation.
ICRU (International Commission on Radiological Units), 1998, Proton Dosimetry: Part 1. Beam Production, Beam Delivery and Measurement of Absorbed Dose, Report 59, (Bethasa MD).
ICRU (ntrenational Commision on Radiation Units and Measurements), 2007, Report 78, Vol 7, Journal of the ICRU.
Jiang H, Wang B, Xu X G, Suit H D and Paganetti H 2005. Simulation of organ-specific patient effective dose due to secondary neutrons in proton radiation treatment. *Phys. Med. Biol.,* **50,** 4337-4353.
Joiner M and Kogel A V 2009. *Basic Clinical Radiobiology,* London, Hodder Arnold.
Jones D T L and Schreuder A N 2001. Magnetically scanned proton therapy beams: rationales and principles. *Radiat Phys Chem,* **61,** 615-8.
Kanai T, Kawachi K, Kumamoto Y, Ogawa H, Yamada T, Matsuzawa H and Inada T 1980. Spot Scanning system for proton therapy. *Medical Physics,* **7,** 365-369.
Khan F 2003. *The physics of radiation therapy, 3rd edn.,* Baltimore, Williams & Wilkins.
Koehler A M, Schneider R J and Sisterson J M 1977. Flattening of proton dose distributions for large-field radiotherapy. *Medical Physics,* **4,** 297-301.
Moyers M F, Benton E R, Ghebremedhin A and Coutrakon G 2008. Leakage and scatter radiation from a double scattering based proton beamline. *Medical Physics,* **35,** 128.
NCI (National Cancer Institute), *Radiation Therapy for Cancer, 2013,* Available: http://www.cancer.gov/cancertopics/factsheet/Therapy/radiation.
NIST (National Institute of Standards and Technology), Stopping-power and range tables for protons, 2012, Available: http://physics.nist.gov/PhysRefData/Star/Text/PSTAR.html.

NNDC (National Nuclear Data Center), 2013, *Evaluated nuclear data file (ENDF)*, 2013, Available: http://www.nndc.bnl.gov/exfor/endf00.jsp.

Noll A, Rusch G, Rocher H, Dreute J and Heinrich W 1988. The Siegen Automatic Measuring System for Nuclear Track Detectors: New Developments. *Nuclear Tracks and Radiation Measurements,* **15,** 265-368.

Patel R R and Arthur D W 2006. The emergence of advanced brachytherapy techniques for common malignancies. *Hematology/Oncology Clinics of North America,* **20,** 97-118.

Pelliccion M 1998. Radiation weighting factors and high energy radiation. *Radiation Protection Dosimetry,* **80,** 371-378.

Perez-Andujar A, Newhauser W D and Deluca P M 2009. Neutron Production from beam modifying devices in a modern double scattering proton therapy beam delivery system. *Phys. Med. Biol.,* **54,** 993-1008.

Polf J C, D N W and U T 2005. Patient neutron dose equivalent exposures outside of the proton therapy treatment field. *Radiation Protection Dosimetry,* **115,** 154-158.

Polf J C and Newhauser W D 2005. Calculations of neutron dose equivalent exposures from range-modulated proton therapy beams *Phys. Med. Biol.,* **50,** 3859-3873.

Particle Therapy Co-Operative Groups, May 2013, Avaiable at: http://ptcog.web.psi.ch/ptcentres.html.

P Rinard, Neutron Interactions with Matter: Los Alamos Technical Report, Available: http://www.fas.org/sgp/othergov/doe/lanl/lib-www/la-pubs/00326407.pdf.

Roesler S and Stevenson G R 2006. deq99.f, A FLUKA user-routine converting fluence into effective dose and ambient dose equivalent, 2006, Safety Commission, Technical Note CERN SC-2006-070-RP-TN

Rusch G, Winkel E, Noll A and Heinrich W 1991. The Siegen Automatic Measuring System for Track Detectors: New Developments. *Nuclear Tracks and Radiation Measurements,* **19,** 261-266.

Saha G B 2006. *Physics and Radiobiology of Nuclear Medicine* New York, Springer.

Schlegel W C, Bortfeld T and Grosu A L 2006. *New Technologies in Radiation Oncology,* Berlin, Heidelberg, New York, Springer Berlin.

Schneider U, Agosteo S, Pedroni E and Besserer J 2002. Secondary neutron dose during proton therapy using spot scaninng. *Int J Radiation Oncology Biol. Phys.,* **53,** 244-251.

Seltzer S M 1993. An assessment of the role of charged secondaries from nonelastic nuclear interactions by therapy proton beams in water. NISTIR 5221.

Slater J 1991. The proton treatment center at Loma Linda University of Medical center. *Int J Radiat Oncol Biol Phys,* **22,** 383-389.

Souhami R L and Tobias J S 1986. *Cancer and its management,* Oxford, Blackwell Scientific.

Steneker M, Lomax A and Schneider U 2006. ntensity modulated photon and proton therapy for the treatment of head and neck tumors. *Radiother Oncol. 2006 Aug;80(2):263-7. Epub 2006 Aug 17.,* **80**.

Sternheimer R M and Peierls R F 1971. General Expression for the Density Effect for the Ionization Loss of Charged Particles. *Physical Review B,* **3,** 3681-3692.

Terezakis S A, Heron D E, Lavigne R F, Diehn M and Billy W. Loo J 2011. What the Radiologist Needs to Know about Radiation Oncology. *Radiology,* **261,** 31-44.

Tobias C A, Lawrence J H, Born J L, Mccombs R K, Roberts J E, Anger H O, Low-Beer B V A and Huggins C B 1958. Pituitary Irradiation with High-Energy Proton Beams A Preliminary Report. *Cancer Research,* **18,** 121-134.

Tobias J S 1996. The role of radiotherapy in the management of cancer - an overview. *Ann Acad Med Singapore* **25,** 371-379.

Trakowski W, Schöfer B, Dreute J, Sonntag S, Brechtmann C, Beer J, Drechsel H and Heinrich W 1984. An Automatic Measuring System for Particle Tracks in Plastic Detectors. *Nuclear Instruments and Methods in Physics Research,* **225,** 92-100.

Wiegel B, Beer J, Fricke W, Eversberg H and Heinrich W 1986. Cosmic Ray LET-Spectra Investigated by Automatic Scanning and Measuring of Plastic Nuclear Track Detectors. *Nuclear Tracks,* **12,** 515-518.

Depth Dose Curves, Avaialbe: http://commons.wikimedia.org/wiki/File:Depth_Dose_Curves.jpg.

Wilson R R 1946. Radiological Use of Fast Protons. *Radiology,* **47,** 487-491.

Yan X, Titt U and Koehler A 2002. Measurement of neutron dose equivalent to proton therapy patients outside of the proton radiation field *Nucl Instr Methods Phys Res,* **A476,** 429-434.

Zheng Y, Fontenot J, Taddei P, Mirkovic D and Newhauser W 2008. Monte Carlo simulations of neutron spectral fluence, radiation weighting factor and ambient dose equivalent for a passively scattered proton therapy unit. *Physics in Medicine and Biology,* **53,** 187-201.

Zheng Y, Newhauser W, Fontenot J, Taddei P and Mohan R 2007a. Monte Carlo study of neutron dose equivalent during passive scattering proton therapy. *Physics in Medicine and Biology,* **52,** 4481-4496.

Zheng Y, Newhauser W and Mohan R 2007b. Monte Carlo study of neutron dose equivalent during passive scattering proton therapy. *Physics in Medicine and Biology,* **52,** 4481-4496.

Zheng Y, Ramierz E, Mascia A, Ding X, Okoth B, Zeidan O, Hsi W, Harris B, Schreuder A N and Keole S 2011. Commissioning of output factors for uniform scanning proton beams. *Medical Physics,* **38,** 2299-2306.

Zheng Y, Yaxi L, Zeidan O, Schreuder A N and Keole S 2012. Measurements of neutron dose equivalent for a proton therapy center using uniform scanning proton beams. *Med. Phys.,* **39,** 3484-3492.

VITA

Mohammad Rafiqul Islam

Candidate for the Degree of

Doctor of Philosophy

Thesis: STUDY OF SECONDARY NEUTRONS FROM UNIFORM SCANNING PROTON BEAMS BY MEANS OF EXPERIMENT AND SIMULATION

Major Field: Physics

Biographical:

Education:

Completed the requirements for the Doctor of Philosophy in Physics at Oklahoma State University, Stillwater, OK, in July, 2013

Completed the requirements for the Master of Science in Physics at Oklahoma State University, Stillwater, OK, in March 2013.

Completed the requirements for the Bachelor of Science in Physics at University of Dhaka, Bangladesh, in June 2003.